ABSTRACT

Modeling Dust Coagulation and Chondrule Dust Rim Growth in a Protoplanetary Disk

Chuchu Xiang, Ph.D.

Chairperson: Lorin S. Matthews, Ph.D.

Coagulation of dust particles plays an important role in the formation of planets and is of key importance to the evolution of protoplanetary disks (PPD). Characteristics of dust, such as the diversity of particle size, porosity, charge, and the manner in which dust couples to turbulent gas, affect the collision process. In this work, a numerical model incorporating all of these effects is developed to simulate collisions between dust particles, which leads to dust growth, and between dust and chondrules, which results in fine-grained dust rims (FGRs) on chondrule surfaces. A Monte Carlo algorithm is used to randomly select colliding particles as well as determine the elapsed time interval between collisions. The actual collision outcome is determined by a detailed collision model which takes into account the morphology of the aggregates/FGRs, the trajectory/orientation of the colliding particles, and the electrostatic forces acting between charged grains by calculating the charge distribution on grain surface, etc. Dust growth and FGR formation are compared in environments with different turbulence strengths and different plasma conditions. The physical characteristics and timescales for growth of dust aggregates/FGRs over a range of nebular conditions are quantified, and the interplay between the effects of charge and turbulence on their evolution is investigated.

Modeling Dust Coagulation and Chondrule Dust Rim Growth in a Protoplanetary Disk

by

Chuchu Xiang, B.S., M.S.

A Dissertation

Approved by the Department of Physics

_____

Dwight P. Russell, Ph.D., Interim Chairperson

Submitted to the Graduate Faculty of
Baylor University in Partial Fulfillment of the
Requirements for the Degree
of
Doctor of Philosophy

Approved by the Dissertation Committee

_____

Lorin S. Matthews, Ph.D., Chairperson

_____

Amanda S. Hering, Ph.D.

_____

Gerald B. Cleaver, Ph.D.

_____

Truell W. Hyde, Ph.D.

Accepted by the Graduate School
December 2019

_____

J. Larry Lyon, Ph.D., Dean

Page bearing signatures is kept on file in the Graduate School.

TABLE OF CONTENTS

LIST OF FIGURES

ACKNOWLEDGMENTS

First of all, I would like to thank my advisor, Dr. Lorin Matthews, for guiding me through this challenging journey and providing me with tremendous help in various aspects, from macroscopic research directions to detailed coding problems and paper writing. I benefit greatly from her insight in the research, and am grateful for her prompt replies to my questions and elaborate revisions of the paper drafts. I also wholeheartedly appreciate her for being very generous and considerate when I went through personal problems.

I am grateful to Dr. Truell Hyde for providing instructive advice on the research problems and always giving me kind encouragements, which were reassuring and inspiring when I was self-doubting. I would like to thank Dr. Gerald Cleaver for teaching me courses and being a very nice and helpful graduate program advisor. I would also like to thank Dr. Amanda Hering for patiently answering my questions about analyzing the data and introducing useful statistical methods to me. I appreciate all of them for taking time out of their busy schedules to serve on my dissertation committee. I also acknowledge Dr. Augusto Carballido for explaining physical concepts to me and putting much effort into the preparation of the papers.

I owe a debt of gratitude to Dr. Nina Gunkelmann for providing the LIGGGHTS code and helping integrate it into our code. I am thankful for her patience and kind understanding when I had to delay our co-authored paper in order to finish other projects first.

Thanks to Mr. Mike Hutcheson and Mr. Carl Bell for providing timely help for issues related to the computational cluster. I also appreciate Mrs. Sandra Harman for carefully checking and improving the format of the dissertation.

Lastly, I would like to thank my classmates, Yang Liu, Chao Zhang and Katie Vermillion, for their kind help with my coursework or research. I also learned things

from many other people in the department and enjoyed talking to them. I am thankful for their company.

CHAPTER ONE

Introduction

1.1 Formation of Stars and Protoplanetary Disks

1.1.1 Interstellar Medium

The interstellar medium (ISM) is the material and radiation that fills the space between stars in a galaxy (Herbst 1995). Approximately 99 % (in mass) of the ISM is composed of interstellar gas in ionic, atomic and molecular form, and the remaining 1 % is tiny grains of dust (Boulanger et al. 2000). Within the gas, around 70 % of the mass is hydrogen (either molecular or atomic), around 28 % is helium and the rest consists of "metal" elements with greater mass than hydrogen and helium (Ferriere 2001; Klessen & Glover 2016). The ISM can be heated by multiple sources such as cosmic rays, stellar winds and supernova explosions. In addition, dust grains can absorb ultraviolet (UV) radiation emitted from hot stars and eject electrons, which carry excess energy, and heat up the gas through mutual collisions, the so-called photoelectric heating. On the other hand, the ISM can be cooled through the de-excitation of excited atoms or molecules, during which photons are emitted and carry energy out of the region. Due to different heating and cooling processes in different regions of the ISM, the interstellar gas is typically found in three forms: a large fraction of the space is filled with hot, tenuous gas with temperature heated to $T \sim 10^6\ K$ by shocks generated by supernovae; nested in the hot medium are cold ($T < 300\ K$), dense clouds consisting of neutral atomic or molecular hydrogen, which accounts for a very small fraction of the gas; the third phase is warm ($T \sim 10^4\ K$) photoionized clouds surrounding cold clouds. These are composed of rarefied neutral and ionized gas, with much greater volume but far less mass than the cold clouds (Mckee & Ostriker 1977; Field et al. 1969). In all phases, the ISM is extremely

tenuous and devoid of matter; the particle number density is $10^{-4}\ cm^{-3}$ in hot, dilute regions, and $10^{6}\ cm^{-3}$ in cold, dense regions, much lower than any laboratory vacuum chamber on earth, where the number density is on the order of $10^{10}\ cm^{-3}$.

Matter is primarily ionized in hot regions of the ISM. Ionization occurs when a large amount of energy is provided to a gas and the electrons gain enough energy (greater than the binding energy) to become unbound from the nuclei of their parent atoms or molecules. Such a partially or fully ionized gas composed of interacting positively charged ions and free electron is called plasma, the fourth state of matter (Tonks 1967; Compton & Langmuir 1930). Plasma is electrically conductive owing to the presence of charge carriers, and its collective behavior is dominated by long-range electromagnetic fields (Morozov, 2012). As the most abundant form of mater in the universe, plasma constitutes 99% of the visible universe, and can be found naturally in stars, in space and on earth, such as the interior of the sun, solar wind, auroras, lightning and the earth's ionosphere.

In cold regions of the ISM with relatively high particle number density, the gas is mainly in the form of molecular hydrogen (Prialnik 2000). These types of interstellar clouds are called molecular clouds, in contrast to clouds of ionized gas in hot regions of the ISM. A spiral galaxy like the Milky Way contains numerous molecular clouds, as shown in Figure 1.1. Molecular clouds are the densest part of the interstellar medium, and account for 1-2% of its total volume (Ferriere 2001; Klessen & Glover 2016). The masses and sizes of molecular clouds vary: giant molecular clouds have masses of $10^3 - 10^7$ times the mass of the Sun ($M_\odot$) and sizes of 50-100 parsec (a parsec is equal to 19 trillion miles), while small molecular clouds have masses of a few hundred $M_\odot$ and sizes of a few parsec (Murray 2011). In contrast to other regions of the interstellar medium, which is mainly comprised of ionized gas, molecular clouds are cold enough for molecules to form and survive, with number densities ranging from 10^3 to 10^5 particles per cubic centimeter (Di Francesco et al. 2006).

Figure 1.1: Molecular clouds in a whirlpool galaxy. The blue features show the radiation from carbon monoxide (CO) molecules, which is used as a tracer for molecular hydrogen, the raw material for forming new stars. Stars form in the arms which contain regions with high concentration of gas and dust. Credit: PAWS Team/IRAM/NASA HST/T. A. Rector (University of Alaska Anchorage)

Molecular clouds can collapse under the gravitational force if the kinetic energy of the internal gas pressure can not balance the gravitational potential energy (Kwok 2006). The threshold mass above which a cloud will collapse is called the Jeans mass (Jeans 1902), which increases with increasing temperature and decreasing density of the cloud. However, even if the Jeans criterion is met, a cloud may still be prevented from collapsing by some other mechanisms, such as rotation and magnetic fields (Hartmann 2000; Li et al. 2009). The rotation of the clouds produces an outward centrifugal force to counteract the inward gravitational force, but in most cases the clouds are not rotating fast enough to provide sufficient support. The more important mechanism to resist collapse is magnetic fields. The magnetic force acting on charged particles ties them to the magnetic field lines, which can counteract gravitational collapse. The neutral gas particles are also hindered in collapse as long as they are collisionally coupled to the plasma. However, if the cloud is weakly ionized and there are not sufficient collisions between the plasma and neutrals, the neutrals will decouple from the plasma and fall towards the cloud core, a process known as ambipolar diffusion (Prialnik 2000; Kwok 2006).

As different regions in a molecular cloud have different densities and therefore different Jeans masses, they collapse individually, breaking the cloud into a number of smaller pieces (Prialnik 2000), as shown in Figure 1.2. The density of a molecular cloud increases by many orders of magnitude during its contraction, which decreases the Jeans mass and promotes further fragmentation of the cloud (Kwok 2006). On the other hand, the increase of density makes the fragments opaque, preventing radiation of thermal energy converted from gravitational potential energy. As a result, the cloud becomes hotter and eventually prohibits further fragmentation (Prialnik 2000). The fragments then cool and condense into rotating spheres of gas (cloud core), where star formation takes place when they contract under their own gravity (Battaner 1996).

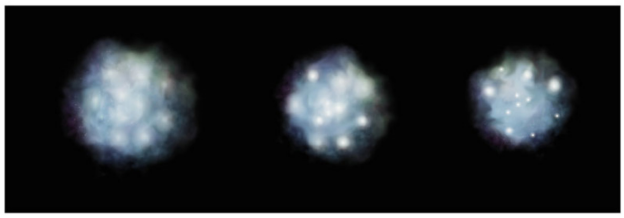

Figure 1.2: Schematic showing the fragmentation process of molecular clouds. Credit: The University of Arizona (2004).

1.1.2 Star Formation

As the protostellar cloud core continues to collapse, it passes through several phases. The first phase is isothermal collapse during which the core is transparent to radiation of infrared wavelengths. The radiation rate of thermal energy is equal to the rate of acquisition of gravitational energy, keeping the cloud temperature nearly constant (McLaughlin & Pudritz 1997). The collapse increases the cloud density, especially at the core region, increasing the optical depth of the core region, and eventually making it opaque to infrared radiation. At this point, the cloud enters the adiabatic collapse phase, in which the thermal energy can not be radiated away and the core temperature increases (Yoshida et al. 2012). When the temperature reaches $\sim 2000K$, the molecular hydrogen dissociates into hydrogen atoms, and then hydrogen

and helium atoms are ionized (Larson 1969). The energy gained from compression of the cloud is consumed in these processes, which allows further collapse of the cloud. This continues until the core reaches a critical temperature and builds up enough internal gas pressure to balance gravity, a condition called hydrostatic equilibrium. At this point, a quasi-static protostar is formed, surrounded by an envelope of gas and dust (Prialnik 2000). The temperature and density of the protostar continue increasing due to the accretion of infalling material, and deuterium fusion begins when the central temperature reaches $\sim 10^6 K$. The collapse is halted by the outward pressure caused by the production of nuclear energy, until the deuterium is depleted (Henyey et al. 1955). Then the protostar collapses again, increasing the internal temperature. Finally, hydrogen fusion is ignited in the core at a temperature of $\sim 10^7 K$, and a star is formed (Hartmann 2000).

1.1.3 Protoplanetary Disks

A natural consequence of the star formation process is the formation of a protoplanetary disk around the star, where planets are formed, as shown in Figure 1.3. During the collapse, the molecular cloud rotates faster as the radius decreases, due to the conservation of angular momentum (Armitage 2011). The gas at the equator experiences greater centrifugal force, which is proportional to the distance from the rotation axis (Feynman et al. 1963). When the centrifugal force exceeds the gravitational pull, the material spreads in the radial direction of the cloud, while continuing to collapse in the vertical direction (Pringle 1981). As a result, the cloud flattens out and forms a thin disk consisting of gas with embedded dust grains, with a radius up to 1000 AU (1 AU is defined as the distance from Earth to the Sun, equal to 149,597,870,700 meters). The disk reaches a quasi-equilibrium state when the gravitational force balances the centrifugal force in the radial direction of the cloud, and balances the gas pressure in the direction perpendicular to the disk (Mamajek et al. 2004; White & Hillenbrand 2005).

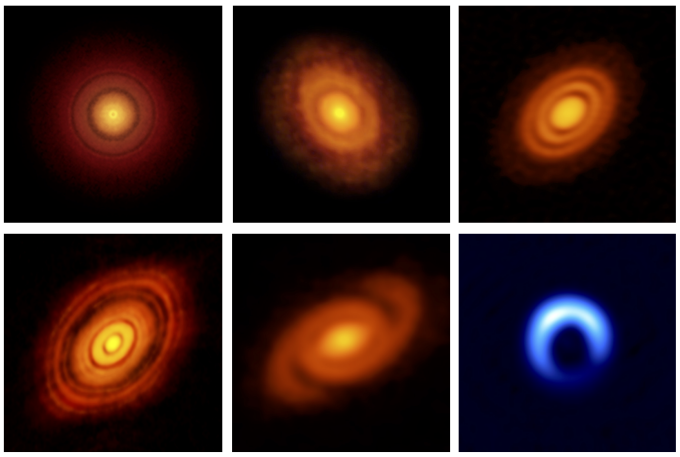

Figure 1.3: Gallery of high angular resolution continuum observations of planet forming protoplanetary disks obtained with ALMA. Credits: S. Andrews, L. Cieza, A. Isella, A. Kataoka, B. Saxton (NRAO/AUI/NSF), and ALMA (ESO/NAOJ/NRAO)

As the material in the disk orbits around the central star, it is compressed and heated by the gravitational and frictional forces, causing the emission of energy in the form of electromagnetic waves, the frequency range of which depends on the mass of the central star (Nowak & Wagoner 1991; Wagoner 2008). The orbiting particles' angular momentum is reduced during the radiation of energy, resulting in a slower velocity, which causes them to drift to a lower orbit. As particles drift inward, despite of the loss of total energy and angular momentum, their velocities are increased due to the conversion of gravitational potential energy to kinetic energy. The increased velocity causes more frictional heating, which, in turn, results in further inward spiral of particles and more radiation of energy. Since the total angular momentum of the disk is conserved, the loss of the angular momentum has to be compensated by the increase in the angular momentum of particles farther away from the center of the disk. Therefore, the angular momentum lost by the infalling material should be transported outwards to the exterior regions of the disk (Cameron 1978).

Angular momentum can be redistributed by a gravitational instability, which produces spiral density waves (Mordasini et al. 2010), and by the magnetic field caused by the central star. Since the central star rotates faster than the surrounding

disk, it will be decelerated by magnetic torques exerted by ionized gas in the disk coupled to the magnetic field lines, and transfer momentum outwards to the disk (Ji & Balbus 2013). In addition to the two mechanisms, the transport of angular momentum can also be caused by collisions between neighboring annuli: the material in an inner orbit moves faster than that in an outer orbit, and resulting collisions slow the inner material and speed up the outer material. As a result, the inner material adopts an even lower orbit while the outer material adopts a higher orbit, and momentum is transferred outwards (Dominik 2015).

Gas viscosity is responsible for the redistribution of angular momentum, as viscous stress can cause disk material to heat up and dissipate energy (Goldreich & Schubert 1967). However, the molecular viscosity itself is not sufficient for the transport of angular momentum (Kubsch et al. 2016). Instead, Shakura and Sunyaev (1973) proposed that turbulence in the gas can enhance the gas viscosity and destabilize the orbital gas motion (Ji & Balbus 2013). However, neither the level nor the origin of turbulence in PPDs are well understood. The Magnetorotational Instability (MRI; Balbus & Hawley 1998), an instability caused by the differential rotation of the conducting material in a disk, was conventionally accepted as the leading mechanism to drive turbulent flow in accretion disks (Balbus & Hawley 1991), the onset of which requires the disk to be sufficiently ionized to produce a weak poloidal magnetic field. However, only the inner regions in PPDs have large ionization fractions, and most regions beyond 0.1 AU are very weakly ionized (Hayashi 1981; Igea & Glassgold 1999), where the MRI-driven turbulence is mainly affected by non-ideal magnetohydrodynamics (MHD) effects, such as Ohmic resistivity, the Hall effect and ambipolar diffusion (AD). Different non-ideal MHD effects dominate in different regions of PPDs based on disks' density and strength of magnetic field (Bai & Stone 2013; Wardle 2007). Recent research has shown that the efficiency of the MRI is dramatically reduced with the inclusion of ambipolar diffusion, and the MRI is com-

pletely suppressed at 1 AU when ohmic resistivity and ambipolar diffusion are taken into account (Bai & Stone 2013).

An alternative mechanism for transporting angular momentum and driving disk accretion is the laminar flow driven by a magnetocentrifugal wind, which is gas outflowing from the disk that is centrifugally accelerated along magnetic field lines. The efficiency of the wind is positively related to the net vertical magnetic flux and the penetration depth of the far-ultraviolet (FUV) ionization, which depends on the extent of dust attenuation and self-shielding (Bai & Stone 2013). According to Bai & Stone (2013), the two scenarios, MRI and laminar wind, are mutually exclusive, as MRI requires a weak vertical background magnetic field, while the launching of a laminar wind requires a strong vertical field of equipartition strength (i.e., energy density in magnetic field is similar to the kinetic energy density due to turbulent motion of gas; Basu & Roy 2014) at the disk midplane. On the other hand, in non-magnetically active regions of protoplanetary disks, recent research has identified other turbulence generating mechanisms, such as the vertical shear instability, convective overstability, zombie vortex instability, and the streaming instability (Raettig et al. 2015; Johansen & Youdin 2007). The dominant hydrodynamic instability process varies in different disk locations, determined by the cooling times defined by disk opacities.

The amount of material in the disk is reduced as it spirals inward and accretes onto the central star. In addition, the material can also be removed by a variety of other processes. One typical external process is evaporation or ablation of disk material by winds from nearby luminous massive stars (Tenorio-Tagle 1996). However, compared to external processes, the internal processes play a more significant role in the disk dispersal. Photoevaporation is considered to be the major driver for removing disk material at large radial distances. As the upper layer of the disk beyond a few AU is heated to high temperatures by high-energy radiation from the central star, such as ultraviolet and X-rays, the thermal energy of the heated layer exceeds its

gravitational binding energy. This allows the gas, along with the entrained dust particles, to escape from the disk surface, forming a photoevaporative wind (Hollenbach et al. 2000; Dullemond et al. 2007; Mordasini et al. 2010).

Another internal process that contributes to the removal of disk material is planet formation. Planets are believed to form in protoplanetary disks; the dust particles embedded within the disk are the building blocks of planets. Although planet formation is not the major mechanism for disk dispersal, since observations show that the planets account for less than 1.0 % of the initial total disk mass (Wright et al. 2011; Mayor et al. 2002), the disk dispersal has a significant impact on the process of planet formation, putting strict constraints on the time scale for planet formation. The efficiency of the removal of disk material affects the growth rates as well as the chemical composition of planets. In addition, as the angular momentum exchange in the disk changes the semi-major axis (one half of the longest diameter of an ellipse) of a planet's orbit, disk clearing will halt planets' orbital migration, and therefore influence the initial architectures of planetary systems as well as the formation of giant and terrestrial planets (see section 1.2; Mordasini et al. 2010; Alexander et al. 2013).

1.2 Planet Formation

1.2.1 First Stage: from Dust Particles to Planetesimals

Planet formation is comprised of several stages. In the first stage, small dust particles with an initial size of $\sim 0.1 - 1\ \mu m$, similar to those found in the interstellar medium (Mordasini et al. 2010), collide and stick together by the Van der Waals force, which is a weak short-range interaction due to a transient shift in the electron density of atoms. After the initial fractal growth (in which particles grow by hit-and-stick collisions), the increased relative velocity between dust particles causes compaction, resulting in particles with sizes of $\sim 1 - 10\ mm$ and filling factors (the

ratio of the total volume of all constituent monomers, which are solid spherical particles, to the geometrical compound volume of the particle; Ormel et al. 2013) of ~ 0.36 (Zsom et al. 2010). The increased compactness of aggregates, which are collections of monomers, makes them less coupled to the ambient gas, increasing the relative velocities with respect to other particles. Two dust particles which collide with sufficiently high velocity rebound instead of sticking, which poses a bouncing barrier to dust growth. The maximum particle size before growth is hindered by bouncing decreases with increasing radial distance from the central star and dust-to-ice ratio (Lorek et al. 2018). The porosity (i.e., the fraction of the volume of voids within the particle) of aggregates, formed at this stage increases with increasing radial distance and decreasing constituent monomer size, as well as dust-to-ice ratio. A lower dust-to-ice ratio produces larger and more porous aggregates, because ice is stickier than dust, which increases the bouncing threshold velocity for ice particles and reduces their compaction.

There are several mechanisms that may enable the dust population to continue growing after hitting the bouncing barrier, one of which is the velocity distribution of dust particles. Both the stochastic turbulence-induced velocity (Ormel et al. 2007) and differences in drift velocities (Brauer et al. 2008) due to different porosity and mass can contribute to the variations in velocity, which enables the occurrence of fragmentation, i.e., particles colliding with large relative velocities are disrupted and break into fragments (Kataoka 2017). When small fragments hit large aggregates, part of their mass is transferred to the target, leading to further growth of large particles to planetesimal sizes ($\sim 1 - 1000\ km$; Blum 2018). The efficiency of the dust growth greatly depends on the location in the disk: particles with a size of 100 m can be formed within 5×10^4 years at 1 AU, while it takes 6×10^5 years to grow particles to a size of several meters at 30 AU (Windmark et al. 2012; Garaud et al.

2013). The longer the growth time scale, the more the particles are subject to the radial drift, which obstructs the growth (Blum 2018).

In addition to direct mutual collisions, planetesimals can also been formed through gravitational instability. This happens when a portion of the dust layer with a high mass density of solid particles and low relative velocity becomes unstable to its own gravity, and eventually collapses to a planetesimal. However, the low relative velocity of a dense dust layer may be a difficult criterion to meet, due to the differential radial drift velocity between particles of different sizes. In addition, as the dust layer revolves about the central star at a Keplerian speed, while the gas-rich layers above and below the dust layer revolve at a sub-Keplerian speed due to the gas pressure, the turbulence generated by the differential velocity can stir up the particles in the dust layer, increasing their relative velocities (Chambers 2003). On the other hand, turbulence can promote the gravitational instability by concentrating dust inside or between turbulent eddies. The onset of gravitational instability requires a solid density 2-10 times higher than that expected for material with solar composition (Youdin & Shu, 2002; Chambers 2003), and turbulence can increase the local density of solid particles by a factor of $\sim 10^3$ on the smallest turbulence scales and by a factor of up to 80 on large scales (Cuzzi et al. 2008; Johansen et al. 2006). In non-turbulent disks, particles can pile up in some regions as their migration speeds differ in different regions, like a traffic jam on a road, due to the variation in gas drag. The density of dust in the piles can be further increased as particles slow down when traveling through a dense region, and are likely to be trapped in the piles (Chambers 2003). In addition, dust particles can be concentrated with the aid of the streaming instability (a mechanism in which solid particles orbiting in a disk concentrate into clumps due to gas drag; Youdin & Goodman 2005) or in pressure bumps, such as the edge of the dead zone (an annular region in the disk where the viscosity is essentially zero, incapacitating the infall of material to the central star), the mid-plane (the region of

a disk with the greatest vertical density; Johansen et at. 2007) and the ice-line (the point in a disk at and beyond which it is cold enough for volatile compounds such as water to condense into ice grains) where the surface density is discontinuous (Brauer et al. 2008). As a result of different processes of dust growth, the solar nebular is comprised of gas, dust grains and growing planetesimals of various sizes, as shown in Figure 1.4.

Figure 1.4: Illustration of the solar nebular comprised of gas, dust grains and growing planetesimals. Credit: William K. Hartmann (Boss 2007).

1.2.2 Second Stage: from Planetesimals to Planets

Once planetesimals are formed, mutual gravitational interactions become the dominant driving mechanism for further growth of solid bodies and formation of planets. This stage of growth cannot become effective until the objects grow to planetesimal size, at which point the gravitational force is strong enough to attract surrounding particles (Blum 2010) [for small colliding particles, their collision velocities are typically much greater than the gravitational escape speed, which is the minimum speed a free object must have in order to escape from the gravitational influence of the other body]. The random velocities of planetesimals are excited by close passages between planetesimals through gravitational attraction, and damped by gas drag as well as collisions between planetesimals. The equilibrium velocity comes through a

balance of these two factors. Collisions between planetesimals are greatly affected by the random velocity: a small random velocity allows two planetesimals undergoing a close encounter to have sufficient time to adjust their trajectories and travel towards each other through mutual attraction, increasing the collision probability; on the other hand, a large random velocity reduces the effectiveness of gravitational focusing, decreasing the chance of collisions (Chambers 2003).

The random velocity of planetesimals plays an important role in different stages of the planet formation process. In the early stage, also called the runaway stage, large planetesimals have small random velocities (thus high collision probability), and grow fastest by accreting small planetesimals as well as fragments resulting from destructive collisions between small planetesimals. These eventually form protoplanets (planetary embryos), which are a few thousand kilometers in diameter (Wetherill & Stewart 1993). The second stage of planet formation is called oligarchic growth, during which the random velocities of planetesimals are stirred up by the massive embryos through gravitational perturbations. This reduces the effectiveness of gravitational focusing and slows down the runaway growth, and each embryo accretes material in its own orbital niche. In the third stage, orderly growth, the random velocities of embryos increase when the remaining planetesimals are insufficient to damp their velocities, which slows down their growth. Embryos travel across each other's orbits and collide (Kokubo & Ida, 1998). Some large protoplanets accrete massive envelopes consisting of hydrogen/helium and become giant gaseous planets, while the small protoplanets interact and excite each other's orbital eccentricity, causing their orbits to cross. As a result, they collide and form terrestrial planets (Mordasini et al. 2010). The remaining planetesimals are swept up by the planets, accreted to the central star, or ejected by the solar wind.

1.3 Dust Growth

1.3.1 Significance of Dust Collisions

Dust is the building material of the planetary system. The second stage of planet formation (described in section 1.2.2) cannot become effective until the particles grow to planetesimal size. Whether planetesimals are formed by direct collision of dust particles or through gravitational instability, the collisional growth of submicron-sized dust grains into larger aggregates is a necessary step towards further growth and eventual planet formation. The collision process determines the size and porosity of resulting aggregates. As particles with different mass-to-surface ratios have different radial drift velocities, they migrate differently in the disk and therefore change the nebular mass distribution, which affects the chemical and optical properties of the disk. In addition, in regions with high dust density, the dust properties significantly affect the ionization-recombination balance of the gas, which is important to dust charging, the accretion process, coupling of gas with magnetic fields and instability in disks (Ivlev et al. 2016; Li et al. 2014; Turner et al. 2014). The collection of electrons on dust particles also reduces the ionization degrees of the disks (Ivlev et al. 2016). Since the ionization degree determines the electromagnetic interactions between ionized species, which drive the MRI, a possible source of disk viscosity that drives the transport of disk momentum and material (Mandell 2015; Balbus & Hawley 1991), dust properties (i.e., size, dust-to-gas ratio) have a significant impact on the disk evolution by affecting the MRI level and the size as well as shape of the dead zone (Sano & Miyama 2000; Ivlev 2016). Therefore, it is important to research the collision processes between dust particles and their growth in the disks.

1.3.2 Sources of Relative Velocity

Dust particles entrained within gas in a protoplanetary disk can collide due to the relative velocities caused by a variety of processes such as turbulence, Brow-

nian motion, systematic drift, differential sedimentation, relative orbital decay or transverse motion (Wurm & Blum 1998). The dominating process varies for different particle sizes at different disk locations. However, particle porosity can alter the mass range in which a particular process becomes dominant by several orders of magnitude. In general, the smallest particles with radii smaller than $\sim 5 - 50\ \mu m$ are mainly driven by Brownian motion, resulting in relative velocities between grains smaller than $\sim 1\ mm\ s^{-1}$ (Blum 2018; Schmitt et al. 1997). As particles grow larger, turbulence, which causes stochastic motion, becomes the dominant driver for relative velocity, followed by systematic drift for even larger objects with volume $> 1\ cm^3$. Radial drift (systematic drift in the radial direction) of dust particles is caused by the difference in the orbital velocity of the dust and the gas. The gas rotates around the central star with sub-Keplerian velocity due to the support of gas pressure. Small dust particles well-coupled to the gas also move with approximately sub-Keplerian velocity, but they don't experience the pressure support. Therefore, the centripetal force acting on them is insufficient to counteract the gravitational force, resulting in an inward drift. On the other hand, large particles travel with near-Keplerian speed, due to the weak coupling to the gas. These particles experience a headwind from the slower-orbiting gas, and lose angular momentum, which also causes an inward acceleration. The radial drift velocity increases with increasing particle size for small particles ($< 1\ m$), and decreases with increasing particle size for large particles ($> 1\ m$). The maximum radial drift velocity ($\sim 100\ m/s$) is obtained for $\sim 1\ m$-diameter-particles, for which the radial drift time is much smaller than the disk lifetime. Particles of different sizes and different surface-to-mass ratios experience different radial drift velocities, which causes a relative velocity between grains driving collisions. Differential sedimentation can cause relative velocity between dust particles as particles with smaller surface-to-mass ratios sediment more quickly to the

midplane, due to less friction from the gas. The efficiency of sedimentation is related to the elevation above the midplane and the gas density (Blum 2018).

1.3.3 Charge

Most of the previous studies on dust coagulation are limited to neutral environments (Ormel et al. 2007, Krijit 2015), in which the particles are not charged. However, the absorption of cosmic rays, stellar X-rays and radionuclides in the disk material can cause weak ionization of the gas in the midplane of the disk (Okuzumi et al. 2011a,b). Dust particles in such an environment capture ions and electrons, and become negatively charged due to the higher thermal electron velocities compared to that of ions. The Coulomb interactions between colliding pairs can significantly alter collision outcomes, as the trajectories and orientations of the colliding particles can be altered by the electrostatic force acting between them. The deflection and deceleration can cause the colliding dust particles to miss each other, affecting the coagulation probability (Matthews et al. 2012; Okuzumi 2009; Okuzumi et al. 2011a,b). Collisional growth is strongly inhibited (or halted) by electric repulsion between colliding aggregates in locations with weak turbulence (disk radius $r \leqslant 20$ AU or scale height $|z| \leqslant 2H$; Okuzumi 2009). In addition, the charge also impacts the porosity of the resulting dust aggregates as the decreased relative velocity can reduce restructuring.

1.3.4 Collision Outcomes

When two particles collide, the possible collision outcomes include sticking, bouncing, compaction, fragmentation, erosion, mass transfer, cratering, abrasion, melting and vaporization, as determined by the collision energy (Guttler et al. 2010; Dominik & Tielens 1997; Chokshi 1993; Blum & Munch 1993; Kothe 2016; Wurm et al. 2005a; Seizinger et al 2013; Krijt et al. 2015). During the initial stage of the aggregate growth process, sub-micron-sized particles are mainly driven by Brownian

motion and have low relative velocity. They hit and stick at the point of contact through van der Waals forces (Meakin 1988), increasing the porosity of the resulting aggregates. As aggregates grow larger, they develop greater relative turbulent velocities, in which case compaction or fragmentation can take place, dissipating kinetic energy in the form of elastic waves. Particles with great size differences tend to have large relative velocities, but even with a velocity higher than the fragmentation velocity threshold, it is difficult to cause catastrophic fragmentation of the larger particle when the ratio of the mass of the projectile to that of the target is much less than one. Instead, collisions between particles differing greatly in size can cause erosion, mass transfer or cratering.

1.3.5 Growth Barriers

The main factors that limit the growth of dust through collisions are the low velocity threshold for bouncing and the low collision energy required for compaction (Blum 2018). As a result, bouncing takes place before the particles are able to grow to a large size, and compaction promotes the radial drift of the dust particles (i.e., particles decouple from the pressure-supported gas disk and drift inward by transferring angular momentum to the surrounding gas; Whipple 1972; Weidenschilling 1977). In addition to the bouncing barrier and radial drift barrier, dust aggregates also have to overcome other barriers to growth such as erosion, fragmentation and the electrostatic barrier for charged particles, before becoming planetesimals. The threshold velocity for bouncing, erosion or fragmentation depends on not only the impact energy, but also the material, monomer size and the porosity of colliding bodies.

Material with greater stickiness has a higher force of rolling friction, which reduces the amount of compaction, resulting in higher porosity of particles (Gundlach & Blum 2015). The bouncing barrier can be alleviated for particles made of stickier material or covered by frost coatings in cold regions. Ice is stickier than silicate material, but can only form icy planetesimals, like comets, beyond the snowline. For regions

interior to the snowline, some research suggests that organic matter mantling the silicate grains can act as a glue, increasing the stickiness and holding them together. Such organic-mantled-grains (OMG) are found in chondritic porous interplanetary dust particles (Homma et al. 2019; Flynn 1994). The irregular shape of particles also increases the critical bouncing velocity. For example, spherical silica grains stick at velocities lower than 1 ms^{-1}, while silica aggregates can stick at velocities up to 50 ms^{-1} (Poppe et al. 2000; Chambers 2003). In addition, charge exchange and formation of dipoles during collisions can increase the sticking forces between particles with radii of several hundred microns by around 1000 times (Marshall & Cuzzi, 2001; Chambers 2003).

The high stickiness of material not only reduces the compaction and bouncing, but also alleviates the fragmentation barrier. For example, particles made of ice have a much higher threshold velocity for fragmentation than refractory particles, such as oxides, metals and silicates (Dominik & Tielens 1997; Wada et al. 2013). In addition to the material, the constituent monomer size also has a great impact on the fragmentation. Aggregates consisting of smaller monomers have a higher fragmentation barrier than those with larger monomers. In the simulation of OMG aggregates, the fragmentation threshold increases from 10 ms^{-1} for particles with 0.3-μm-radius-monomers to 100 ms^{-1} for monomer radii of $\sim$ 0.02 μm, at 140 K (Homma et al. 2019). In addition to fragmentation, particles with small constituent monomers are more resistant to compaction, resulting in fluffier aggregates (Wada et al. 2009; Okuzumi et al. 2012; Kotaoka et al. 2013).

In addition to forming planetesimals by gravitational instability, as discussed in Section 1.2.1, another possible way to get around these growth barriers is through piling up of dust by mechanisms mentioned in Section 1.2.1. Particles in regions with high number density have lower relative velocities, which make them less subject to

destructive collision such as bouncing and fragmentation. The high dust density also enables them to grow quickly, reducing the radial drift barrier.

1.3.6 Porosity

The porosity of aggregates plays an important role in alleviating or enhancing the growth barriers. Compact aggregates are more likely to bounce or fragment than fluffy aggregates, because compact aggregates have a much higher average coordination number, i.e., the number of contacts per monomer, than porous aggregates, making it more difficult to dissipate the collision energy through restructuring (Wada et al. 2011; Seizinger & Kley 2013). However, fluffy aggregates are more subject to erosion than compact aggregates, as the erosion threshold decreases with decreasing coordination number (Dominik & Tielens 1997). Particles with high porosity have a larger capture cross section compared to compact particles of the same mass, which increases the collision rate, resulting in a faster growth of dust population. Both the relatively short growth time scale ($\sim 10^4$ years) and the porous structure of particles (strong coupling to the gas) reduce the adverse impact of radial drift on the dust growth (Krijt et al. 2015; Lorek et al. 2018; Blum 2018). On the other hand, compaction increases the mass-to-surface-area ratio of aggregates, making them less coupled to the ambient gas, resulting in higher drift velocities and greater collision energy relative to those for porous aggregates of the same mass (Okuzumi et al. 2011a,b). The high collision energy helps to reduce the electrostatic barrier for charged particles (Okuzumi 2009), but may cause other types of growth barriers such as bouncing and catastrophic fragmentation. In addition, the large vertical velocity of compact particles catalyzes their settling to a mid-plane dust layer (Ormel et al. 2007), and the piling up of dust particles speed up the growth. Therefore, the porosity of the aggregates greatly impacts these processes and also affects the collision efficiency. In addition, the charging of aggregates strongly depends on the open area of the aggregates, i.e., more porous aggregates have a higher charge than more compact

aggregates of the same mass in the same environment (Matthews et al. 2012), and affects the ionization rate of the disk. Okuzumi (2009) pointed out that the ionization degree of the disk is kept low in fractal dust growth, owing to the porous structure of aggregates, in contrast to other findings that the dust growth increases the ionization degree (Sano et al. 2000, Ivlev et at. 2016). Moreover, the porosity affects the temperatures and emission characteristics of aggregates (Greenberg & Hage 1990), and the surface area for chemical reactions taking place in PPDs (Ehrenfreund 2003). It also greatly affects the optical properties of dust, such as the scattering and absorption opacities, influencing the appearance of PPDs (Kirchschlager & Wolf , 2014; Krijt et al. 2015). In conclusion, the porosity of aggregates has significant impact on the collision processes and the evolution of the disks. Therefore, it is important to take it into consideration in the coagulation model.

Various processes, either collisional or non-collisional, can alter the porosity of aggregates (Krijt et al. 2015). Depending on the ratio of impact energy to the rolling energy (the energy needed for one monomer to roll a distance of one-half circumference on the surface of the other monomer), the porosity of the resulting aggregates can either be increased or decreased upon collision. Figure 1.5 shows three examples of the resultant aggregates formed from collision between two aggregates with different relative velocities. At the lowest relative velocity, the particles hit and stick, resulting in a very fluffy aggregate (Figure 1.5b). Larger relative velocity causes restructuring of the aggregates (Figures 1.5c and 1.5d), with greater restructuring resulting in a more compact aggregate as the relative velocity increases. Non-collisional mechanisms for decreasing porosity include the gas-compaction and compaction by self-gravity, which can happen when the pressure from the surrounding gas or from an aggregate's own gravity exceeds the external pressure it can withstand (Kataoka et al. 2013; Krijt et al. 2015).

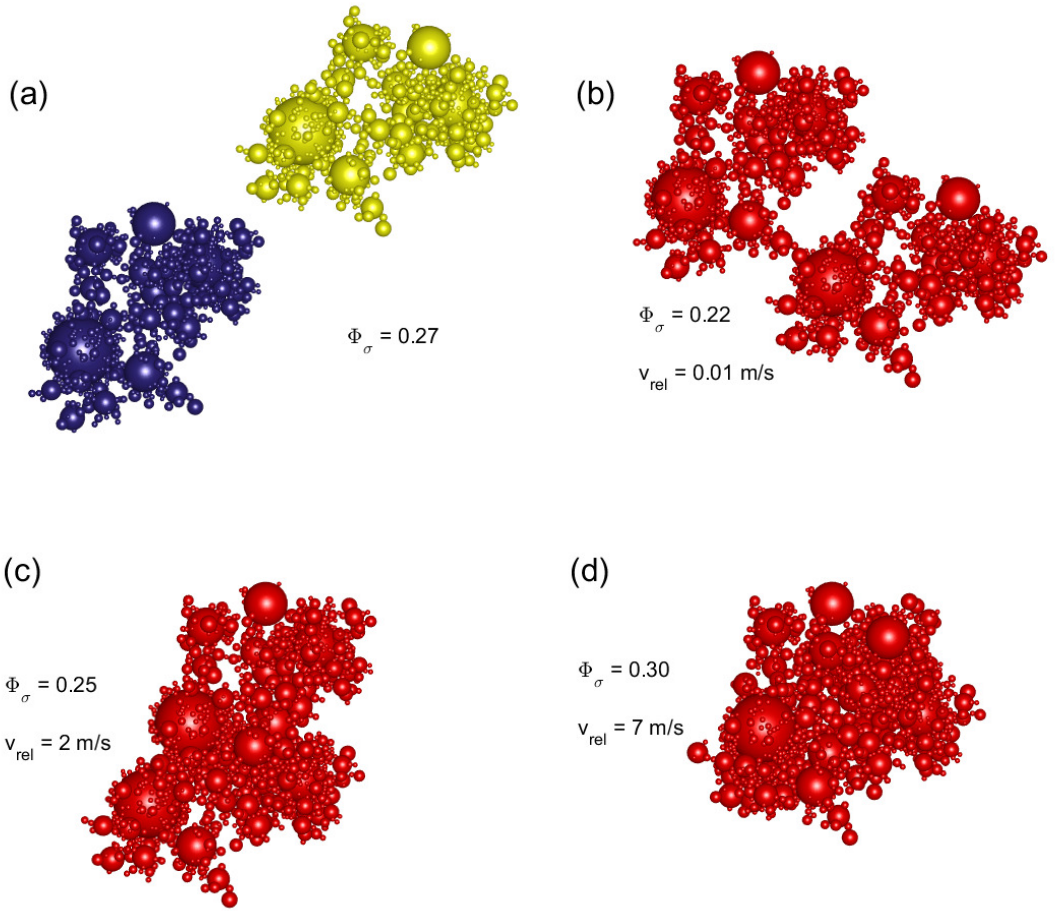

Figure 1.5: Illustration showing aggregates formed at different relative velocities. a) shows the two initial (identical) colliding aggregates. b), c) and d) show the resulting aggregate after collision with relative velocity equal to 0.01 ms^{-1}, 2 ms^{-1} and 7 ms^{-1}, respectively. The compactness factor Φ_σ is shown for each aggregate. Acknowledgement to Dr. Nina Gunkelmann for providing the LIGGGHTS code.

1.3.7 Previous Work

Early models of dust coagulation assumed hit-and-stick collisions (Meakin 1988) and fixed internal density (i.e. a compact sphere) (Weidenschilling 1980; Nakagawa et al. 1981). The hit-and-stick model works well for low collision velocities, but fails for high relative velocities, which lead to other collision outcomes (e.g., restructuring and fragmentation) due to excessive collision energy. The microphysics of coagulation between two elastic spheres was studied in detail by Chokshi (1993), who derived critical sticking and fragmentation energies as a function of particle sizes, velocities and material properties. The first experimental research on bouncing and fragmenta-

tion was conducted by Blum and Münch (1993). Since then, an extensive parameter space (particle size, mass ratio, impact velocity, grain material) has been researched, and various collision outcomes have been modeled theoretically and experimentally (Blum 2018): compaction (Dominik & Tielens 1997; Blum & Wurm 2000; Paszun & Dominik 2009; Wada et al. 2008); bouncing (Zsom et al. 2010; Heißelmann et al. 2007); erosion (Krijt et al. 2015; Schrapler & Blum 2011; Schrapler et al. 2018); mass transfer (Wurm et al. 2005b; Teiser & Wurm 2009); cratering (Wurm et al. 2005a; Paraskov et al. 2007); and fragmentation (Brauer et al. 2008; Birnstiel et al. 2012).

Although some of these studies have factored in the porosity of particles, most of them are limited to neutral environments with uncharged grains. The properties of charged dust particles have recently been receiving more attention (Matthews et al. 2012, 2015; Okuzumi 2009; Okuzumi et al. 2009, 2011a,b). Okuzumi (2009) modeled collisions between aggregates of a fixed mass ratio formed of monodisperse spherical monomers, with the collision outcome limited to hit-and-stick. However, the dust in a PPD has a size distribution, generally taken to be a power law distribution $n(r)dr \propto r^{-3.5}dr$, where $n(r)dr$ is the number of particles in the size interval $(r, r + dr)$ [the Mathis, Rumpl and Nordsieck (MRN) distribution for material in the ISM; Mathis et al. 1977]. Assuming monodisperse monomers limits the diversity of the aggregate structures, which has a significant impact on the dust growth process. In this study, we extend the analysis of the porosity of aggregates by considering an initial population of spherical monomers with radii ranging from 0.5 to 10 μm, with a MRN size distribution. A population of aggregates is built self-consistently by considering the probability of collisions between particles of all sizes present in the population. A detailed model of the collision process, which takes into account two key physical characteristics (porosity and charge), is used to resolve the collision outcome.

1.4 Formation of Chondrules and FGRs

1.4.1 Meteorites

Meteorites are pieces of fragment from comets, meteoroids or asteroids, which are rocky objects orbiting the sun formed from shattered remnants of parent planetesimals. Based on the constituent material, meteorites can be classified as stony meteorites (composed of rocky material), iron meteorites (composed of iron-nickel alloys) and stony-iron meteorites (a mixture of silicate minerals and iron-nickel metal). Stony meteorite is the most common type among the three, accounting for 94% of the meteorites (Reynolds 2004). This type can be further divided into chondrite and achondrite, depending on whether or not a meteorite contains chondrules, which are formerly molten, quasi-spherical, (sub)millimeter-sized silicate grains. Because the parent bodies of chondrites formed throughout a wide range of the solar nebula with varying material distribution and went through different thermal processing, they have different chemical properties and physical structures. Based on the mineralogy, petrology, bulk chemical composition, and the oxygen isotopic compositions, chondrites can be classed as carbonaceous chondrites, enstatite chondrites, unequilibrated ordinary chondrites and equilibrated chondrites (metamorphic rocks; Van Schmus & Wood 1967; Clayton & Mayeda 1989).

1.4.2 Chondrules

Most chondrules are composed of the ferromagnesian olivine and low-Ca pyroxene grains (Lauretta et al. 2006), embedded in glass or crystalline minerals, although the proportion of each material varies between chondrules. Chondrules were formed from fluffy dust balls during violent, high temperature events ($\sim 1000K$), such as direct radiation from the protosun, nebular lightning, magnetic flares, meteor ablation, the occurrence of shock fronts resulting from gravitational instabilities (Boss et at, 2005) and collisions between molten planetesimals. Dust aggregates are rapidly

heated and melted into droplets that quickly cool into sub-millimeter-sized quasi-spherical balls (Cuzzi et al. 2006). The textures of chondrules show evidence of rapid cooling after being molten: chondrules with porphyritic texture cooled more slowly than those with radial or barred textures, but still on a timescale of hours. Chondrule textures also show that more than 25% of chondrules were melted more than once (Rubin & Krot, 1996).

1.4.3 Fine-Grained Rims

Chondrules in carbonaceous chondrites are commonly surrounded by fine-grained dust rims (FGRs). FGRs have been observed in both optical and scanning electron microscopy studies of carbonaceous chondrites, and are particularly visible in CM chondrites (Ashworth 1977, Metzler et al. 1992, Brearley 1993). A sample of a rimmed chondrule is shown in Figure 1.6. Some research proposes that FGRs were formed in the parent body environment, either by attachment and compaction of dust onto chondrules in regolith (Sears et al. 1993, Trigo-Rodriguez et al. 2006, Takayama & Tomeoka 2012), or through pervasive aqueous alteration of chondrules (Sears et al. 1993, Takayama & Tomeoka 2012). However, most researchers believe that fine-grained dust rims were formed by accretion of grains onto the underlying chondrule cores in a nebular setting, before the rimmed chondrules were incorporated into their parent bodies (Metzler et al. 1992, Mofill et al. 1998, Brearley et al. 1999).

1.4.4 Significance of Research on Chondrules and FGRs

Chondrules are the primary constituents of ordinary and enstatite chondrites: ordinary chondrites contain 60-80% chondrules. Since chondrites are the most common type of meteorites that fall to Earth (80% of meteorites that fall to earth are ordinary chondrites), most of the meteorites collected on the earth are composed of chondrules. They are valuable goelogic specimens that represent primitive pre-planetary materials, as our only direct evidence of the conditions present in the early

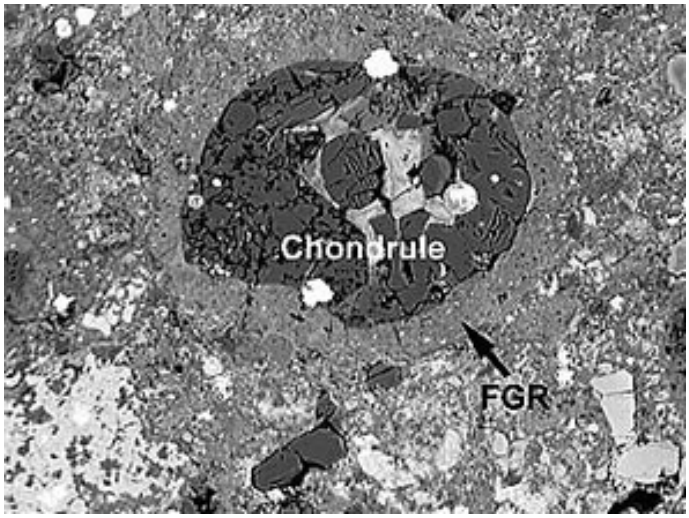

Figure 1.6: A chondrule surrounded by fine-grained dust rims in a sample of the Murray chondrite meteorite. Credit: Dante Lauretta.

PPD comes from meteorites, the parent bodies of which are thought to have formed early in the solar system. By studying the textures, mineral compositions and isotopic effects of chondrule samples, we can interpret their thermal histories and gain information about the nebular environment that existed billions of years ago. The collisions between chondrules, condensates and refractory residues after evaporation form nebular sediments, which are the building blocks of the planetary system. Chondrule FGRs may have acted as a "glue" that facilitated accretion of many rimmed chondrules into centimeter-sized objects, possible precursors to asteroids (Ormel et al. 2008). Along with refractory components such as calcium-aluminum inclusions, and a matrix made up of both crystalline and amorphous grains, rimmed chondrules encode valuable information regarding early processes in our solar system.

1.4.5 Previous Work

Previous modeling approaches to the problem of FGR formation are few but varied. Morfill et al. (1998) integrated an evolution equation for the radius of a rimmed chondrule, assumed to be suspended in a dusty-gaseous medium, and using a prescribed sticking efficiency between dust and chondrule. Cuzzi (2004) used a semi-

analytical model to calculate rim volume as a function of chondrule volume under constant and variable dust densities. Ormel et al. (2008) employed a sophisticated Monte Carlo method to study inter-chondrule sticking in parameterized turbulence. They modeled the compaction of porous dust layers based on experimental and theoretical results from the physics of dust collisions (Chokshi et al. 1993, Dominik & Tielens 1997, Blum & Schrapler 2004). Carballido (2011) performed simulations of dust sweep-up by chondrules in a local, magnetohydrodynamic (MHD), turbulent model of the solar nebula (SN), following the approach of Morfill et al. (1998). However, since the turbulence in Carballido (2011) was generated by the magnetorotational instability under *ideal* MHD conditions, the turbulent regime needs to be revised in light of recent results indicating that *non*-ideal MHD effects lead to much weaker turbulence than in the ideal MHD case (Bai & Stone 2013, Bai 2013). However, all these models didn't resolve the actual rim structure, and assumed that the dust grains comprising the rims are electrically neutral.

1.4.6 Effect of Charge on FGR Formation

As mentioned above, the trajectories of colliding dust grains can be altered by the electrostatic force acting between the grains, affecting their coagulation probability as well as their impact velocity (Matthews et al. 2012, 2016; Ma et al. 2013; Xiang et al. 2017a). The electrostatic force therefore influences the structure of the dust rim (porosity, monomer size distribution, etc.), as well as the time scale of rim formation. The effect of dust charge on this process is modified by the turbulence strength, as dust grains entrained in solar nebula regions with relatively strong turbulence have a greater probability of overcoming the electrostatic barrier, and hence reaching the rimmed chondrule surface. The collection of dust particles can be inhibited by the increasing Coulomb repulsion force, and the strength of the electrostatic barrier is roughly proportional to the aggregate size (Okuzumi 2009; Okuzumi et al. 2011a,b). For these reasons, as in the case of dust coagulation, it is important to take

into account grain charge in models of FGR formation. If the nebular hypothesis is correct, the resulting FGR structure could ultimately be used to infer values of gas velocities, turbulent viscosity, and ionization state of the solar nebula (Ormel et al. 2008; Matthews et al. 2012; Okuzumi 2009).

1.5 This Work

Studies are needed which consider all the important factors, i.e., the diversity of particle size, porosity, charge (repulsion and rotation), and turbulence, in a single model of dust growth in a protoplanetary disk. These factors influence each other and come together to determine the collision process. In order to reflect more realistic coagulation process, all of these factors are incorporated into a single numerical model. The subsequent evolution of the dust population is analyzed to determine how these factors affect the growth of dust aggregates and FGRs. In this work, an N-body code, Aggregate Builder (AB), is developed to simulate collisions between dust particles and between dust and chondrules, taking into consideration detailed collisional physics, i.e., the morphology of the aggregates/dust rims, the trajectory of the incoming particle, and the electrostatic interactions, etc. At the same time, a Monte Carlo algorithm is used to randomly select colliding particles as well as determine the elapsed time interval between collisions. Aggregate growth and FGR formation are compared in environments with different turbulence strengths and different plasma conditions, characterized by the dimensionless hydrodynamical viscosity parameter α and dust surface potentials, respectively. The values chosen are relevant for many regions of a protoplanetary disk. The goal of this work is to quantify the physical characteristics and timescales of dust aggregates/FGRs over a range of nebular conditions, and investigate the interplay between the effects of charge and turbulence on their evolution (Xiang et al. 2019c).

This dissertation is organized as follows:

Chapter Two presents the physical processes considered in this work, including charging of particles and relative velocities due to turbulence. Section 2.1 provides details on the plasma basics, charging currents, Orbital-Motion-Limited (OML) theory for the charging of spherical grains as well as the Orbital-Motion-Limited Line-of-Sight approximation (OML_LOS) for charging of irregular surfaces, and its application in calculating the charge distribution on dust particles and chondrule rims. Section 2.2 gives an overview of the motion of dust in a turbulent protoplanetaty disk, including the relative velocities and collision outcomes for grains embedded in turbulent gas flow.

Chapter Three describes the numerical treatment of dust evolution and FGR growth on chondrule parent bodies. A detailed Monte Carlo method is employed, which uses a Monte Carlo algorithm to randomly select colliding dust particles as well as determine the elapsed time interval between collisions, and an N-body code AB is used to model the detailed collision process at close approach as well as determine the collision outcome. A discussion about the disk parameters, plasma conditions and turbulence levels used in this simulation concludes the chapter.

Chapter Four presents the results from simulations of dust coagulation, investigating the effects of turbulence strength and particle charge on the coagulation process, and comparing three different collision types: PPA (particle-particle aggregation), PCA (particle-cluster aggregation) and CCA (cluster-cluster aggregation). The resulting characteristics of the dust aggregates including the monomer size as well as porosity and the time evolution of the dust population in different environments are presented, an the relationship between the properties of colliding particles and the collision outcomes is analyzed.

This chapter was submitted as [199]: Chuchu Xiang, Lorin S. Matthews, Augusto Carballido, Truell W. Hyde, " Detailed Model of the Growth of Fluffy Dust Aggregates in a Protoplanetary Disk: Effects of Nebular Conditions," arXiv:1911.04589.

LSM devised the project and developed the Aggregate-Builder code. CX modified the code to detect bouncing collisions and collect statistics on each pair interaction. CX also modified the OML_LOS method for large aggregates in order to speed up the computation, so that the blocked portion of an aggregate is calculated in each test direction instead of calculating the LOS factor for each patch. The Monte Carlo code was originally written by AC. CX modified this code for computational expediency and to allow for larger dust populations by assigning a weight to each particle and grouping dust particles into bins. CX performed the numerical simulation, analyzed the results and drafted the manuscript under LSM's guidance. LSM supervised the project, enriched and reorganized the content, and worked on improving presentation of the results. AC rewrote the introduction. TWH provided advice on the research problems. All authors revised the manuscript and discussed the results.

Chapter Five presents the simulations of dust rim growth on a chondrule surface through the collection of dust grains in an electrically neutral environment. The effects of turbulence strength and chondrule size on rim growth, as well as the difference between rims formed by accretion of dust monomers (particle aggregation) and rims formed by accretion of dust aggregates (cluster aggregation) are investigated, by analyzing the rim structure, porosity as well as the formation time.

This chapter was published as [200]: Chuchu Xiang, Augusto Carballido, Romy D. Hanna, Lorin S. Matthews, Truell W. Hyde, "The initial structure of chondrule dust rims I: Electrically neutral grains," Icarus 321, 99-111 (2019). LSM and AC conceived the study. The Aggregate-Builder code was originally developed by LSM. CX modified the code to simulate dust rim growth on a chondrule body, expanding the collision outcomes to include restructuring (due to rolling on the surface) and bouncing. The Monte Carlo code was originally written by AC. CX modified the code to randomly select particles (dust) from a population of grains or aggregates to collide with a fixed particle (chondrule). CX also modified the code to assign a weight to each

particle and group dust particles into bins for computational expediency. CX ran the code, analyzed the results, prepared the figures and wrote the initial manuscript with support from LSM, AC and TWH. LSM directed the study, supervised the findings of this work and designed figures for further exploration of the results. AC rewrote part of the introduction, worked on better explaining the results and wrote the section on comparison with previous work. HR carried out the experiments and wrote the section on comparison with experimental measurement. TWH provided advice on the research direction and data presentation. All authors revised the manuscript and contributed to the interpretation of the results.

In Chapter Six, the model presented in Chapter Five is expanded to examine the growth of FGRs under different plasma conditions, where both the chondrules and dust particles are charged to varying degrees. The manner in which the charge affects the rim structure (porosity, monomer size distribution, etc.) as well as the time to build the rims is examined. It is shown that the impact of the charge changes with varying turbulence levels and chondrule sizes.

This chapter was submitted as [201]: Chuchu Xiang, Augusto Carballido, Lorin S. Matthews, Truell W. Hyde, "The initial structure of chondrule dust rims II: charged grains," arXiv:1911.00981. The Aggregate-Builder code was originally developed by LSM. CX modified the code to simulate dust rim growth on a chondrule body. CX also modified the OML_LOS method to charge a dust pile and duplicate it on the rest of the chondrule surface. CX ran the code, performed the analysis and wrote the initial manuscript with support from LSM, TWH and AC. LSM designed and supervised the project. LSM also reorganized the paper, improved the text and figures, and provided advice on refining presentation of the data. All authors discussed the research problems, revised the manuscript and contributed to the interpretation of the results.

The conclusions drawn from this work are summarized in Chapter Seven, which gives an overview of the impact of the charge and turbulence on the evolution of dust population and FGRs in the disks. A discussion about the future work that can be done to extend this study to further our understanding of this subject concludes the dissertation.

Some content in this chapter was published in Xiang et al. 2017a, 2017b, 2019a, 2019b, 2019c.

CHAPTER TWO

Physical Processes in Charging and Coagulation of Grains in Protoplanetary Disks

2.1 Grain Charging

2.1.1 Ionization of Gas in PPD

In many regions of a protoplanetary disk, the gas is weakly ionized by thermal collisions of the atoms at high temperature with gas heating, caused by multiple sources such as cosmic X-rays, gamma rays from the new star, radioactive decay and ultraviolet stellar radiation. The electrons freed from the atomic orbits form an electron gas cloud. This, together with the surrounding ions and the neutral atoms, forms plasma.

The relationship between the degree of ionization and the gas temperature was first postulated by Saha. In addition, the degree of ionization also depends on the density and ionization energies of the atoms. Let E_a and E_b be the energies of state a and state b, with statistical weights (degeneracy) g_a and g_b, respectively. The number of particles in state i, N_i, and that in state j, N_j satisfy the Boltzman equation,

$$\frac{N_a}{N_b} = \frac{g_a}{g_b} exp(-(E_a - E_b)/kT). \tag{2.1}$$

For ions in the i_{th} and $(i+1)_{th}$ states of ionization, their number density ratio, n_{i+1}/n_i, is acquired by integrating the Boltzman equation in the momentum space of free electrons,

$$\frac{n_{i+1} n_e}{n_i} = \frac{(2\pi m_e k_B T)^{3/2}}{h^3} \frac{2 g_{i+1}}{g_i} exp\left(-\frac{\epsilon_{i+1} - \epsilon_i}{k_B T}\right) \tag{2.2}$$

where n_e amd m_e is the number density and mass of electron; T is the temperature of the gas; k_B and h are the Boltzmann constant and the Planck's constant, respectively; g_i and g_{i+1} are the degeneracy of the two ions; and ϵ_i and ϵ_{i+1} are the energies required

to remove i and $i+1$ electrons from the atom. This is the so-called Saha equation, often used to determine the ratio of number density of different ion species (Saha 1920).

2.1.2 Debye Shielding

Assuming the plasma is collisionless and considering each plasma species β as a "fluid" with temperature T_β, number density n_β, mean velocity $\vec{v}_\beta$ and pressure $P_\beta = k_B n_\beta T_\beta$, where k_B is the Boltzmann constant, the equation of motion for each fluid reads as (Bellan 2008)

$$m_\beta \frac{d\vec{v}_\beta}{dt} = q_\beta \vec{E} - \frac{\nabla P_\beta}{n_\beta}, \tag{2.3}$$

where m_β and q_β are the mass and charge of the particle, and $\vec{E}$ is the electric field. For a slow perturbation, i.e., $d\vec{v}_\beta/dt \approx 0$, $\vec{E} \approx -\nabla\phi$, and $\nabla P_\beta \approx k_B T_\beta \nabla n_\beta$, Eq. 2.3 can be reduced to (Bellan 2008)

$$n_\beta q_\beta \nabla\phi \approx -k_B T_\beta \nabla n_\beta, \tag{2.4}$$

which solution is given by

$$n_\beta = n_{\beta,0} exp\left(-\frac{q_\beta \phi}{k_B T_\beta}\right), \tag{2.5}$$

where $n_{\beta,0}$ is the number density of plasma species β at infinity.

Suppose a test charge Q is slowly inserted into an initially neutral plasma in which electrons and ions are uniformly distributed with a zero electric potential. With the perturbation of the test charge, the plasma is brought out of the equilibrium state, i.e., the nearby particles with the same polarity as the test charge are repelled and those with opposite polarity are attracted towards to the test charge. The charge cloud surrounding the test charge has an opposite charge from the test charge, and therefore partially cancel the electric field caused by the test charge, a mechanism called *screening*. The resulting local potential ϕ is calculated using the Poisson's

equation,

$$\nabla^2\phi = -\frac{\rho}{\varepsilon_0}, \tag{2.6}$$

with ρ the net charge density, contributed by both the test charge and the screening charge cloud,

$$\rho = Q\delta(\vec{r}) + \sum_\beta n_\beta(\vec{r})q_\beta, \tag{2.7}$$

where the origin of the coordinate is located at the center of the test charge. As the perturbation is slow, the nearby particles have a Boltzmann distribution given by Eq. 3.6. Using the Taylor expansion, Eq. 3.6 can be rewritten as

$$n_\beta = n_{\beta,0}\left(1 - \frac{q_\beta\phi}{k_BT_\beta} + \frac{(q_\beta\phi/k_BT_\beta)^2}{2!} + ...\right). \tag{2.8}$$

Since the electric potential energy caused by the perturbation is small compared to the thermal energy of the plasma species, $|q_\beta\phi| \ll k_BT_\beta$, Eq. 2.8 can be approximated by keeping the first order term,

$$n_\beta \approx n_{\beta,0}\left(1 - \frac{q_\beta\phi}{k_BT_\beta}\right). \tag{2.9}$$

Substituting Eqs. 2.7 and 2.9 into Eq. 2.6, and using the initial neutrality of the plasma, i.e., $\sum_\beta n_{\beta,0}(\vec{r})q_\beta = 0$, one obtains

$$\begin{aligned}\nabla^2\phi(\vec{r}) &= -\frac{1}{\varepsilon_0}\left[Q\delta(\vec{r}) - \phi(\vec{r})\sum_\beta \frac{n_{\beta,0}q_\beta^2}{k_BT_\beta}\right] \\ &= -\frac{1}{\varepsilon_0}\left[Q\delta(\vec{r}) - \frac{\phi(\vec{r})}{{\lambda_D}^2}\right],\end{aligned} \tag{2.10}$$

where λ_D is the Debye length, defined as

$$\frac{1}{{\lambda_D}^2} = \sum_\beta \frac{1}{\lambda_\beta^2}, \tag{2.11}$$

with the Debye length λ_β of species β given by

$$\lambda_\beta^2 = \frac{\varepsilon_0 k_BT_\beta}{n_{\beta,0}q_\beta^2}. \tag{2.12}$$

The Laplacian operator in spherical coordinates can be written as

$$\nabla^2 = \frac{1}{r^2}\frac{\partial}{\partial r}\left(r^2\frac{\partial}{\partial r}\right) + \frac{1}{r^2 sin\theta}\frac{\partial}{\partial\theta}\left(sin\theta\frac{\partial}{\partial\theta}\right) + \frac{1}{r^2 sin^2\theta}\frac{\partial^2}{\partial\phi^2}. \tag{2.13}$$

Assuming the electrostatic potential $\phi(\vec{r})$ is spherically symmetric, only the radial term in Eq. 2.13 is nontrivial,

$$\nabla^2 = \frac{2}{r}\frac{\partial}{\partial r} + \frac{\partial^2}{\partial r^2}. \tag{2.14}$$

Substituting Eq. 2.14 into Eq. 2.10 yields

$$\frac{\partial^2\phi(r)}{\partial r^2} + \frac{2}{r}\frac{\partial\phi(r)}{\partial r} - \frac{\phi(r)}{\lambda_D^2} = -\frac{Q\delta(\vec{r})}{\epsilon_0}. \tag{2.15}$$

For $r > 0$, Eq. 2.15 reduces to

$$\frac{\partial^2\phi(r)}{\partial r^2} + \frac{2}{r}\frac{\partial\phi(r)}{\partial r} - \frac{\phi(r)}{\lambda_D^2} = 0, \tag{2.16}$$

which has solutions

$$\phi(r) = \frac{C}{r}exp\left(\pm\frac{r}{\lambda_D}\right). \tag{2.17}$$

The constant C is determined by reducing the solution to the Coulomb potential of a point charge in vacuum for $r \ll 1$,

$$C = \frac{Q}{4\pi\varepsilon_0}. \tag{2.18}$$

Since the solution which contains $exp(r/\lambda_D)$ explodes as r increases, contradictory to the screening effect, the final solution becomes

$$\phi(r) = \frac{Q}{4\pi\varepsilon_0 r}exp(-\frac{r}{\lambda_D}). \tag{2.19}$$

Eq. 2.19 shows that the electrostatic potential caused by the test charge and the surrounding charge cloud that participates in the screening decays exponentially as the distance from the test charge increases. For $r \gg \lambda_D$, the test charge is completely screened by the surrounding plasma particles which have opposite polarity as the test particle.

As can be seen in Eq. 2.12, the Debye length increases with increasing thermal energy $k_B T_\beta$ and decreasing plasma density $n_{\beta,0}$, as a greater thermal energy causes particles in a larger region to be affected by the perturbation and a low plasma density reduces the efficiency of the Debye shielding (Conde 2018). The shielding mechanism works only if there are sufficient plasma particles in the cloud, $4\pi n_{\beta,0}\lambda_D^3 \gg 1$ (Bellan, 2008). In addition, the derivation above is based on the assumption of a small perturbation. In case of large perturbation, i.e., $|q_\beta \phi| > k_B T_\beta$, additional terms in Eq. 2.8 are needed, and a different solution is obtained from the nonlinear Possion's equation (Conde 2018).

2.1.3 Quasi-Neutrality

As discussed above, for an outside observer far away from the test charge, the perturbation is completely shielded and the plasma appears to be neutral. However, at a small scale comparable to the Debye length, the neutrality breaks down due to the local nonuniform charge distribution. Here we validate the assumption of initial neutrality of plasma without a perturbation, and examine the scale over which a plasma can become non-neutral due to thermal fluctuations. Suppose r_{max} is the maximum radius of a sphere which is completely depleted of electrons due to thermal motions. The electrons that leave the sphere have to stop on the surface of the presumed sphere, because if the electrons continue to move outward or inward on the surface, the radius of the maximum sphere would have to be larger or smaller than r_{max}. While the electrons move to the sphere surface, their thermal energy is converted into electric potential energy, stored in the electric field produced by the remaining ions (Bellan 2008). The number of ions left in the sphere is equal to the number of electrons collected on the sphere surface. Therefore, the total ion charge in a sphere with radius r is

$$Q_{tot} = \frac{4\pi r^3 e n_e}{3}, \tag{2.20}$$

with n_e the average number density of electrons. Assuming the resulting electric field is spherically symmetric, it can be calculated using Gauss's law,

$$\frac{Q_{tot}}{\varepsilon_0} = \oint \vec{E} \cdot d\vec{A} = 4\pi r^2 E, \tag{2.21}$$

where $d\vec{A}$ is a differential surface element. Combining Eq. 2.20 and Eq. 2.21 gives the electric field at a radial distance of r from the center of the sphere,

$$E(r) = \frac{e n_e r}{3\varepsilon_0}. \tag{2.22}$$

The potential energy stored in the electric field is calculated as

$$W = \int_0^{r_{max}} \frac{\varepsilon_0 E^2(r)}{2} 4\pi r^2 dr = \frac{2\pi e^2 n_e^2 r_{max}^5}{45\varepsilon_0}. \tag{2.23}$$

The thermal energy of an electron with temperature T_e in one degree of freedom is $k_B T_e/2$. Therefore, the total thermal energy of the electrons that leave the sphere (three degrees of freedom) is

$$KE = \frac{3}{2} k_B T_e \times \frac{4}{3} \pi r_{max}^3 n_e = 2\pi k_B T_e n_e r_{max}^3. \tag{2.24}$$

Since the thermal energy is the only source of energy that is converted to the potential energy, by equating Eq. 2.23 and Eq. 2.24, r_{max} is obtained,

$$r_{max} = \left(\frac{45\varepsilon_0 k_B T_e}{e^2 n_e} \right)^{1/2}, \tag{2.25}$$

which is around seven times as large as the electron Debye length. Therefore, the maximum volume that can be vacant of electrons is on a microscopic scale. In addition, since the thermal motions of plasma particles tend to be random, the scenario that all electrons move in the radial direction, causing the maximum non-neutrality of the sphere, is very unlikely. Therefore, we can conclude that the plasma is quasi-neutral on a large macroscopic scale, i.e., $r \gg \lambda_D$ (Bellan 2008).

2.1.4 Plasma Frequency

When a plasma is disturbed by an external electric field, a cloud of electrons is driven by the electric force and travels up the potential gradient, while the ions are left in the original area due to their heavy masses. The charge separation results in an internal electric field, which has a tendency to restore the equilibrium state (electric neutrality),

$$E = \frac{enl}{\varepsilon_0}, \tag{2.26}$$

where e is the positive electron charge, n is the equilibrium ion/electron number density and l is the distance between the cloud of electrons and that of ions.

When the external perturbation is removed, the restoring force caused by Coulomb attraction accelerates the cloud of electrons towards the equilibrium position. The electrons continue to move after reaching the equilibrium position due to their inertia, and are slowed down by the resulting Coulomb repulsion. Such movements are repeated periodically, and the cloud of electrons collectively oscillates around the equilibrium position,

$$m_e \frac{d^2 l}{dt^2} = \pm eE = \pm \frac{e^2 nl}{\varepsilon_0}. \tag{2.27}$$

The frequency of such a harmonic oscillation is given by

$$\omega_{pe} = \left(\frac{e^2 n}{\varepsilon_0 m_e} \right)^{1/2}. \tag{2.28}$$

This is referred to as the (angular) electron plasma frequency, which only depends on the equilibrium number density of the electrons. Similarly, the ion plasma frequency is obtained by substituting the ion mass for the electron mass in Eq. 2.28,

$$\omega_{pi} = \left(\frac{e^2 n}{\varepsilon_0 m_i} \right)^{1/2}. \tag{2.29}$$

The ratio of the electron plasma frequency to ion plasma frequency is

$$\frac{\omega_{pe}}{\omega_{pi}} = \left(\frac{m_i}{m_e} \right)^{1/2}, \tag{2.30}$$

which is much greater than 1. Therefore, the electron plasma frequency determines the shortest time scale in response to external disturbance, and is usually called the plasma frequency.

The oscillations of electrons around ions are damped by the collisions between electrons and neutrals. If the electron plasma frequency is smaller than the collision frequency between electrons and neutrals, electrons will couple with the neutral particles, and the medium will no longer exhibit features of a plasma and instead behave like a neutral gas. In hot regions of the ISM and sufficiently ionized regions of a PPD, the number density of neutral particles is small, and the average time between electron-neutral collision is larger than the period of the oscillation. Therefore, the damping is negligible, and the medium behaves like a plasma (Bittencourt 1980).

2.1.5 Charging Currents

A dust particle immersed in plasma gains charge by collecting electrons and ions on its surface. As electrons are more mobile than ions, due to their small mass, they hit the dust particle more frequently than ions. The higher flux of electrons to the dust surface compared to that of ions causes a dust particle to be negatively charged. In addition to charging by collecting electrons and ions from the surrounding environment (primary current), dust particles can also be charged by emission of electrons, due to electron impact, ultraviolet radiation, field emission or thermionic emission (Goree 1994). Secondary electron emission happens when high energy electrons knock additional electrons on dust particles. The efficiency of electron emission depends on the impact energy, material property and dust particle size. Small particles are more efficient in emitting electrons than bulk materials, because it is easier for electrons to escape from the interior of small particles than from a large slab of material (Chow et al. 1993). Another kind of electron emission is photoelectric emission, in which a particle releases photoelectrons by absorbing ultraviolet radiation. The efficiency of this process depends on the material property (photoemission effi-

ciency) and the surface potential, as a particle with positive potential can recapture a portion of the photoelectrons (Goree 1994). The emission of electrons from the dust surface results in a positive current toward the surface (Samarian et al. 2001). When the positive current is significant compared to the negative primary current, the particle can be positively charged, or have a charge which fluctuates between positive and negative (Goree 1994). Therefore, the primary currents set a lower limit for the charge on a dust particle (Spitzer 1941).

2.1.6 Charging of Single Isolated Spherical Grain

For a spherical grain, the electron and ion currents to the grain surface are typically calculated using orbital-motion-limited (OML) theory (Allen 1992). OML theory is valid when the Debye length λ_D, a scale over which the local electric field in a plasma is screened by the surrounding charge carriers, is much greater than the radius of a dust particle, and much smaller than the collisional mean free path between neutral atoms and electrons or ions. It is assumed that a particle is charged by collecting electrons and ions when their collisionless orbits intersect with the particle's surface (Goree 1994). For a spherical dust particle with charge Q_d and physical radius R placed at the origin, and an electron/ion with charge q, mass m, and velocity v_∞ at infinity, let v_r be the electron/ion velocity at grazing collision with the dust particle. Assuming the potential energy of the electron at infinity is zero, the conservation of energy and angular momentum yields:

$$\frac{1}{2}mv_\infty^2 = \frac{1}{2}mv_r^2 + \frac{qQ_d}{R}, \tag{2.31}$$

$$mv_\infty R_{col} = mv_r R. \tag{2.32}$$

By eliminating v_r in the two equations, the collection radius R_{col} can be defined as

$$R_{col} = R\left(1 - \frac{2qQ_d}{Rmv_\infty^2}\right)^{1/2}, \tag{2.33}$$

which is the threshold impact parameter, i.e., electrons with impact parameter less than R_{col} will hit the dust particle and be collected. The capture cross section for electrons/ions by the dust particle is therefore

$$\pi R_{col}^2 = \pi R^2 \left(1 - \frac{2qQ_d}{Rmv_\infty^2}\right) \tag{2.34}$$

$$= \pi R^2 \left(1 - \frac{qV_r}{E_0}\right), \tag{2.35}$$

where $V_r = Q_d/R$ is the potential at the dust surface, and $E_0 = \frac{1}{2}mv_\infty^2$ is the kinetic energy of the electron/ion at infinity. The capture cross section is greater than the physical cross section πR^2 if the incoming plasma species and the dust particle are oppositely charged, i.e., $qV_r < 0$, and is smaller if they are like charged. The capture cross section is 0 for $qV_r > E_0$, meaning that the plasma species can not overcome the electrostatic repulsion and reach the dust surface.

For monoenergetic electrons/ions, the current towards the dust particle is

$$I = q\pi R_{col}^2 v_\infty n_\infty \tag{2.36}$$

$$= qv_\infty n_\infty \pi R^2 \left(1 - \frac{qV_r}{E_0}\right), \tag{2.37}$$

where n_∞ is the number density of electrons/ions at infinity.

For non-monoenergetic electrons/ions, i.e., the species have a velocity distribution, integration over the species' velocities is required to obtain the current towards a dust particle. The flux of plasma species β to a given surface patch P depends on the number density n_β and the velocity distribution $f(v_\beta)$ of the plasma particles (Allen 1992),

$$\Gamma_{\beta,P} = n_\beta \int\int\int f(v_\beta) v_\beta cos\theta d^3\overrightarrow{v_\beta}, \tag{2.38}$$

where θ is the angle between the velocity $\overrightarrow{v_\beta}$ and the normal of the patch surface $\hat{n}$, and $v_\beta cos\theta = \overrightarrow{v_\beta} \cdot \hat{n}$ is the velocity component of the incoming plasma particle perpendicular to the surface. The product of the flux and the particle charge q_β gives

the current density,

$$J_{\beta,P} = \Gamma_{\beta,P} q_\beta = n_\beta q_\beta \int\int\int f(v_\beta) v_\beta cos(\theta) d^3\overrightarrow{v_\beta}. \tag{2.39}$$

Using $d^3\overrightarrow{v_\beta} = v_\beta^2 dv sin\theta d\theta d\phi$, Eq.2.39 can be rewritten as

$$J_{\beta,P} = n_\beta q_\beta \int\int\int f(v_\beta) v_\beta cos\theta v_\beta^2 dv_\beta sin\theta d\theta d\phi \tag{2.40}$$

$$= n_\beta q_\beta \int f(v_\beta) v_\beta^3 dv_\beta \int cos\theta sin\theta d\theta \int d\phi. \tag{2.41}$$

Assuming a Maxwellian distribution for the ion and electron velocities,

$$f(v_\beta) = \left(\frac{m_\beta}{2\pi k_B T_\beta}\right)^{3/2} e^{\frac{-m_\beta \left|v_\beta\right|^2}{2kT}}, \tag{2.42}$$

Eq. 2.41 becomes

$$J_{\beta,P} = n_\beta q_\beta \int_{v_{min}}^{\infty} \left(\frac{m_\beta}{2\pi k_B T_\beta}\right)^{3/2} e^{\frac{-m_\beta \left|v_\beta\right|^2}{2kT}} v_\beta^3 dv_\beta \int_0^{\pi/2} cos\theta sin\theta d\theta \int_0^{2\pi} d\phi. \tag{2.43}$$

By setting v_r in Eq. 2.32 to 0, one obtains the the minimum velocity a plasma particle must have to overcome the electrostatic repulsion and reach the dust particle surface, $v_{min} = \sqrt{2q_\beta \Phi_P / m_\beta}$ for $q_\beta \Phi_P > 0$, with Φ_P the dust surface potential and m_β the mass of the plasma particle. v_{min} is zero if the dust particle carries no charge or is of opposite charge to the plasma species, i.e., $q_\beta \Phi_P \leqslant 0$. The upper limit of the integration of θ is $\pi/2$ instead of π, because only plasma particles with velocities directed towards the patch surface, i.e., $\overrightarrow{v_\beta} \cdot \hat{n} > 0$ and thus $cos\theta > 0$, can be collected by the dust particles. Integration of Eq. 2.43 over v_β, θ and ϕ yields

$$J_{\beta,P} = \begin{cases} n_\beta q_\beta \left(\frac{k_B T_\beta}{2\pi m_\beta}\right)^{1/2} exp\left(-\frac{q_\beta \Phi_P}{k_B T_\beta}\right) & \text{for} \quad q_\beta \Phi_P > 0 \\ n_\beta q_\beta \left(\frac{k_B T_\beta}{2\pi m_\beta}\right)^{1/2} \left(1 - \frac{q_\beta \Phi_P}{k_B T_\beta}\right) & \text{for} \quad q_\beta \Phi_P \leqslant 0 \end{cases} \tag{2.44}$$

The current of plasma species β to a sphere with radius R is given by

$$I_\beta = 4\pi R^2 J_{\beta,P}. \tag{2.45}$$

By defining $I_{0,\beta} = 4\pi R^2 n_\beta q_\beta \sqrt{\frac{k_B T_\beta}{2\pi m_\beta}}$, which is the current collected when $\Phi_P = 0$, Eq. 2.45 becomes

$$I_\beta = \begin{cases} I_{0,\beta}\ exp\left(-\frac{q_\beta \Phi_P}{k_B T_\beta}\right) & \text{for} \quad q_\beta \Phi_P > 0 \\ I_{0,\beta}\left(1 - \frac{q_\beta \Phi_P}{k_B T_\beta}\right) & \text{for} \quad q_\beta \Phi_P \leqslant 0 \end{cases} \tag{2.46}$$

For electrons with charge $-e$, mass m_e, number density n_e and temperature T_e, the current is given by

$$I_e = \begin{cases} I_{0,e}\left(1 + \frac{e\Phi_P}{k_B T_e}\right) & \text{for} \quad \Phi_P > 0 \\ I_{0,e}\ exp\left(\frac{e\Phi_P}{k_B T_e}\right) & \text{for} \quad \Phi_P \leqslant 0 \end{cases} \tag{2.47}$$

where $I_{0,e} = -4\pi R^2 n_e e \sqrt{\frac{k_B T_e}{2\pi m_e}}$. Similarly, for ions with charge Ze, mass m_i, number density n_i and temperature T_i, the current is

$$I_i = \begin{cases} I_{0,i}\ exp\left(\frac{-Ze\Phi_P}{k_B T_i}\right) & \text{for} \quad \Phi_P > 0 \\ I_{0,i}\left(1 - \frac{Ze\Phi_P}{k_B T_i}\right) & \text{for} \quad \Phi_P \leqslant 0 \end{cases} \tag{2.48}$$

with $I_{0,i} = 4\pi R^2 n_i Z e \sqrt{\frac{k_B T_i}{2\pi m_i}}$.

The balance between the negative current (electrons) and positive current (ions) towards a dust particle determines its charge and surface potential. Assuming the charge varies smoothly, i.e., ignoring the discrete nature of the charge (Goree 1994), the change in charge of the dust particle per second equals the sum of all currents to the particle. In the case of a single ion species,

$$\frac{dQ_d}{dt} = I_i + I_e. \tag{2.49}$$

The equilibrium state is reached when the total charge gained by the particle per second is zero, $dQ_d/dt = 0$ (Spitzer 1941), meaning

$$I_i + I_e = 0. \tag{2.50}$$

Substituting Eqs 2.48 and 2.47 into Eq. 2.50 yields

$$-n_e\sqrt{\frac{T_e}{m_e}}\ exp\left(\frac{e\Phi_P}{k_BT_e}\right) = n_iZ\sqrt{\frac{T_i}{m_i}}\left(1-\frac{Ze\Phi_P}{k_BT_i}\right). \tag{2.51}$$

The equilibrium potential depends on the temperatures and masses of ions as well as electrons. For $n_i = n_e$, $T_i = T_e$ and $Z = 1$, Eq. 2.51 becomes

$$-\sqrt{\frac{m_i}{m_e}}\ exp\left(\frac{e\Phi_P}{k_BT_e}\right) = \left(1-\frac{Ze\Phi_P}{k_BT_i}\right). \tag{2.52}$$

The numerical solution to Eq. 2.52 is the classical Spitzer potential,

$$\Phi_P = -2.5\ k_BT_e/e. \tag{2.53}$$

The equilibrium charge of a spherical dust particle is proportional to the particle's surface potential,

$$Q_d = C\Phi_P, \tag{2.54}$$

where $C = 4\pi\varepsilon_0\,(R + R^2/\lambda_D)$ is the capacitance of the dust particle, which equals $C = 4\pi\varepsilon_0 R$ when the particle radius is much less than the Debye length. The charging time depends on the particle size and plasma density: the larger the dust particle and the higher the plasma density, the faster it charges up (Goree 1994).

2.1.7 Charging of Irregular Aggregates (OML_LOS)

The OML method assumes spherical grains, and all ions/electrons with impact factors smaller than R_{col} can be collected by the dust grain. However, dust aggregates in space are irregularly shaped, and the non-spherical distribution of potential near the dust particle can reflect ions/electrons (Goree 1994) or block the trajectories of incident electrons or ions (Matthews et al. 2012). The irregular aggregate surface is treated by modifying the OML currents using a line-of-sight approximation (OML_LOS) to adjust the currents to less-exposed regions of the surface (Matthews et al. 2012; Matthews et al. 2016). The surface of each sphere is divided into patches,

and the charging current due to incoming plasma species is calculated for each patch by determining open Lines of Sight (LOS), i.e., paths for incoming electrons or ions to the patch.

The current density to a given patch can be split into two parts: the component of the current density $J_{\beta 0}(v_\beta)$, which only depends on the speed of the plasma particles, and the line of sight factor L_p for the patch P, which depends on the angle of the incoming trajectories with respect to the surface normal. Using $d^3\overrightarrow{v_\beta} = v_\beta^2 dv d\Omega$, where $d\Omega$ is the differential solid angle, Eq. 2.39 can be rewritten as

$$J_{\beta,P} = n_\beta q_\beta \int f(v_\beta) v_\beta^3 dv_\beta \times \int\int cos(\theta) d\Omega \tag{2.55}$$

$$= J_{\beta 0} L_p, \tag{2.56}$$

where

$$J_{\beta,0} = n_\beta q_\beta \int f(v_\beta) v_\beta^3 dv_\beta = \begin{cases} \frac{n_\beta q_\beta}{\pi} \left(\frac{k_B T_\beta}{2\pi m_\beta}\right)^{1/2} exp\left(-\frac{q_\beta \Phi_P}{k_B T_\beta}\right) & \text{for} \quad q_\beta \Phi_P > 0 \\ \frac{n_\beta q_\beta}{\pi} \left(\frac{k_B T_\beta}{2\pi m_\beta}\right)^{1/2} \left(1 - \frac{q_\beta \Phi_P}{k_B T_\beta}\right) & \text{for} \quad q_\beta \Phi_P \leqslant 0 \end{cases} \tag{2.57}$$

$$L_p = \int\int cos\left(\theta\right) d\Omega, \tag{2.58}$$

assuming a Maxwellian velocity distribution of ions and electrons. L_p can not be integrated directly, as it depends on whether the line of sight in a given direction is obstructed by other monomers. As shown in Figure 2.1, the shaded areas indicate the open solid angles for four given points on a monomer surface, i.e., plasma particles approaching the sphere with trajectories in those regions can reach the surface points, with the assumption of straight-line trajectories. In order to calculate L_p, the surface of an aggregate is divided into patches with approximately equal surface area. In the simulation, the number of patches on a monomer with radius R (in unit of μm) is

$$N = 10 R_{int}^2, \tag{2.59}$$

where R_{int} is the nearest integer of R.

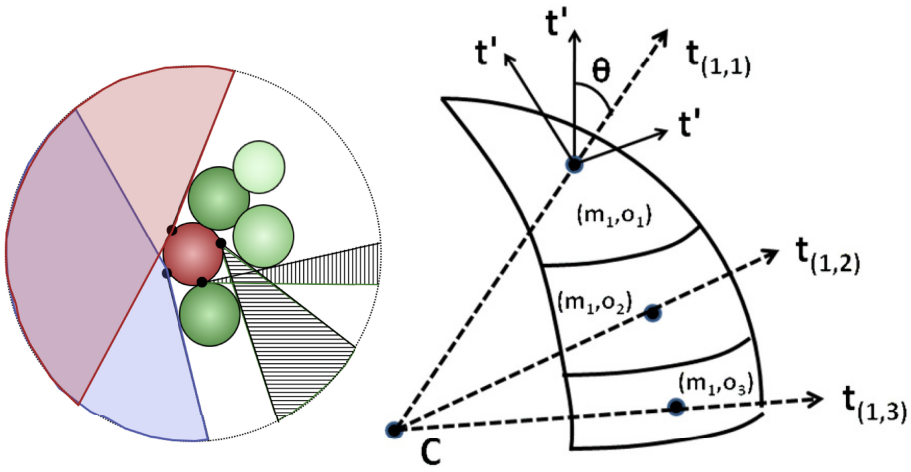

Figure 2.1: Two-dimensional representation of OML_LOS geometry. Plasma currents to the surface points on monomers are partly blocked by other monomers. In the left figure, the shaded areas indicate the open solid angles for four given points on a monomer surface. Shown in the right figure are three surface patches with coordinates (m_1, o_1), (m_1, o_2), (m_1, o_3) on the monomer centered at point C. The vectors $\mathbf{t}_{1,1}$, $\mathbf{t}_{1,2}$, $\mathbf{t}_{1,3}$ are the normal vectors to the patches, and the vectors $\mathbf{t}'$ indicate some test directions for patch (m_1, o_1) to determine its open lines of sight. Figure credit: Matthews et al. 2012.

For each patch, a certain number of test directions, which originate at the center of the patch, are defined (Figure 2.1), and are tested to determine whether the line of sight is open or blocked by another monomers. As shown in Figure 2.2, $\vec{t'}$ is a test direction originating at the center of patch P on monomer i, and $\vec{d}_{ij}$ is a vector pointing from the center of patch P to monomer j with magnitude equal to the distance between them. The line of sight to patch P in this direction is blocked by monomer j if the perpendicular distance between the center of monomer j and the test direction $\vec{t'}$ is smaller than the radius R_j of monomer j, and the angle between $\vec{t'}$ and $\vec{d}_{ij}$ is smaller than 90°,

$$\left|\vec{d}_{ij}\right|^2 - \left|\vec{d}_{ij} \cdot \hat{t'}\right|^2 < R_j^2 \tag{2.60}$$

$$\vec{d}_{ij} \cdot \vec{t'} > 0, \tag{2.61}$$

where $\hat{t'}$ is a unit vector in the $\vec{t'}$ direction.

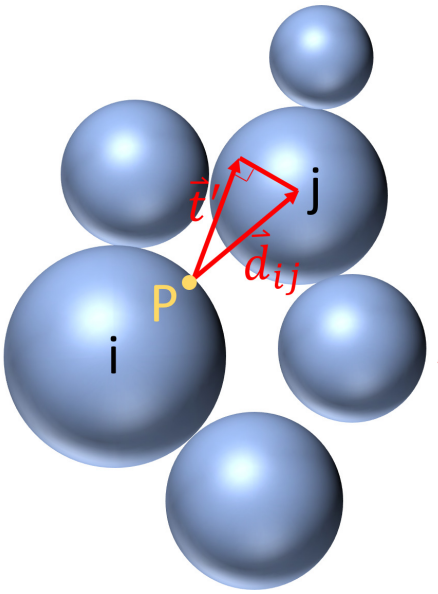

Figure 2.2: Geometry to determine the open lines of sight. $\vec{t}'$ is a test direction at the center of patch P on monomer i, and $\vec{d}_{ij}$ is a vector pointing from the center of patch P to monomer j.

This test is conducted for all monomers within the aggregate, including the monomer on which the patch resides. If any of the monomers blocks the line of sight to patch P in test direction $\vec{t}$, LOS is assigned with a value 0, $LOS_{P,t} = 0$. Otherwise, $LOS_{P,t} = 1$. The integral over the solid angle in Eq. 2.58 is then approximated by a sum over test directions originating from the center of patch P which cover the solid angle $\Delta\Omega_t$,

$$L_p \approx \sum_t LOS_{t,P} \times cos\theta_t \Delta\Omega_t, \tag{2.62}$$

where θ_t is the angle between the normal direction of the patch and the test direction $\vec{t}$. Monomers in the interior of the aggregate are more likely to have blocked lines of sight, i.e., small L_p, and thus collect little charge.

The net current of species β to patch P is obtained by multiplying the current density $J_{\beta,P}$ by the patch's surface area Δs,

$$I_{\beta,P} = J_{\beta,P} \times \Delta s, \tag{2.63}$$

where $\Delta s = R^2 \Delta\Omega_P$, with R the radius of the monomer on which the patch resides and $\Delta\Omega_P$ the solid angle covered by the patch. Summing over all species gives the total current to patch P,

$$I_P = \sum_\beta I_{\beta,P}. \tag{2.64}$$

The change in the charge on the patch during a time interval dt is then calculated by

$$dQ_P = I_P dt. \tag{2.65}$$

The charge on a monomer is obtained by summing over the contribution from each patch, and the total charge of an aggregate is obtained by adding up the contributions from all constituent monomers. Note that the current reaching patch P depends on the minimum velocity of plasma particles to overcome the Coulomb repulsion barrier, which depends on the potential of the patch due to the charges of all other patches,

$$V_P = \sum_l \frac{Q_l}{4\pi\epsilon_0 d_l}, \tag{2.66}$$

where l sums over all patches in the aggregate. Q_l and d_l are the charge of the l_{th} patch and its distance from patch P, respectively. Therefore, the change in charge on a given patch depends on the charges on other patches, and the charge on each patch is calculated in an iterative process until the equilibrium charge is reached, i.e., the change in aggregate charge is smaller than 0.01% of the aggregate charge at the previous time step (Matthews et al. 2012, 2016).

At large distances, the electrostatic force acting on a dust aggregate due to another aggregate is calculated using a multipole approximation including terms up to the quadrupole moment. The monopole moment q is the sum of charges contributed from all patches on an aggregate,

$$q = \sum_l q_l, \tag{2.67}$$

where l is the index of each patch. The dipole moment $\vec{p}$ is given by

$$\vec{p} = \sum_l q_l \vec{d}_l, \tag{2.68}$$

where $\vec{d}_l$ is the vector pointing from the center of mass (COM) of the aggregate to patch l. The elements of the quadrupole moment, $\bar{\bar{M}}$, are calculated from

$$M_{ij} = \sum_l 3 r_{l,i} r_{l,j} q_l - \delta_{ij} \sum_l r_l q_l, \tag{2.69}$$

where r_l is the distance of patch l from the origin, and the indices i, j run over the Cartesian coordinates x, y, z.

The electrostatic potential at a position $\vec{r}$ from the COM of an aggregate is approximated using the monopole, dipole and quadrupole moments (Matthews et al. 2015),

$$\begin{aligned} V &= \frac{1}{4\pi\epsilon_0}\left(\frac{q}{r} + \frac{\vec{p}\cdot\vec{r}}{r^3} + \frac{\vec{r}^T\bar{\bar{M}}\vec{r}}{2r^5}\right) \\ &= \frac{1}{4\pi\epsilon_0}\left(\frac{q}{r} + \frac{1}{r^3}\sum_i p_i r_i + \frac{1}{2r^5}\sum_{i,j} M_{ij} r_i r_j\right), \end{aligned} \tag{2.70}$$

where $\vec{r}^T$ is the transpose of $\vec{r}$. The electric field at $\vec{r}$ from the aggregate's COM is calculated by taking the negative gradient of the potential,

$$\begin{aligned} \vec{E}(\vec{r}) &= \vec{E}_{mon} + \vec{E}_{dip} + \vec{E}_{quad} \\ &= \frac{1}{4\pi\epsilon_0}\left\{\frac{q\hat{r}}{r^2} + \frac{3\hat{r}(\vec{p}\cdot\hat{r}) - \vec{p}}{r^3} + \frac{1}{r}\left[\frac{5}{2r^2}\left(\vec{r}^T\bar{\bar{M}}\vec{r}\right)\vec{r} - \bar{\bar{M}}\vec{r}\right]\right\}. \end{aligned} \tag{2.71}$$

The i_{th} component of the electric field is given by

$$\begin{aligned} E_i(\vec{r}) = \frac{1}{4\pi\epsilon_0}\Bigg\{ &\frac{q r_i}{r^3} + \frac{1}{r^5}\left(3 r_i \sum_i p_i r_i - p_i r^2\right) + \\ &\frac{1}{r}\left[\frac{5}{2r^2}\left(\sum_{i,j} M_{ij} r_i r_j\right)\vec{r} - \sum_j M_{ij} r_j\right] \end{aligned} \tag{2.72}$$

The force on an aggregate with charge q and dipole moment $\hat{p}$ in a non-homogeneous electric field produced by another aggregate is given by (Weisstein

2012)

$$\vec{F} = q\vec{E} + \bar{\bar{G}}\vec{p}, \tag{2.73}$$

with the i_{th} component equal to

$$F_i = qE_i + \sum_j G_{ij} p_j, \tag{2.74}$$

where $G_{ij} = \nabla_i E_j$, is the gradient of the electric field. For a multipole approximation up to the quadrupole term, G_{ij} is given by (Raab & de Lange, 2004),

$$G_{ij} = \frac{-1}{8\pi\epsilon_0 r^7}\left[30 r_i r_j \vec{p}\cdot\hat{r} + 35 r_i r_j \vec{r}^T \bar{\bar{M}} \vec{r} - 10 r_i \sum_k M_{jk} r_k - 10 r_j \sum_k M_{ik} r_k \right.$$
$$\left. + r^2\left(2M_{ij} - 6p_i r_j - 6p_j r_i + 6q r_i r_j\right) + \delta_{ij}\left(5\vec{r}^T \bar{\bar{M}} \vec{r} + 6r^2 \vec{p}\cdot\hat{r} + 2qr^4\right)\right]. \tag{2.75}$$

The total torque on an aggregate in the electric field of a second aggregate, which causes its rotation, is the sum of the torque from the dipole moment and that from the quadrupole moment,

$$N_i = N_i^{dip} + N_i^{quad}. \tag{2.76}$$

The contribution to the torque on a dust aggregate from dipole moment $\hat{p}$ in the electric field $\hat{E}$ produced by a second aggregate is

$$N_i^{dip} = \sum_{j,k} \varepsilon_{ijk} p_j E_k, \tag{2.77}$$

where ε_{ijk} is the Levi-Civita pseudo-tensor. The torque from the quadrupole moment is given by (Torres del Castillo & Mendez Garrido 2006)

$$N_i^{quad} = \frac{1}{3}\sum_{jkv} \varepsilon_{ijk} Q_{jv} G_{kv}. \tag{2.78}$$

At close approach (a few aggregate radii), the charge approximation using the dipole and quadrupole moments breaks down, and the electrostatic force acting on aggregate 1 due to aggregate 2 is calculated by treating the monomers as point charges centered at each monomer. Thus the force on the m_{th} monomer in aggregate 1 is

(Matthews et al. 2015, 2016)

$$\vec{F}_m = \sum_n \frac{q_m q_n \hat{d}_{mn}}{4\pi\epsilon_0 d_{mn}^2}, \tag{2.79}$$

where n runs over all monomers in aggregate 2 and d_{mn} is the distance between two monomers. The total force on aggregate 1 is then obtained by (Matthews et al. 2015)

$$\vec{F} = \sum_m \vec{F}_m, \tag{2.80}$$

where m runs over all monomers in aggregate 1. The net torque on aggregate 1 is given by

$$\vec{N} = \sum_m \vec{r}_m \times \vec{F}_m, \tag{2.81}$$

where $\vec{r}_m$ is the position vector pointing from the origin of the coordinate system to the center of the m_{th} monomer. The force and torque on aggregate 2 can be obtained in the same way by switching the two aggregates in the equations above.

2.1.8 Charging of Chondrule Dust Rim

A rimmed chondrule is modeled as an aggregate of spheres. The charge on the rimmed chondrule includes two parts: the charge on the spherical chondrule core and the charge on the porous dust rim. As most dust rims in CM chondrites appear to be evenly layered around the entire chondrule in petrographic observations, we assume that the chondrule accretes dust isotropically, and restrict our study to a small patch on the chondrule surface for computational expediency. As the monomers on the vertical sides of the pile have a greater LOS_factor than if the entire dust rim were included in the simulation, we divide the dust pile into two regions, an inner region (the yellow spheres in Figure 2.3a) and an outer region (the green spheres in Figure 2.3a), and only use OML_LOS to charge the monomers in the inner region. The outer monomers are included in the calculation of the LOS_factor for the inner monomers (Figure 2.3b). After the charges on the monomers in the inner region are obtained,

they are used to approximate the charges on the outer monomers: the monomers in the two regions are sorted based on their distance z from the top of the dust pile, and the charges on the inner monomers are assigned to the outer monomers with the same ranking, scaled by the ratio of the radius of the outer monomer to that of the inner monomer (Figure 2.3c),

$$Q_{out}(z) = Q_{in}(z) \times \frac{r_{out}}{r_{in}}, \tag{2.82}$$

where Q and r are the charge and monomer radius, with the subscripts "out" and "in" representing outer and inner monomers, respectively. In this manner, the charge on the monomer is related to its radius and distance from the chondrule surface.

After the charges on the monomers are obtained, the total charge of the dust pile and the chondrule patch beneath the pile are duplicated as point charges on the rest of the chondrule surface, based on the ratio of the chondrule patch area to the total chondrule surface area. The duplicated charges have the same distance from the chondrule core as the center of charge of the dust pile. As shown in Fig. 2.3d, the deviation from spherical equipotential lines is very small except very near the dust rim surface. The charge on the entire chondrule is then obtained by adding the duplicated charges to the total charge of the dust pile and the chondrule patch beneath the pile. The dipole and quadrupole moments are calculated using formulas 2.68 and 2.69 by treating each duplicated charge as a patch. A multipole expansion up to the quadrupole term is used to determine the force and torque (Eqs. 2.74, 2.76) on an incoming dust particles at large distance. At close approach, the force and torque are calculated by Eqs. 2.80 and 2.81, in which m runs over all monomers in the dust pile, the chondrule patch beneath the pile and all duplicated point charges. The force and torque on the dust particle eventually determine its trajectory and rotation (for an aggregate) while approaching the chondrule surface.

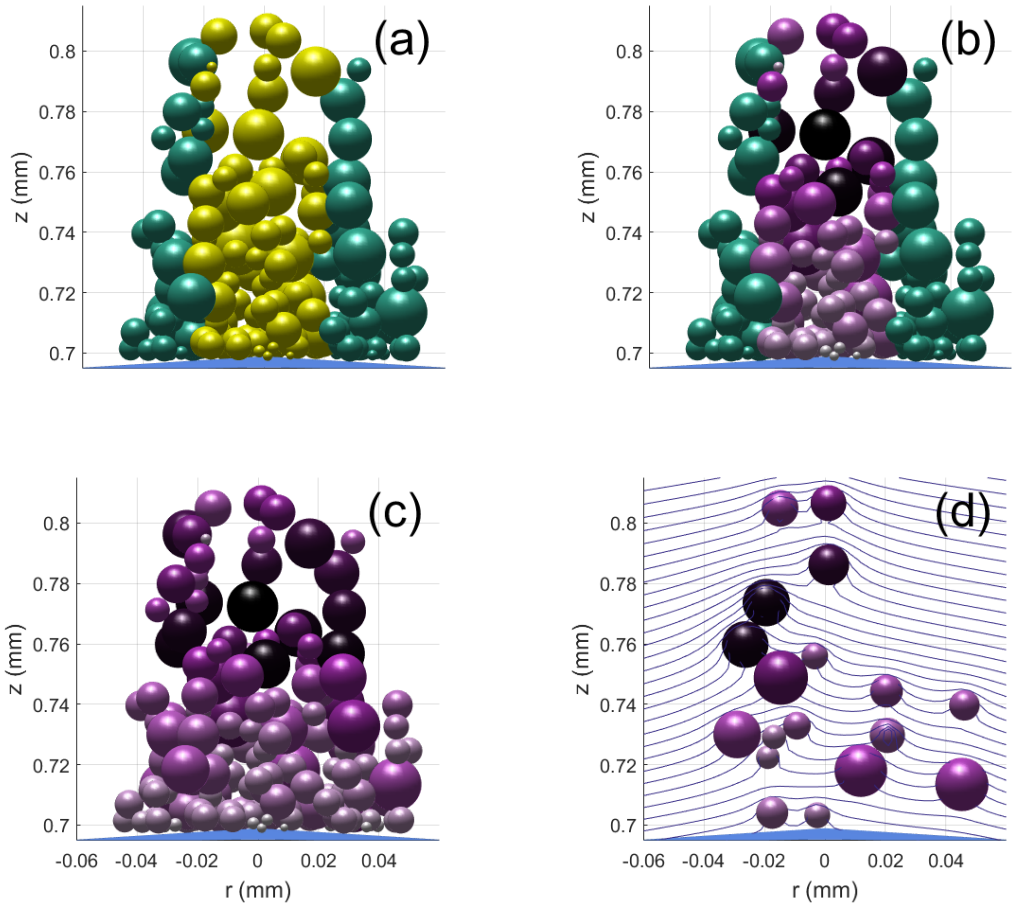

Figure 2.3: Illustration showing two different regions used in the charging calculation and the resulting equipotential lines. a) depicts the initial state before the monomers are charged, with the two colors indicating the inner (yellow) and outer (green) regions. b) represents the state after the monomers in the inner region have been charged. The charge collected by the inner spheres is calculated directly using OML_LOS, and the outer spheres are used to calculate the LOS_factor for the inner spheres. The resulting charge collected by each sphere in the inner region is indicated by the shade: large spheres near the top of the pile collect the most charge (dark), while small, interior spheres collect little charge (light). c) represents the state after all monomers have been charged. The charges on the inner monomers are used to approximate the charge on the spheres in the outer region, based on their size and distance from the chondrule surface. d) shows equipotential lines for a slice through the center of the dust pile.

2.1.9 Charging when $n_e \neq n_i$

Local quasi-neutrality of the plasma leads to a zero net charge contributed by the free electrons, free ions and dust particles. Assuming a single ion species, the

quasi-neutrality condition is

$$-en_e + en_i - eZ_D n_D = 0, \tag{2.83}$$

where n_e, n_i and n_D are the number densities of free electrons, free ions and dust particles, respectively, and Z_D is the dust charge number.

In a plasma with high dust concentrations, the density of free electron is reduced due to electron collection on the dust particles, which affects the dust particle's floating potential as well as the plasma potential. This effect is characterized by the Havnes parameter P, which is the ratio of the charge density on the dust particles to the density of free electrons (Havnes et al. 1990),

$$P = \frac{n_D z_D}{n_e}. \tag{2.84}$$

For spherical dust particles with a radius R,

$$P = 695TR\frac{n_D}{n_e}, \tag{2.85}$$

where the temperature T is measured in eV and the dust radius R is given in μm. n_D and n_e are the number of dust particles and electrons per cm^3. The dust particle's floating potential is greatly reduced for $P > 1$, and is barely affected for $P \ll 1$. In this simulation, three cases are considered: $n_e/n_i = 0.1$, 0.5 and 1, corresponding to P value of 9, 1 and 0, respectively.

2.2 Relative Dust Motion in a Turbulent Protoplanetary Disk

Various mechanisms impart relative velocities to solid particles in a protoplanetary disk (PPD), such as Brownian motion, inward radial drift, vertical settling towards the midplane, and turbulence (Brauer et al. 2008; Weidenschilling 1977; Voelk et al. 1980; Ormel & Cuzzi 2007; Ormel et al. 2008). The dominant source of relative velocities depends on the disk temperature and location, as well as on the particle properties, i.e., mass and porosity (Krijt et al. 2015). The collision energy

determines the collision outcome: two dust particles can stick at the point of contact, cause restructuring to the resulting particle, bounce, fragment, etc. At the same time, the relative velocity between dust particles of various sizes affects the collision rate, which determines the growth rate of the dust population.

For the disk locations and particle sizes considered in this dissertation, turbulence is the dominant source for the relative velocity between dust particles, as systematic relative velocities due to drift and settling are much lower for particles sizes relevant to our problem (Rice et al. 2004; Dullenmond et al. 2004; Ormel et al. 2008). Therefore, we only consider the contributions of turbulence and Brownian motion in this study, assuming the particles are well coupled to turbulent eddies.

In the rest of this section we discuss the turbulent relative velocity and the possible collision outcomes that we consider in our simulations.

2.2.1 Turbulent Relative Velocity

As discussed above, in our models, the relative velocity between two dust particles is the sum of the turbulent velocity v_T and Brownian velocity v_B,

$$v_r = \sqrt{v_B^2 + v_T^2}, \tag{2.86}$$

where the contribution from Brownian motion is much smaller than that from turbulence. The Brownian velocity depends on the masses of the two colliding particles, m_1 and m_2,

$$v_B = \sqrt{\frac{8(m_1 + m_2)k_B T}{\pi m_1 m_2}}, \tag{2.87}$$

where k_B is Boltzmann's constant and the gas temperature is given by $T = 280\ K/\sqrt{r}$, based on the minimum mass solar nebula (MMSN) model (Weidenschilling 1977; Hayashi 1981; Thommes et al. 2006), with r the heliocentric distance (taken to be 1 AU in this study).

A closed-form analytical expression for the relative turbulent velocity v_T between two grains was presented by Ormel & Cuzzi (2007) and Ormel et al. (2008), by comparing the stopping time of the largest particle,

$$\tau_1 = \frac{3}{4 c_g \rho_g} \frac{m_1}{\pi a_1^2}, \tag{2.88}$$

where ρ_g is the gas density, c_g is the gas thermal speed, and m_1 and a_1 are the mass and equivalent radius of the particle, to the turn-over times of the largest and smallest turbulent eddies, t_L and t_s. Three regimes are considered: the linear regime for small particles; the square_root regime; and the "high stokes regime" where particles decouple from the gas (Ormel et al. 2008),

$$v_T = \begin{cases} v_g Re^{1/4}(\mathrm{St}_1 - \mathrm{St}_2) & \text{for} \quad \tau_1 < t_s \\ v_g[2y_a - (1+\epsilon) + \frac{2}{1+\epsilon}(\frac{1}{1+y_a} + \frac{\epsilon^3}{y_a+\epsilon})]^{1/2} \mathrm{St}_1^{1/2} & \text{for} \quad 5t_s \simeq \tau_1 \lesssim t_L \\ \left(\frac{1}{1+\mathrm{St}_1} + \frac{1}{1+\mathrm{St}_2}\right) & \text{for} \quad \tau_1 \geq t_L \end{cases} \tag{2.89}$$

In this expression, v_g is the gas speed; Re is the Reynolds number, defined as the ratio of the turbulent viscosity, $\nu_T = \alpha c_g^2/\Omega$, to the molecular viscosity of gas, $\nu_m = c_g\lambda/2$ (Cuzzi et al. 1993), with α the turbulence strength (Shakura & Sunyaev 1973), Ω the local Keplerian angular speed, and λ the gas mean free path; the turn-over times of the largest and smallest eddies are $t_L = 1/\Omega$ and $t_s = Re^{-1/2} t_L$, respectively; the Stokes numbers St_i, $i = 1, 2$, are the ratios τ_i/t_L; y_a is a numerical constant taken to be 1.6; and the quantity ϵ is the ratio $\frac{St_1}{St_2} \leq 1$ (Ormel et al. 2008).

For the regions of the PPD that we are considering and the particle sizes (based on MRN distribution described in Section 1.3.7) used in our simulation, v_T is determined by the first condition in Eq. 2.89, and the relative velocities depend on the size difference between the colliding grains

$$v_T = (\frac{v_g Re^{1/4} \Omega}{c_g \rho_g})(SAD_1 + SAD_2), \quad \tau_1 < t_s \tag{2.90}$$

where $SAD_i = 3m_i/4a_i^2$, i=1,2, is the spherically averaged density of aggregates.

2.2.2 Collision Outcomes

For low-velocity collisions between particles, i.e., $v < 10\ cm\ s^{-1}$, almost all collisions result in sticking (Ormel et al. 2008). However, collisions with energies that exceed a certain minimum threshold will result in restructuring, bouncing, fragmentation, erosion, mass transfer, cratering and abrasion. The threshold velocities for different collision outcomes depends on the material properties, aggregate size, constituent monomer size, mass ratio, as well as the porosity of colliding bodies. For example, the experiments conducted by Blum & Münch (1993) showed that an impact velocity of $\sim 0.15 - 1\ ms^{-1}$ between mm-sized particles results in bouncing, and a velocity $\gtrsim 1\ ms^{-1}$ results in fragmentation. Note that there can be multiple scenarios for each of these outcomes. For example, particles with collision energy lower than the hit-and-stick threshold energy stick at first contact (Dominik & Tielens, 1997; Blum & Wurm 2000). A collision energy exceeding the hit-and-stick threshold energy results in sticking with surface effects: the contact zone of the particles is elastically deformed/flattened, and the increased contact area can cause sticking at greater velocities (Blum & Münch 1993; Weidling et al. 2009). For even higher collision velocities, sticking can occur between a large porous aggregates and a small/compact projectile, which leads the projectile to penetrate deeply into the target. Experiments show that the projectile can not bounce off the target if the penetration is deeper than the projectile size (Langkowski et al. 2008; Blum & Wurm 2008).

Likewise, bouncing can cause alteration of the colliding partners, depending on their sizes, porosity and the collision energy. For two similar-sized aggregates, a bouncing collision causes compaction of the particles, through which the energy is dissipated (Weidling et al. 2009). On the other hand, for two porous particles with great size difference, the small projectile penetrates slightly into the large target, and bounces off alone with some material from the target. A local compaction is caused in this process (Langkowski et al. 2008; Blum & Wurm 2008).

Similarly, for particles with relative velocities exceeding the fragmentation velocity threshold, the collision results depend on the size ratio of the colliding particles: catastrophic fragmentation occurs with similar-sized collision partners, while erosion, mass transfer or cratering occurs for particles with great size difference. When the projectile is very small, collisions are likely to cause local erosion near the impact point on the large body. The erosion threshold velocity increases with increasing mass ratio, and the erosion efficiency increases with increasing impact velocity (Krijt et al. 2015). Mass transfer is also a possible collision outcome, in which part of the projectile's mass ($\lesssim 50\%$) is permanently transferred to the target body and is compressed to a volume filling factor of 0.3-0.4 (Blum 2018; Teiser et al. 2011; Beitz et al. 2011). For larger projectiles, the mass transferred to the target object is less than the excavated mass. As a result, the collision causes cratering on the target body. The mass loss of the target increases with increasing collision energy of the projectile, up to 35 times the projectile's mass (Blum 2018; Wurm et al. 2005a; Paraskov et al. 2007).

In our simulations, the relative velocities are low and for simplicity we only consider hit-and-stick, bouncing and restructuring. The collision outcomes are determined by whether or not the impact velocity exceeds the critical velocity for bouncing or rolling. In the rest of this section, we briefly discuss the mathematical form of these threshold velocities.

2.2.2.1. Sticking The microphysics of collisions between two smooth spherical grains was derived in detail by Chokshi et al. (1993) and Dominik & Tielens (1997) using elastic continuum theory. Upon contact, the van der Waals force accelerates the colliding particles which elastically deform near the contact region, forming a neck of material. The degrees of the reduction of surface energy and the excitation of elastic surface waves during this process determine the threshold kinetic energy between sticking and bouncing (Wurm & Blum 1998). If the kinetic energy is sufficient to

break the neck, the particles separate and dissipate energy in elastic waves. Otherwise, the particles stick together. The critical velocity, corresponding to the critical kinetic energy, depends on the sizes of the grains and the material properties, and is given by (Chokshi et al. 1993)

$$v_{cr} \simeq 3.86 \frac{\gamma^{5/6}}{E^{1/3} R^{5/6} \rho^{1/2}}, \tag{2.91}$$

with γ and ρ respectively the surface energy per unit area and the density of the grains, and R the reduced radius of the two spheres, $R = R_1 R_2/(R_1 + R_2)$. The Poisson ratios ϑ_1, ϑ_2 and Young's moduli E_1, E_2 of the two grains enter into the expression via the material constant $E = [(1 - \vartheta_1^2)/E_1 + (1 - \vartheta_2^2)/E_2]^{-1}$.

2.2.2.2. Bouncing Bouncing occurs when the collision velocity is too high for hit-and-stick collisions to occur, and yet lower than the threshold fragmentation velocity. For collisions between fluffy aggregates consisting of monodisperse monomers, assuming there is only one contact point per monomer, the local properties are the same as for two contacting monomers. The increased mass of the aggregates, compared to the case of monomer-monomer collisions, can be expressed as an increased density in Eq. 2.91, scaling the critical velocity by $N^{-1/2}$, where N is the number of monomers in the two aggregates. Letting μ and m_0 be the reduced mass of the two aggregates and the mass of a monomer respectively, the critical velocity between aggregates can be expressed as (Wurm & Blum 1998)

$$v_{cr}^{'} = \frac{1}{\sqrt{2}} v_{cr} \left(\frac{\mu}{m_0} \right), \tag{2.92}$$

where v_{cr} is the critical bouncing velocity for the monomer-monomer collision between the two contacting spheres. In our simulation with polydisperse monomers, m_0 is set to be the average mass of all the monomers in the two aggregates.

2.2.2.3. Restructuring Restructuring occurs when particles roll along the surface. For micron-sized particles considered in the astrophysical context, the main

source of friction comes from bonds between atoms at the surface. New contacts can be made and old contacts can be broken only in step sizes of at least one atom (Dominik & Tielens 1997). The critical energy required to roll a distance equal to the size of an atom is

$$e_{roll} = 6\pi\gamma\xi_{\rm crit}^2, \tag{2.93}$$

where γ is the surface energy per unit area and $\xi_{\rm crit}$ is the average distance over which energy is dissipated. Following Dominik & Tielens (1997), we set $\xi_{\rm crit} = 1\ \mathring{A}$. In order to cause non-negligible restructuring, the particle has to roll a finite distance. Therefore, we define the quantity E_{roll}, which is the energy required to roll a distance of 1000 $\mathring{A}$,

$$E_{roll} = 1000 e_{roll}. \tag{2.94}$$

Greater impact energy leads to more massive restructuring, and the maximum restructuring occurs when all monomers in the aggregate have sufficient energy to roll a angle of 90 degrees (Paszun & Dominik 2009).

This derivation assumes that the critical rolling energy is independent of the monomer size. Therefore, the energy required to roll a distance of half the sphere is proportional to the monomer radius a, $E \propto a$. However, some recent research shows that the rolling force scales with the monomer area in direct contact, resulting in a smaller energy required to roll this distance, $E \propto a^{\frac{5}{3}}$ (Krijt et al. 2015). Smaller rolling energy means that particles are more likely to restructure and form a more compact structure (Krijt et al. 2015). The implementation of the restructuring process in this simulation is described in Section 3.3.2.

Some content in this chapter was published in Xiang et al. 2017a, 2017b, 2019a, 2019b, 2019c.

CHAPTER THREE

Numerical Treatment

3.1 Aggregate Structure

As discussed above, the porosity of dust particles plays an important role in the collision process, as it impacts the coupling of dust particles to the motion of ambient gas. The relative velocity developed due to the difference of dust particles coupling times (see Section 2.2.1) affects the collision frequency (and therefore the dust growth rate), the collision outcome (see Section 2.2.2) and also determines whether two charged particles can overcome the electrostatic barrier and coagulate. Due to its importance, a consistent measurement of porosity is needed. Different quantities have been used to measure the "fluffiness" of aggregates in previous works, such as fractal dimension (Gmachowski 2002), gyration radius (Wada et al. 2008), and enlargement factor (Ormel et al. 2008). Here we adopt the compactness factor Φ_σ (Min et al. 2006). This parameter is useful in this case as it is based on an aggregate's equivalent radius R_σ, which defines an effective cross section for coupling with the gas and has been shown to be directly related to an aggregate's charge (Matthews et al. 2012). We use Φ_σ, R_σ, and an aggregate's physical radius R to characterize the structure of an aggregate, as described below. For both the dust aggregate and the rimmed chondrule, the physical radius is the maximum radial extent from the center of mass (COM).

The equivalent radius R_σ of an aggregate is defined as the radius of a circle with area equal to the projected cross-section σ of the aggregate averaged over many orientations (Min et al. 2006),

$$R_\sigma = \sqrt{\frac{\sigma}{\pi}}. \tag{3.1}$$

The compactness factor Φ_σ for an aggregate is defined as the ratio of the volume of all the constituent monomers in an aggregate to the volume of a sphere with radius equal to R_σ,

$$\Phi_\sigma = \frac{\sum_i^N r_i^3}{R_\sigma^3}, \tag{3.2}$$

where r_i is the radius of the constituent monomer and N is the total number of monomers within the aggregate (Figure 3.1a).

In the case of a rimmed chondrule, as we only simulate a dust pile on the chondrule surface, we use different methods to define its porosity and R_σ. The porosity of a horizontal layer (i.e., parallel to the chondrule's surface) in the dust rim is defined as the ratio of the volume of voids within the layer, which is the total volume of the layer V_{layer} minus the sum of the volume of the monomers (or monomer portions) within that layer $\sum V_d$, to the total volume of the layer, i.e., $\left(V_{layer} - \sum V_d\right)/V_{layer}$. The equivalent radius of a rimmed chondrule is defined as the sum of the radius of the chondrule core and half of the maximum radial extent of the rim to the surface of the chondrule core. The comparison of R_σ and R for an aggregate and a rimmed chondrule is illustrated in Figure 3.1.

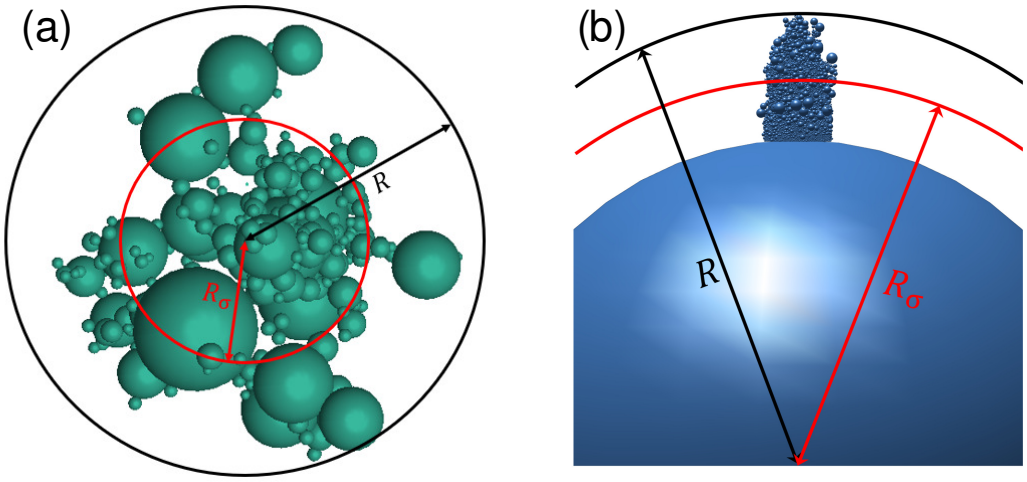

Figure 3.1: Illustration of physical radius R and equivalent radius R_σ for a) a dust aggregate, and b) a dust rim (shown is a dust pile on the chondrule surface). The black arrow indicates the physical radius R, defined as the maximum radial extent from the center of mass for an aggregate (a) or a rimmed chondrule (b). The red arrow indicates the equivalent radius R_σ, as defined in the text.

3.2 "Detailed-MC" Method

The factors that affect the coagulation process are the probability that two particles travel towards each other (determined by their cross-sectional area and relative velocity) and the type of interaction between them, which determines the collision outcome (i.e., sticking, bouncing, restructuring, etc.). We use a "Detailed-MC" method which combines Monte Carlo (MC) method (Ormel et al. 2007; Gillespie 1975) and an N-Body code (Matthews et al. 2012) to model these two factors. When two solid particles are far away from each other, their relative velocity depends largely on the particle sizes, as motion is driven by coupling of the solids to the gas. The Monte Carlo algorithm is used to randomly select colliding particles, where the collision probability is a function of the particle size, as well as determine the elapsed time interval between collisions. At close approach, the detailed collision process is modeled using an N-body algorithm, Aggregate Builder (AB), to determine the collision outcome (Xiang et al. 2019c).

At the beginning of the simulation, a population of dust particles with sizes ranging from 0.5 μm to 10 μm is grouped into 100 logarithmic bins by their radii, and the collision rates C_{ij} between the bins are initialized using the average equivalent radius and mass of particles in each bin. In each iteration, time is advanced by a random interval to the time when the next collision will occur. Then, two bins are selected based on the collision rates C_{ij}, and one particle is chosen from each bin to collide, with the collision outcome modeled by AB.

3.2.1 Monte Carlo Algorithm

The Monte Carlo algorithm is a mathematical method used to simulate the stochastic coagulation model. The fundamental postulate of this algorithm is that there exists a function $C_{ij}(x_i, x_j)d\tau$ which represents the probability that a given pair of particles x_i and x_j will coagulate in the time interval $d\tau$. In our model, assuming the particles are evenly distributed over a volume,

$$C_{ij} = \sigma_{ij}\Delta v_{ij}/V, \tag{3.3}$$

where $\sigma_{ij} = \pi(r_i + r_j)^2$, is the collisional cross section, Δv_{ij} is the relative velocity of the two particles and V is the volume of the simulated region (Gillespie 1975; Ormel et al. 2007). The collision kernel $\sigma_{ij}\Delta v_{ij}$ is equal to the volume that particle x_i sweeps out relative to particle x_j per unit time. The ratio of this volume to the total volume V is proportional to the probability that the two particles collide per unit time, i.e., particles with larger radii and larger relative velocity have a higher chance to collide. At time t, the probability that the next collision will occur in time interval $(t + \tau, t + \tau + d\tau)$ and involve particles x_i and x_j is equivalent to the probability that all the following events occur: (1) no collisions happen in the time interval $(t, t + \tau)$, (2) particles x_i and x_j collide in the differential time interval $(t + \tau, t + \tau + d\tau)$, and (3) no other particles collide in this differential time interval. Since these three events are independent, the probability that they happen simultaneously is the product of

the probabilities of the three events (Gillespie 1975),

$$P(i,j,\tau)d\tau = C_{ij}exp\left(-\tau\sum_{k=l}^{N-1}\sum_{l=k+1}^{N}C_{kl}\right)d\tau. \tag{3.4}$$

By defining the partial sum $C_i = \sum_{j=i+1}^{N} C_{ij}$ and the total sum $C_{tot} = \sum_{i=1}^{N-1} C_i$ (Gillespie 1975), it can be written as the product of three conditional probabilities,

$$\begin{aligned} P(i,j,\tau) &= (C_{tot}exp[-C_{tot}\tau]) \times (C_i/C_{tot}) \times (C_{ij}/C_i) \\ &= p_1(\tau)\cdot p_2(i|\tau)\cdot p_3(j|\tau,i) \end{aligned} \tag{3.5}$$

where

$$\begin{aligned} p_1(\tau) &= C_{tot}exp[-C_{tot}\tau] \\ p_2(i|\tau) &= C_i/C_{tot} \\ p_3(j|\tau,i) &= C_{ij}/C_i. \end{aligned} \tag{3.6}$$

The first term $p_1(\tau)d\tau$ is the probability that the next collision will occur between times $(t+\tau)$ and $(t+\tau+d\tau)$, independent of the colliding pair chosen. The time elapsed between two collisions, according to this probability, is given by $\tau = {C_{tot}}^{-1}ln(1/r)$ with r a random number. $p_2(i|\tau)$ is the probability that particle x_i is chosen to collide, given that the next collision occurs at $(t+\tau)$. $p_3(j|\tau,i)$ represents the probability that the other chosen particle is x_j, given that the next collision occurs at $(t+\tau)$ and involves particle x_i.

$p_2(i|\tau)$ and $p_3(j|\tau,i)$ are both normalized as shown in Formulas 3.6. In order to generate a random number i according to $p_2(i|\tau)$, a random number r_1 from the uniform distribution on the interval [0,1] is generated, and the partial sums C_k are cumulatively added until r_1C_{tot} is just exceeded, meaning that i satisfies the following:

$$\sum_{k=1}^{i-1} C_k < r_1C_{tot} \leq \sum_{k=1}^{i} C_k. \tag{3.7}$$

Dividing each term by C_{tot} yields

$$\sum_{k=1}^{i-1} C_k/C_{tot} < r_1 \leq \sum_{k=1}^{i} C_k/C_{tot}. \tag{3.8}$$

Since $C_k/C_{tot} = p_2(k|\tau)$ is the normalized probability that particle x_i is chosen to collide irrespective of which other particle is selected, the cumulative summation of the probability function is its distribution function,

$$F_{i-1} < r_1 \leqslant F_i \qquad (0 \leqslant F_i \leqslant 1) \tag{3.9}$$

where $F_i = \sum_{k=1}^{i} p_2(k|\tau)$.

Since r_1 follows a uniform distribution on [0, 1], the probability that r_1 falls in interval $[F_{i-1}, F_i]$ equals the length of the interval $F_i - F_{i-1}$ which is equal to $p_2(i|\tau)$. In other words, larger $p_2(i|\tau)$ corresponds to a larger segment on the interval [0,1], resulting in a higher chance for r_1 to fall in that segment. Therefore, the selection procedure for particle x_i can represent its probability in Formula 3.6. Similarly, particle x_j is chosen by generating another random number r_2 from the uniform distribution on the interval [0,1], and cumulatively adding C_{ij} until $r_2 C_i$ is just exceeded,

$$\sum_{l=i+1}^{j-1} C_{il} < r_2 C_i \leq \sum_{l=i+1}^{j} C_{il}. \tag{3.10}$$

In order to reduce the computational cost in calculating the collision probabilities C_{ij}, the range of equivalent radii is divided into 100 logarithmic intervals, and particles of similar size (within the same interval) are binned into the same group. The average equivalent radius of each bin is used to calculate $\widetilde{C_{ij}}$, the collision rate between particles in group i and group j,

$$\widetilde{C_{ij}} = \begin{cases} \frac{1}{2} g_i g_i C_{ii} & \text{for} \quad i = j \\ g_i g_j C_{ij} & \text{for} \quad i \neq j \end{cases} \tag{3.11}$$

where g_i and g_j are the number of particles in the two groups. After particles from group i and j collide, g_i and g_j are both decreased by 1, and the number of particles in

the group which the resulting particle belongs to is increased by 1. At the same time, a particle in the population is randomly chosen to be duplicated, and the number of particles in its group is increased by 1, so that the total number of particles stays the same during the simulation. The abstract volume V is rescaled after each duplication procedure, in order to keep the dust spatial density constant (Ormel et al. 2007).

According to the power law size distribution that we employ to model dust particles, the initial population contains a small number of particles with large radii. In order to reduce the fluctuation caused by small number statistics, instead of creating monomers randomly based on the power law distribution at the beginning of the simulation, we create monomers with evenly spaced radii within the radius range 0.5 μm $\leqslant a \leqslant$ 10 μm, and add weights to particles of different sizes according to the power law distribution. If particles in the i^{th} group have weights $w_1, w_2, ...w_k$, then g_i in Eq. 3.11 equals $\sum_{x=1}^{x=k} w_x$. The physical meaning of a non-integer weight can be interpreted by expanding the space. Suppose the smaller weight of the colliding particle is 0.2: the collision can be imagined to take place in a space which is 5 times as large as the original one, so that there is one such particle in the enlarged volume and at the same time the weight of each species becomes 5 times as large. Therefore, the probability that particles x_i and x_j will collide is: $C_{ij}(new) = 25 w_i(old) w_j(old) \sigma_{ij} \Delta v_{ij} / 5V = 5 C_{ij}(old)$, where 'old' refers to the original space and 'new' refers to the enlarged space. Since the chance that the collision takes place in the original space is 1/5 (the original volume is 1/5 of the enlarged volume), the probability that particles x_i and x_j will collide in the original space is $C_{ij}(new)/5$, which equals to $C_{ij}(old)$.

3.2.2 Collision Resolution (Aggregate Builder)

Once the dust particles are selected, the detailed interaction is modeled using an N-body code, Aggregate Builder (Matthews et al. 2012), taking into account the morphology of the aggregates, the trajectory of the incoming particle, and the

electrostatic interaction. For collisions between two dust particles, one of the particles is placed with its center of mass at the origin as the target, and an incoming particle is shot towards the target's COM plus an offset up to $b = 0.2 \times (R_1 + R_2)$, where R_1 and R_2 are the maximum radii of the target and the incoming aggregates respectively (this factor is chosen for computational expediency, to reduce the number of missed interactions). The relative velocities between the two aggregates are set assuming the dust is coupled to turbulent eddies in a protoplanetary disk (Ormel et al. 2007), calculated by Eq. 2.89. The initial distance between two charged particles is set such that the potential energy due to the charge interactions is less than 90% of the initial kinetic energy, while in the neutral case, it is set to be $2.5 \times (R_1 + R_2)$. The linear acceleration $\vec{a}_v$ and angular acceleration $\vec{a}_\omega$ of a dust particle are given by

$$m\vec{a}_v = \vec{F} \tag{3.12}$$

$$I\vec{a}_\omega = \vec{N} \tag{3.13}$$

where m and I are the mass and moment of inertia of the particle; $\vec{F}$ and $\vec{N}$ are the electric force and torque acting on the particle, given by Formulas 2.73 and 2.76.

At each time step, the positions, velocities and accelerations of the target and incoming particles are updated using a 5th-order Runge Kutta method. We are interested in detecting true collisions, where constituent members of the two particles physically overlap. If the two particles are separated by a distance smaller than the sum of their radii, a collision check determines if any two monomers in the target and incoming aggregates overlap. In the case of an overlap, the incoming particle is backed up until the overlap is within a small tolerance ($0.5 \times 10^{-4} \mu m$), and the critical bouncing velocity is calculated for the two aggregates to determine whether they stick or bounce: the particles stick if the relative velocity is lower than the critical bouncing velocity, and bounce otherwise. A missed collision is detected when the two particles are moving away from each other. This can be caused by one particle going

through the gaps within the other particle, or the electrostatic repulsion between two like-charged particles. An illustration of the difference in the collision results for charged particles with different relative velocities is shown in Figure 3.2. In the case of bouncing or a missed collision, the code proceeds to the next iteration and new dust particles are selected.

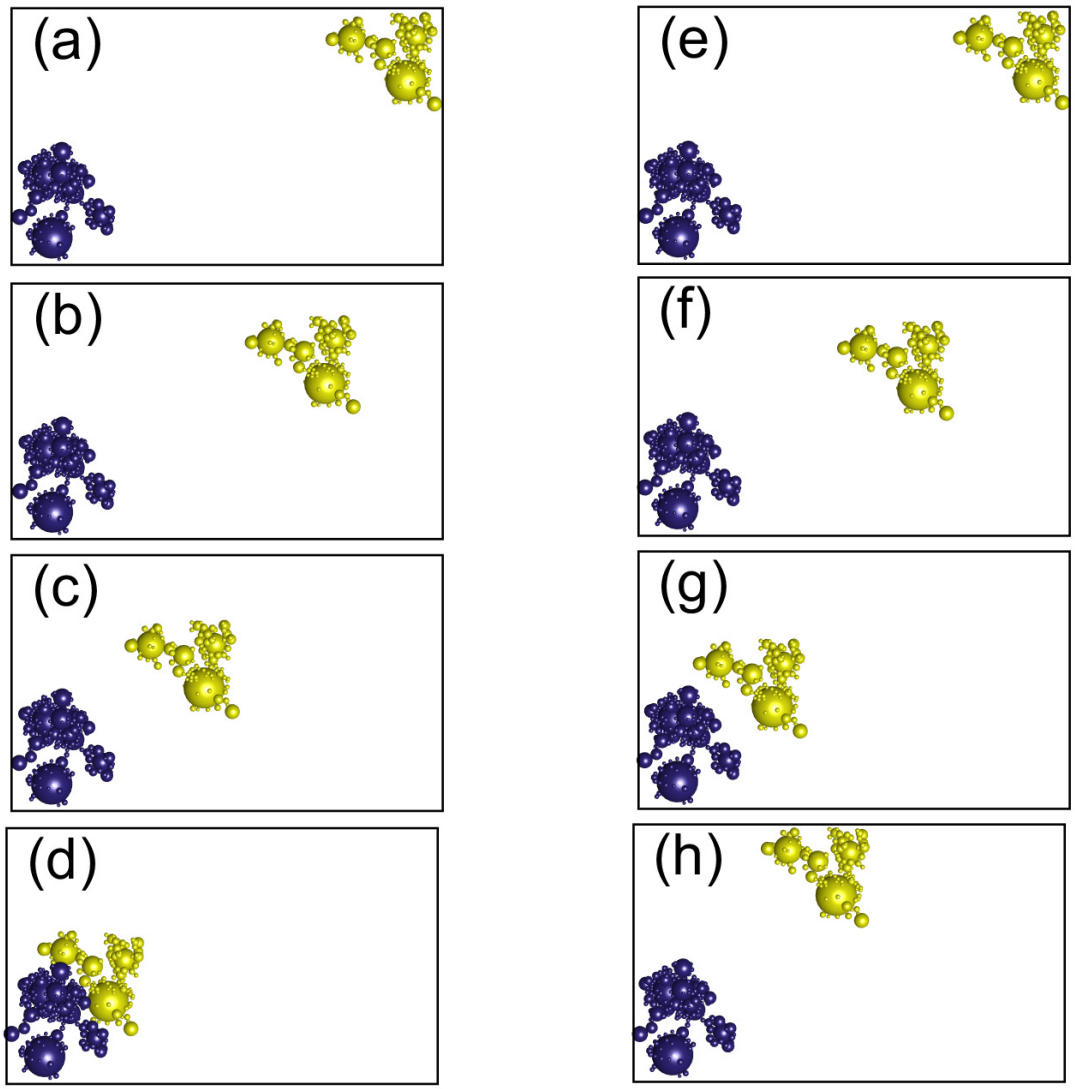

Figure 3.2: Illustration of collision process of charged aggregates with a surface potential of -0.1 V. The blue aggregate is the target, while the yellow aggregate travels towards the target's COM plus an offset. a, b, c, d) show a hit-and-stick collision with an initial relative velocity of 0.1 m/s, and e, f, g, h) show a missed collision due to electrostatic repulsion with an initial relative velocity of 0.002 m/s. Each row shows snapshots of the two particles at different time steps (increased elapsed time from top to bottom).

Upon a successful hit-and-stick collision, the two aggregates are connected at the point of contact, and the total mass, charge, spin and moment of inertia are calculated for the resulting aggregate. This new aggregate replaces the incoming aggregate in the library. Subsequently, another aggregate is randomly chosen to replace the target aggregate, so that the total number of aggregates from the library stays constant. The collision probabilities C_{ij} are updated based on the new average equivalent radius of each bin and the change in the population of the dust particles. For each hit, bounce and miss, the masses, radii, equivalent radii, compactness factors, charges, relative velocity of the two particles, and the time interval between two interactions are recorded. The detailed flow chart of this process is shown in Figure 3.3.

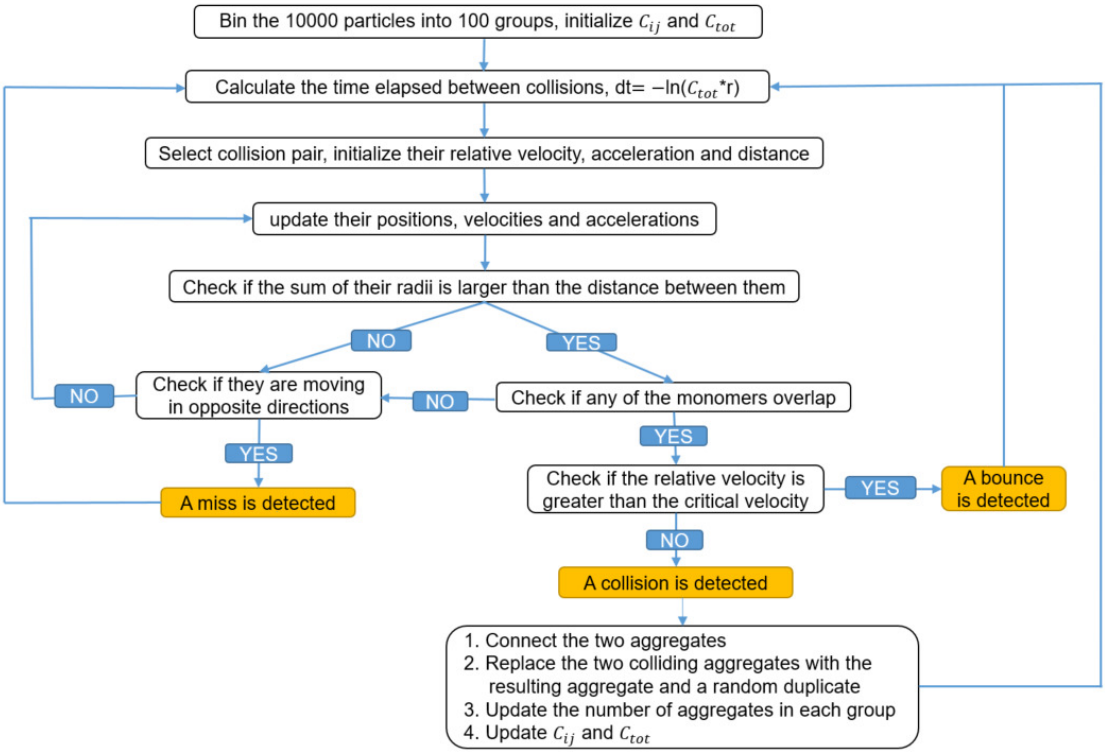

Figure 3.3. Flow chart of the simulation of particle collision.

3.3 Modifications for Building Chondrule Rims

3.3.1 Modified MC Algorithm

In modeling FGR formation, the collision is between a fixed target chondrule *ch* and a randomly chosen dust particle *d*. The probability that the two objects collide per unit time is

$$C_{ch,d} = \sigma_{ch,d} \Delta v_{ch,d} / V. \tag{3.14}$$

The first step in this method is to determine the random time interval between the collection of dust particles, consistent with the collision probabilities $C_{ch,d}$ (Gillespie 1975; see Section 3.2.1). The probability per unit time of collecting any dust particle is

$$C_{tot} = \sum_{i=1}^{N} C_{ch,i}, \tag{3.15}$$

with N the total number of dust particles. During a given time interval τ, the probability of collecting any dust particle is proportional to

$$P = exp[-C_{tot}\tau]. \tag{3.16}$$

The time elapsed between two collisions, according to this probability, is given by $\tau = -ln(r_1)/C_{tot}$, with r_1 a random number between zero and one. A second random number r_2 is used to select the incoming dust particle d by finding the smallest integer satisfying

$$\sum_{i=1}^{d} C_{ch,i} > r_2 C_{tot}. \tag{3.17}$$

In order to reduce the computational cost in calculating the collision probabilities $C_{ch,d}$, the range of the equivalent radii of dust particles is divided into 100 logarithmic intervals, and particles of similar size (within the same interval) are binned into the same group. The average equivalent radius of each bin is used to calculate $\widetilde{C_{ch,d}}$, the

collision rate between particles in the group d and the chondrule ch,

$$\widetilde{C_{ch,d}} = g_d C_{ch,d}, \tag{3.18}$$

where g_d is the number of particles in group d (Ormel et at. 2007).

3.3.2 Modified Aggregate Builder

For collisions between the chondrule and dust particles, the chondrule is placed as a target with its center of mass at the origin. For computational expediency, we restrict dust particles to accumulate on a circular patch 100 μm in diameter on the chondrule surface, and assume that dust is accumulated isotropically. The elapsed time between two consecutive interactions is multiplied by the ratio of the area of the chondrule surface to the area of the patch, in order to take into account the time required to build the rest of the rim. In each iteration, one dust particle is selected randomly from the dust population according to the previously computed collision rates, and is shot towards a randomly selected point on the target area from a random direction. The angle between this direction and the normal to the patch at the selected point is uniformly distributed between 0° and 60°, so that it is less likely that dust particles impact the side of the dust pile, as illustrated in Fig. 3.4. Although in a natural collision dust particles could approach the chondrule surface at more oblique angles, it is highly likely that such particles would be blocked by the irregular distribution of dust particles near the patch that are not included in our simulation. The initial distance between the chondrule and the incoming dust particle is set to be $2.5R_{\rm ch}$, with $R_{\rm ch}$ the radius of the chondrule. The initial relative velocity between the chondrule and the dust grains is set assuming that the dust is coupled to the gas in the solar nebula, as described in Section 2.2.

Upon a successful collision, in addition to sticking at the point of contact or bouncing, the incoming particle can also roll on the surface of chondrule (which results in compaction), depending on its kinetic energy. During rolling, the momentum of

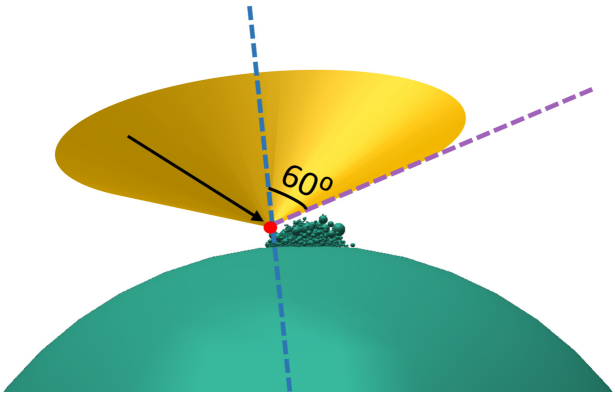

Figure 3.4: Schematic showing the geometry of the collision between a dust particle and the chondrule surface. The green sphere represents the chondrule core with a dust pile on the surface, and the red spot is a randomly selected point on the dust pile. The yellow cone has its vertex at the selected point and its axis parallel to the normal of the surface of chondrule core at that point, with an angle of 60° between the cone axis (blue dashed line) and the cone edge (purple dashed line). The incoming dust particle can be shot towards the point from any direction within the cone, with the black arrow as an example.

the incoming particle is decomposed into directions tangential and perpendicular to the point of contact. The kinetic energy associated with the tangential component of the momentum is used for the rolling of the incoming particle (if it exceeds the critical rolling energy). The perpendicular component is transferred to the sphere in contact with the incoming particle, and is decomposed again at its contact point with another sphere. In this manner the momentum of the incoming particle is transferred to the inner spheres of the dust rim, and the energy of e_{roll} is dissipated as a sphere rolls a distance of 1 $\mathring{A}$. The momentum stops transferring inward when the remaining energy is not sufficient to cause any rolling ($E < e_{roll}$). Figure 3.5 illustrates the process of momentum transfer. Note that the grains do not necessarily stop rolling simultaneously, as each sub system has different kinetic energy. For example, grain A may stop rolling on grain B due to the depletion of its tangential momentum but may still roll together with grain B and C on top of grain D.

The energy required to initiate rolling (e_{roll}) is much smaller than the energy required for breaking a contact, while the energy needed to roll a large distance is

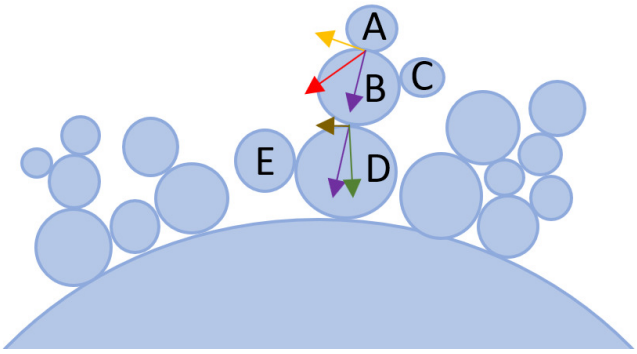

Figure 3.5: Illustration of momentum transfer within the dust rim. When the incoming grain A hits grain B, its momentum (red) is decomposed into the tangential component (yellow) which makes grain A roll counterclockwise on the surface of grain B and the normal component (purple) which is transferred to grain B. The momentum of grain B gets decomposed again at the contact point between grain B and grain D. The tangential component (brown) enables grains B, A and C roll counterclockwise as a whole on the surface of D, and the normal component is transferred to grain D.

similar to that for breaking a contact. Therefore, it is easy for the particles to start rolling for a small distance, but difficult for them to roll a large distance without breaking the contact. The criteria for the different outcomes are (a) for sticking at the point of contact: the relative velocity is lower than the critical rolling velocity; (b) for rolling: the relative velocity is greater than the critical rolling velocity [determined by the critical rolling energy as in Eq. 2.93 and the mass of the incoming particle] and lower than the critical bouncing velocity; (c) for bouncing: the relative velocity is greater than the critical bouncing velocity; (d) for missing: particles are moving away from each other. In our simulation, particles have low relatively velocities and no bouncing collision is detected.

3.4 Physical Parameters Used in the Simulation

3.4.1 Disk Parameters

Coagulation was modeled for conditions at the midplane of a turbulent protoplanetary disk, at a distance of 1 AU from the central young stellar object (YSO), with a gas temperature (T) of 280 K. The average molecular mass u is taken to be

2.33 g/mol, and the sound speed is given by

$$c_g = (\gamma k_B T/um_H)^{1/2}\,, \tag{3.19}$$

with γ the ratio of C_p to C_v for diatomic molecule, k_B the Boltzmann constant, and m_H the mass of hydrogen. The molecular viscosity of the gas is given by

$$v_m = \frac{\sqrt{(2/\pi)}um_H c_g}{\rho_g \sigma_{coll}}, \tag{3.20}$$

with ρ_g the gas density and σ_{coll} the collisional cross section of the gas composed of molecular hydrogen and helium with the density ratio of 10 (Okuzumi et al. 2011b; Krumholz 2015), $\sigma_{coll} = 2\times10^{-19}\ m^2$. The ratio of the dust density to the gas density is assumed to be 0.01 (Tricco et al. 2017).

3.4.2 Plasma Conditions

There are several mechanisms that can contribute to the ionization of the protoplanetary disk, such as cosmic rays (CRs), UV radiations, X-rays, radionuclides. In our simulation, the plasma environment is assumed to be hydrogen with equal electron and ion temperature, $T_e = T_i = 280$ K, as the plasma thermalizes with the gas due to collisions. In the case of low dust density, a negligible percentage of the electrons reside on the dust grains, and the number density of electrons and ions in the gas are equal: $n_e = n_i = 3.5 \times 10^8\ m^{-3}$ (Horanyi & Goertz, 1990). For high dust density, the ratio of free electrons to free ions is reduced due to electron depletion, and we use n_e/n_i =0.1, 0.5. The corresponding surface potentials of the dust particles charged by primary current are -0.061 V, -0.048 V and -0.020 V for n_e/n_i = 1, 0.5, and 0.1 respectively. In the simulation of chondrule dust rims (Chapter six), we compare these three plasma environments with a neutral environment where the particles are not charged. On the other hand, dust can also be charged by secondary electron emission and photoelectric emission from high energy UV and X rays. In the inner solar system, impinging electrons do not have sufficient energy to knock

secondary electrons off dust particles, and thus the main charging processes in this region are the primary plasma currents and photoelectric emission. The level of UV radiation varies over locations in the disk; the inner, denser regions are less exposed to radiation, and therefore the effect of photoelectric emission is reduced. The photon flux, i.e., the product of absorption efficiency, yield and solar flux (Ma et al. 2013), ranges from 5×10^{12} $m^{-2}s^{-1}$ to 1.5×10^{13} $m^{-2}s^{-1}$ at 1 AU (Tobiska 1991), which can charge dust particles up to a few volts (Ma et al, 2013). A porous aggregate can collect more free electrons and absorb more UV photons due to greater surface area than can a compact aggregate of the same mass. Therefore, the efficiencies of both the plasma charging and photoelectric emission are positively related to the open area of an aggregate, and the OML_LOS method used for plasma charging is also applicable to photoelectric emission (Ma et al. 2013). In order to explore the process of dust growth under various charging conditions, we do not specify the value of photon flux, but rather integrate the effect of photoelectric emission into the dust surface potential. We employ values of $|V_s| = 0$, 0.1, 0.5, 1 and 5 V to cover the range of possible surface potentials due to charging through direct collection of plasma particles or charging through photoemission (Matthews et al. 2012; Ivlev et al. 2016) in the simulation of dust coagulation (Chapter four). Although we simulate dust growth at 1 AU, these results can be applied to other regions of the disk with the same surface potential.

3.4.3 Turbulence Levels

As discussed in Section 1.1.3, neither the origin nor the precise value of the turbulence strength in protoplanetary disks is certain. In this work, we do not specify the origin of the turbulence but characterize its strength through dimensionless hydrodynamical viscosity parameter α, which describes the degree of increased viscosity caused by turbulence (Shakura & Sunyaev 1973; Lynden-Bell & Pringle 1974). The values of α often considered range from $\alpha \sim 10^{-6}$ to 0.1 (Hartmann et al. 1998; Cuzzi

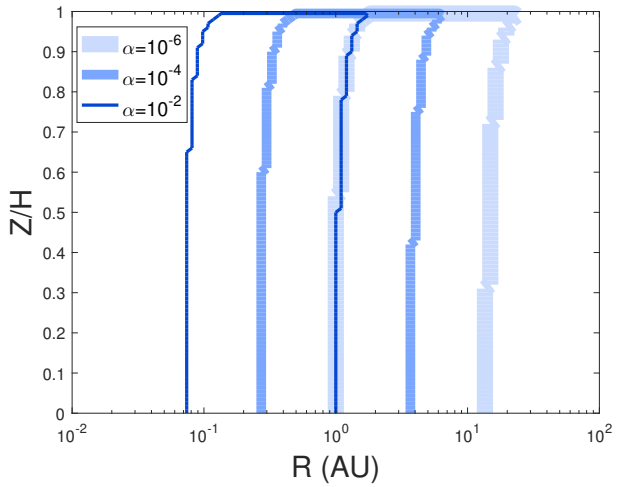

Figure 3.6: Contour lines indicating the regions in a PPD, where the relative velocity between a 0.5-μm-radius particle and a 10-μm-radius particle is within the limits of [0.12 1.21] m/s, for turbulence strengths $\alpha = 10^{-6}$, 10^{-4}, and 10^{-2}.

2004; Ormel et al. 2008, Carballido 2011), and we investigate levels of turbulence with α equal to $10^{-1}, 10^{-2}, 10^{-3}, 10^{-4}, 10^{-5}, 10^{-6}$.

The environmental parameters that determine the relative velocity between particles are the radial distance, scale height, and the turbulence strength, where the scale height is defined as

$$H = 2\sqrt{\pi}\frac{c_g}{\Omega}, \tag{3.21}$$

with Ω the Keplerian angular velocity. Varying the turbulence level at a fixed disk location can result in the same range of relative velocities as changing the disk location with a fixed turbulence level. For example, the relative velocity between two particles, with radii of 0.5 μm and 10 μm respectively, at 1 AU (midplane) is 0.12 m/s for $\alpha = 10^{-6}$ and 1.21 m/s for $\alpha = 10^{-2}$. The contour lines in Figure 3.6 indicate the regions in the disk where such a particle pair has a relative velocity within these two limits, for various turbulence strengths. Therefore, although we model the dust coagulation at a specific location in the disk (midplane at 1 AU) and adopt specific turbulence levels, the results can be applied to other regions of the disk by adjusting the turbulence strength.

In addition to the turbulence level, the process of dust collision is also affected by the charging condition. The combined effect of these two factors can be characterized by the ratio PE/KE, where PE is the electrostatic potential energy of the dust grain at the point of impact, given by $PE = \frac{\epsilon_0 Q_i Q_j}{4\pi r_{i,j}}$, with Q_i and Q_j the charges of the colliding dust particles and $r_{i,j}$ the distance between them. The kinetic energy of the colliding pair when the incoming particle is far from the target is $KE = \frac{1}{2} u v_{rel}^2$, where u is the reduced mass of the two particles, $u = \frac{m_i m_j}{m_i + m_j}$, with m_i and m_j their individual masses, and v_{rel} is the relative velocity calculated from Eq. 2.89. Given the combined turbulence and charge levels, the results are broadly applicable over a large region of the disk where conditions match a given PE/KE.

Some content in this chapter was published in Xiang et al. 2017a, 2017b, 2019a, 2019b, 2019c.

CHAPTER FOUR

Aggregate Growth in a Protoplanetary Disk Using Molecular Dynamics

This chapter submitted as [201]: Chuchu Xiang, Lorin S. Matthews, Augusto Carballido, Truell W. Hyde, "Detailed Model of the Growth of Fluffy Dust Aggregates in a Protoplanetary Disk: Effects of Nebular Conditions," arXiv:1911.04589.

4.1 Introduction

Electric charging of dust grains is an important process in PPDs. This process plays a key role in the ionization-recombination state of the plasma environment, particularly through the removal of electrons from the gas phase. The magneto-hydrodynamics of PPDs are strongly dependent on the abundance of small grains (Mori & Okuzumi 2016; Okuzumi et al. 2019), which are efficient electron sinks. Non-zero grain charges affect the dynamical interactions between grains (Matthews et al. 2012) and, by extension, the coagulation mechanism that leads to macroscopic precursors of planetesimals. Coulomb interactions between colliding dust pairs can significantly alter the collision outcome (Matthews et al. 2012; Okuzumi 2009; Okuzumi et al. 2011a,b): growth is strongly inhibited, or even halted, by the electrostatic repulsion between colliding aggregates, especially in locations with weak turbulence (disk radius $r \leqslant 20$ AU or scale height $|z| \leqslant 2H$; Okuzumi 2009).

Various collision outcomes including bouncing (Zsom et al. 2010), erosion (Krijt et al. 2015) and fragmentation (Brauer et al. 2008, Birnstiel et al. 2012) have been modeled theoretically and experimentally (Blum 2004), with both laboratory observation and numerical simulations revealing that aggregates have a porous structure. The internal density of aggregates changes upon collision, and in turn, affects future collision processes. An understanding of the porous structure of dust aggregates is crucial to determine their charge distribution. Although significant progress has been

made in calculating the amount of charge acquired by non-porous grains (e.g., Ivlev et al. 2016), such calculations remain challenging when applied to irregular, fluffy grains (Okuzumi 2009; Matthews et al. 2012). Aggregate charging depends markedly on the open area of the aggregates: porous aggregates can acquire more charge than compact aggregates of the same mass in the same plasma environment (Matthews et al. 2012). Thus, improved models of the growth of charged dust in weakly-ionized PPDs need to take the evolution of dust aggregate porosity into account (Matthews et al. 2012).

Okuzumi (2009) focused on early stages of dust evolution and modeled collisions between aggregates of a fixed mass ratio formed of monodisperse spherical monomers, with the collision outcome limited to hit-and-stick. The simulation results were used to construct a recipe for the porosity change of the aggregates as well as a formula for collisional cross sections. However, Okuzumi (2009) did not model the morphology of particles and therefore did not factor in the impact of the rotation of charged particles on the porosity of the resulting aggregates. In addition, the initial size distribution of dust grains, generally assumed to be the interstellar medium distribution (a power law with index -3.5; Mathis et al. 1977), is relevant to collisional outcomes. Not only do collisions occur between monomers of different sizes, but the collisions will occur between monomers and aggregates which vary greatly in size, as well as between aggregates of different sizes, based on their collision probability. Therefore, assuming a fixed mass ratio between colliding pairs can not reflect the real coagulation process, and also significantly limits the diversity of the aggregate structures, since the structure of an aggregate strongly depends on its formation history.

In this study, we examine the evolution of charged and neutral dust populations, considering an initial population of spherical monomers whose radii follow the MRN distribution. A population of aggregates is built by considering the probability of collisions between particles of all sizes present in the population. A detailed model of the

collision process, which takes into account two key physical characteristics (porosity and charge), is used to resolve the collision outcome. Here we restrict the analysis to the hit-and-stick regime and identify missed collisions. We parameterize the strength of turbulence in a PPD, and analyze the influence of the turbulent strength on the electrostatic repulsion experienced by colliding aggregates. The resulting characteristics of the dust aggregates including the monomer size as well as porosity and the time evolution of the dust population in different environments are presented, and the relationship between the properties of colliding particles and the collision outcomes is analyzed.

4.2 Results

The simulation is restricted to the hit-and-stick regime before the bouncing criterion is met, i.e., more than 5% of 100 consecutive collisions results in bouncing. At this point, restructuring is expected to play a large role in the evolution of the population. In general, the bouncing probability increases as the population grows. However, it develops differently for populations with different charges, due to their different growth behaviors, as shown in Figure 4.1. Particles in neutral and weakly charged populations grow collectively, and the bouncing probability increases quasi-linearly after the initial stage. On the other hand, in highly charged cases, the growth is concentrated on a small proportion of the population while the majority of the population grows slowly. Therefore, a lot of hit-and-stick collisions still occur after meeting the bouncing criterion. The elapsed times and maximum particle sizes in populations when the bouncing criterion is met are listed in Table 4.1 and Table 4.2. See section 4.2.3 for more discussion about different growth modes of dust populations in different environments.

In this section we compare the collision outcomes, the morphology of the resulting aggregates, as well as the evolution of dust populations for charged and neutral aggregates, in varying levels of turbulence.

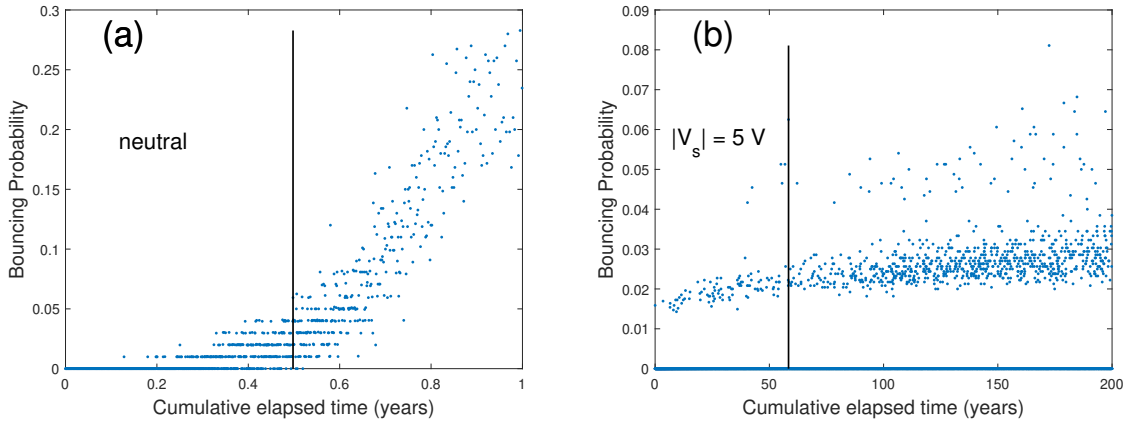

Figure 4.1: Bouncing probability as a function of elapsed time for a) neutral and b) charged (surface potential $|V_s| = 5$ V) populations, with turbulence level $\alpha = 10^{-2}$. Each point represents the ratio of the number of bouncing collisions to the total number of interactions for 100 consecutive interactions. The black vertical lines indicate the time at which the bouncing criterion is met.

Table 4.1: Maximum elapsed time when bouncing criterion is met (more than 5% of previous 100 collisions result in bouncing), for different dust surface potentials (V_s) and turbulence levels (α).

α / $\lvert V_s \rvert$	10^{-2}	10^{-4}	10^{-6}
neutral	0.5	3.3	24.2
$0.1V$	0.4	3.8	58.3
$0.5V$	1.0	52.0	2962.2
$1V$	3.8	568.4	17987.0
$5V$	58.4	23465.1	

Figure 4.2 shows examples of aggregates formed in different plasma conditions with turbulence strength $\alpha = 10^{-6}$. The selected aggregates have similar equivalent radii, but the difference between them is readily apparent: the neutral aggregate and aggregate with the smallest charge (Figs. 4.2a, 4.2b) are the most porous and contain large numbers of the smallest monomers ($< 1\ \mu m$). Compared to the neutral aggregate, the aggregate with the smallest charge has the greatest proportion of small monomers which tend to be attached to large monomers. As the surface potential of the particles increases, fewer small monomers are incorporated into the aggregates,

Table 4.2: Average equivalent radius of the top 0.5% largest particles when bouncing criterion is met (more than 5% of previous 100 collisions result in bouncing), for different dust surface potentials (V_s) and turbulence levels (α). The populations exhibiting runaway growth are highlighted in bold.

α / $\lvert V_s \rvert$	10^{-2}	10^{-4}	10^{-6}
Neutral	14.8±0.5	20.1±1.1	60.9±4.1
0.1 V	15.3±0.5	19.5±1.4	48.7±7.6
0.5 V	16.5±0.5	21.7±0.7	**81.2±0.4**
1 V	20.0±0.4	**44.8±2.0**	**116.2±0.2**
5 V	**23.1±0.8**	**64.5±0.4**	

the minimum size of monomers increases, and the porosity decreases (Figs. 4.2c, 4.2d). In addition, the highly charged aggregates are more spherical (lower aspect ratios) and symmetrical, while the neutral and weakly charged particles have more irregular shapes.

4.2.1 Monomer Size Distribution within Aggregates

As shown in Figure 4.2, highly charged aggregates contain larger monomers than do weakly charged and neutral aggregates, as small monomers have a higher charge to mass ratio and are repelled from highly charged grains. As aggregates grow larger, they develop greater relative velocity with respect to small dust grains, which enable these grains to overcome the electrostatic barrier and be incorporated into the large aggregates. As a result, for environments with low turbulence level and high surface potential, the percentages of small ($r < 1.43$ μm) and medium (1.43 - 7.14 μm) monomers within aggregates increase over time, while the percentage of large monomers (7.14 - 10 μm) decreases over time, leading to a decrease in the average monomer size within aggregates [the small monomers and large monomers are defined as the bottom and top 20% (in mass) of the initial population]. In a strongly turbulent environment, neutral and weakly charged grains incorporate a greater percentage of

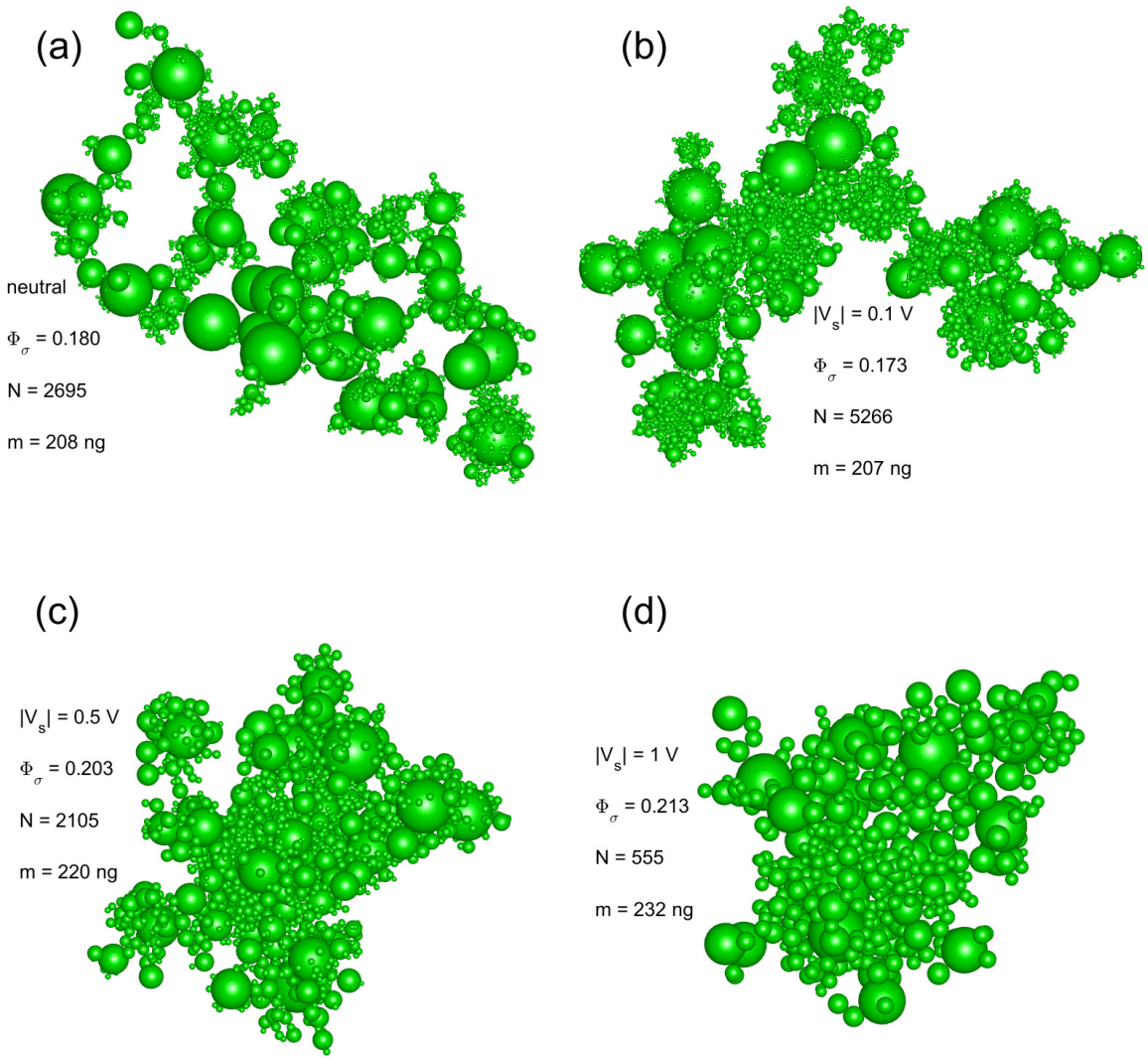

Figure 4.2: Representative aggregates with an equivalent radius of $R_\sigma \sim 48\ \mu m$ formed in environments with turbulence level $\alpha = 10^{-6}$. The surface potential $|V_s|$ is a) neutral, b) 0.1 V, c), 0.5 V and d) 1 V. The compactness factor Φ_σ, number of monomers N and the mass m are shown for each aggregate.

large monomers over time, but the average monomer size within aggregates is quasi-constant.

A comparison of the probability distribution of the monomer sizes incorporated into the aggregates at the end of the simulation (when more than 5% of collisions result in bouncing) is shown in Figure 4.3. At all turbulence levels, the distribution of monomers in the neutral and weakly charged aggregates matches the initial distribution of monomers sizes. As the surface potential increases, the monomer

distribution shifts towards larger monomer sizes, and the shift increases with lower turbulence level. For environments with very low turbulence and very high charge, small monomers are not incorporated into aggregates due to repulsion. [note that for $\alpha = 10^{-4}$ and $|V_s| = 5$ V, the curve is shifted beyond the monomer size of 3 μm, reflecting the fact that aggregate growth is very slow as there are so few of the large monomers which can overcome the Coulomb repulsion barrier.]

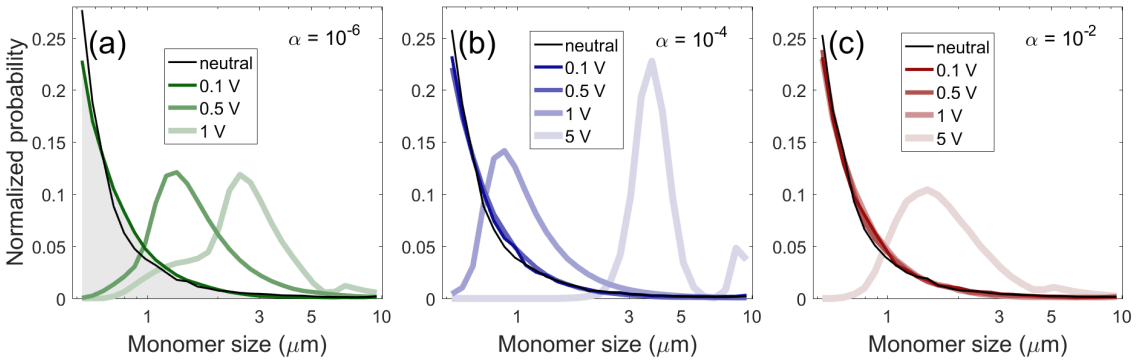

Figure 4.3: Monomer size distribution within aggregates (surface potential $|V_s| = 0$, 0.1, 0.5, 1, 5 V; in order of decreasing color shades), at the end of the simulation (when the bouncing criterion is met). The shadowed area in a) indicates the size distribution of the initial population. Turbulence levels are $\alpha = 10^{-6}$ for a), $\alpha = 10^{-4}$ for b) and $\alpha = 10^{-2}$ for c).

4.2.2 Porosity

Porosity plays an important role in the collision probability because open structures couple more strongly to the gas, which reduces the relative velocity between grains. Although open, porous aggregates have a larger collisional cross section, which enhances the collision rate and aids them in out-growing the radial drift barrier (Garcia et al. 2016), small aggregates can pass through the gaps of the extended arms, making collisions less likely. In addition, the diversity of aggregate porosity can enhance collisions between particles of similar sizes by increasing the difference between their friction times.

Charge influences the porosity of aggregates in different ways, and the porosity of the resulting aggregates is a balance between several factors. The electrostatic force

causes small grains to be repelled, and the lack of small monomers filling in the gaps of aggregates increases the aggregate porosity. On the other hand, low-velocity collisions enable particles to have sufficient time to alter their path or rotate to minimize the potential energy of the configuration, producing more compact structures. This effect is most noticeable for weakly turbulent and/or highly charged environments, in which grains either have small turbulent velocities or are slowed down greatly by the electrostatic repulsion.

The distributions of compactness factor of all aggregates within the population are compared for all charging conditions and turbulence levels, as shown in Figure 4.4. The porosity of aggregates increases as they grow in size through hit-and-stick collisions. Therefore, as time progresses, a population shifts to lower compactness factors, i.e., contains a greater fraction of porous aggregates. The neutral and weakly charged populations have narrower distributions, and the peaks shift towards smaller compactness factor (greater porosity) as the populations grow and turbulence level decreases. On the other hand, the highly charged populations have broader distributions which change very little over time.

Figure 4.5 shows the mean porosity of all aggregates within the population at different time points. Each circle represents a time point which progresses from top to bottom in each column. For all environmental conditions, the mean porosity increases as the population grows. Given the same turbulence level, aggregates in highly charged populations are more compact than those with a low charge after equal elapsed time. However, at the time when the bouncing criterion is met, the highly charged aggregates are more porous in strong turbulence ($\alpha = 10^{-2}$) and more compact in weak turbulence ($\alpha = 10^{-4}$, 10^{-6}). The size of the circle represents the ratio of the number of aggregates to the total number of particles in the population for Fig. 4.5a, and the ratio of the mass of aggregates to the total mass of the population for Fig. 4.5b. It is seen that for neutral or weakly charged dust, the number of

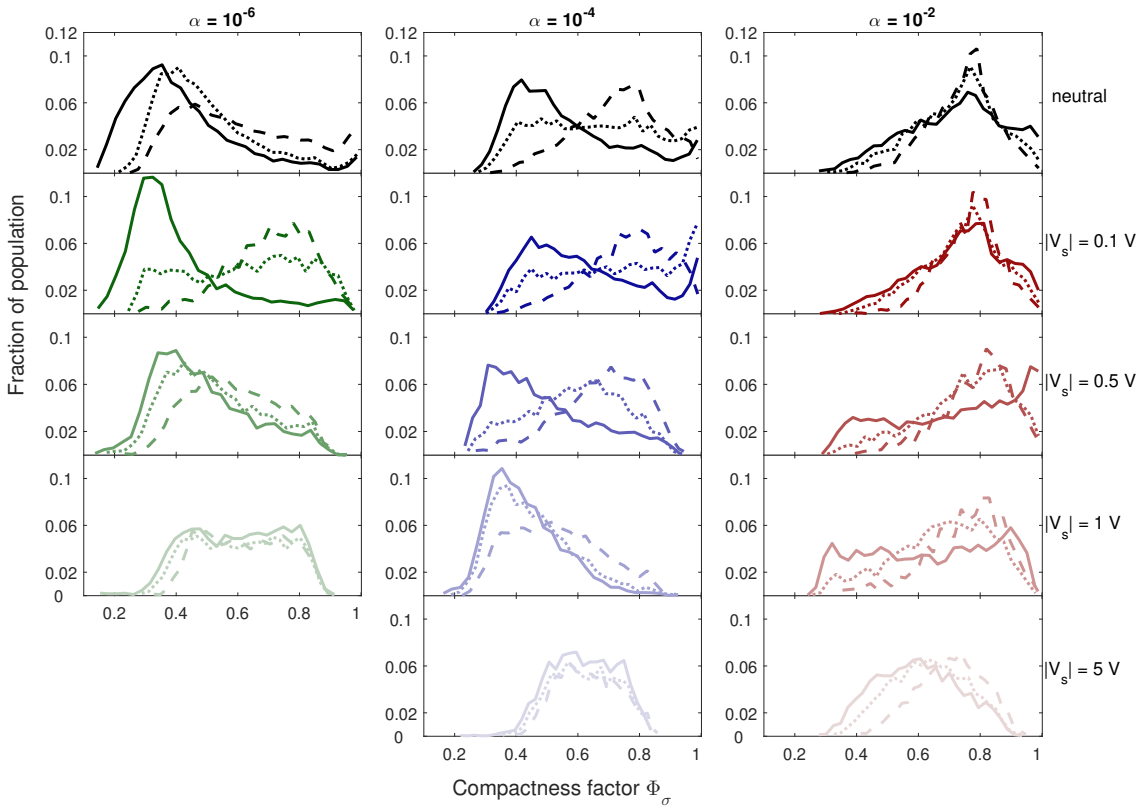

Figure 4.4: Distribution of compactness factor in the population for aggregates with more than 10 monomers and surface potential $|V_s| = 0$, 0.1, 0.5, 1, 5 V, in order of decreasing color shades (from top to bottom). The turbulence levels are $\alpha = 10^{-6}$ for the left column (green), $\alpha = 10^{-4}$ for the middle column (blue) and $\alpha = 10^{-2}$ for the right column (red). The solid curves represent the time when 5% of collisions result in bouncing. The dashed and dotted curves represent 1/3 and 2/3 of the total elapsed time.

aggregates present grows in time (Fig. 4.5a) just as the fraction of the mass contained in aggregates grows (Fig. 4.5b). In contrast, for highly charged dust populations ($|V_s| \geqslant 0.5$ V for $\alpha = 10^{-6}$; $|V_s| \geqslant 1$ V for $\alpha = 10^{-4}$; $|V_s| \geqslant 5$ V for $\alpha = 10^{-2}$), the number of aggregates stays small (Fig. 4.5a) while the fraction of mass within the total population contained in aggregates grows (Fig. 4.5b). This indicates that in the highly charged populations the dust growth is concentrated on a small number of particles, indicating runaway growth (see next section for more discussion).

Comparisons of the compactness factor for charged and neutral aggregates for different charging conditions and turbulence levels are shown in Figure 4.6. Here the data is shown relative to the porosity of neutral aggregates with the same equivalent

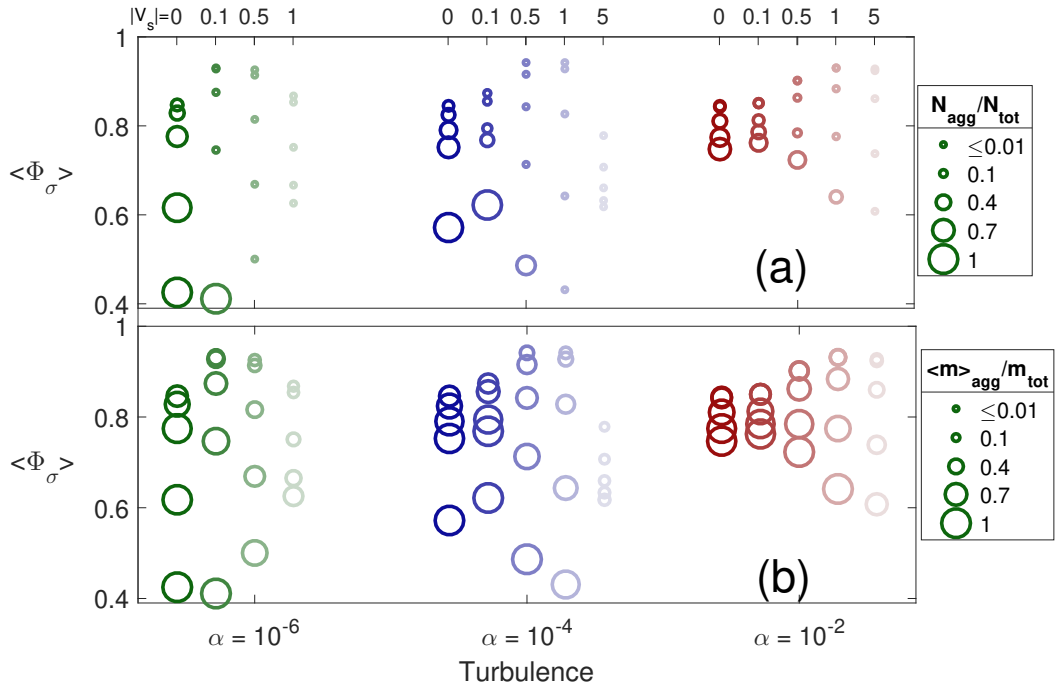

Figure 4.5: Average compactness factor of all aggregates within the population, at different time points. In each column, the circles progress in time from top to bottom for equally spaced times until the bouncing criterion is met. The size of the circle represents the ratio of the number of aggregates to the total number of particles in the population for a), and the ratio of the mass of aggregates to the total mass of the population for b).

radius. For aggregates smaller than $\sim 10\ \mu m$, charged particles are more compact ($\Delta\Phi_\sigma > 0$) than neutral particles in all cases. For large aggregates, charged particles are either more compact or more porous ($\Delta\Phi_\sigma < 0$) than neutral particles, depending on the environmental conditions. In general, highly charged particles tend to be more compact than those with a low charge for the same turbulence level, consistent with Figure 4.4.

4.2.3 Time Evolution of the Aggregate Population

Fig. 4.7 compares the size distribution of the dust grains in the population for all of the turbulence strengths and charging levels when the bouncing criterion is met for each population. In highly charged cases ($|V_s| \geqslant 0.5$ V for $\alpha = 10^{-6}$; $|V_s| \geqslant 1$ V for $\alpha = 10^{-4}$; $|V_s| \geqslant 5$ V for $\alpha = 10^{-2}$), dust particles grow to a larger size than in neutral and weakly charged cases, and the large particles represent a very small proportion of

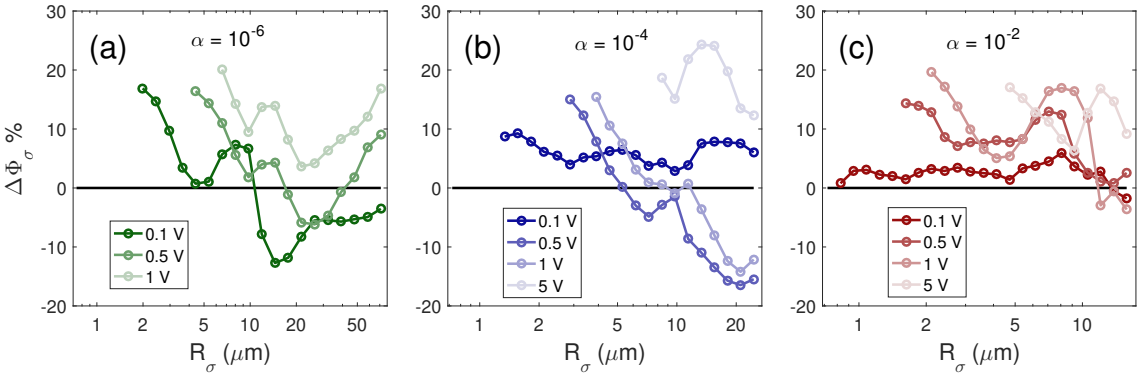

Figure 4.6: Percent difference of compactness factor for charged aggregates relative to neutral aggregates as a function of equivalent radius. Turbulence levels are $\alpha = 10^{-6}$ for a), $\alpha = 10^{-4}$ for b) and $\alpha = 10^{-2}$ for c). Results shown are for all aggregates formed over the course of the simulation until the bouncing criterion is met.

the population. Overall, the size distributions of the highly charged populations do not deviate much from the initial size distribution, meaning that a lot of monomers and small aggregates remain in the population while few large aggregates grow in size, which indicates a runaway growth. In contrast, for neutral and weakly charged populations, almost all monomers have collided and formed aggregates before the bouncing criterion is met, and the size distributions peak around the average particle size. The deviation of the population from the initial mass distribution is negatively correlated with the charge level and turbulence level.

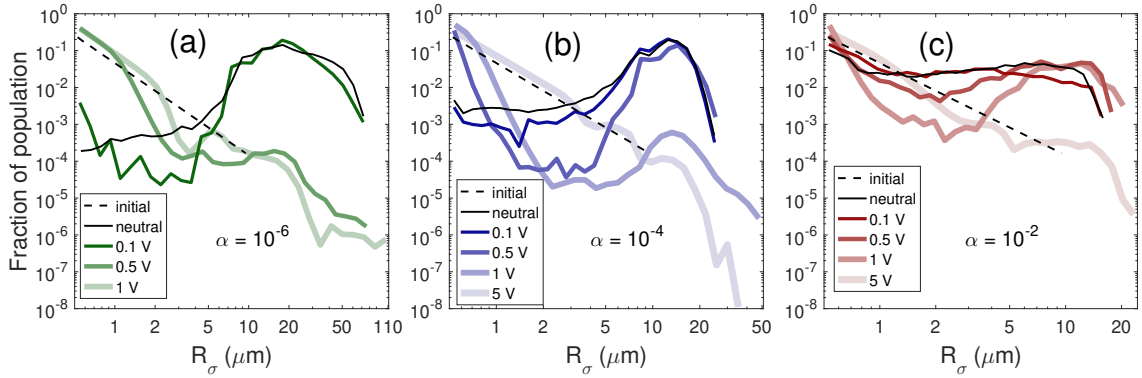

Figure 4.7: Size distribution of the population for charged (surface potential $|V_s| = 0$, 0.1, 0.5, 1, 5 V; in order of decreasing color shades) and neutral particles (darkest shades), at the end of the simulation (more than 5% of collisions result in bouncing). The black dashed lines indicate the distribution of initial population. Turbulence levels are $\alpha = 10^{-6}$ for a), $\alpha = 10^{-4}$ for b) and $\alpha = 10^{-2}$ for c).

The time evolution of the size distribution of the dust grains is shown in Figure 4.8. Over time, as the dust population evolves to larger grain sizes, the smallest grains in the population tend to be depleted [at the highest turbulence level (Fig. 4.8c), the small grains are depleted to a much smaller extent as aggregate growth does not progress very far before the bouncing criterion is met]. An exception occurs in the charged case with low turbulence (Fig. 4.8a): the relative velocities are not great enough for the smallest monomers to overcome the Coulomb repulsion barrier, and the aggregates grow primarily through the agglomeration of the mid-sized monomers. During the early stages of coagulation, the size of the aggregates in the charged populations lags behind that of the neutral populations, as most of the small particles repel each other, resulting in missed collisions (especially in weak turbulence; Figs. 4.8a, 4.8b). As aggregates grow larger, the growth of weakly charged particles in the relatively strong turbulence catches up with neutral population (Figs. 4.8b, 4.8c), caused by higher relative velocities between charged particles, resulting from their more compact structures. At the end of the simulation when the bouncing criterion is met, the charged population even has a greater percentage of the largest particles than the neutral population, for $\alpha = 10^{-2}$ (Fig. 4.8c). It is also shown that the large aggregates are a small fraction of the charged population for weak turbulence ($\alpha = 10^{-6}$; Fig. 4.8a), and a large fraction of the population for medium turbulence level ($\alpha = 10^{-4}$; Fig. 4.8b). For strong turbulence ($\alpha = 10^{-2}$; Fig. 4.8c), the population has relatively flat distribution of particles sizes.

The different growth modes of dust populations in different charging environments are further exhibited in Fig. 4.9. Fig. 4.9a shows the evolution of the size of the largest aggregates in a population compared to the size of the largest aggregates for a given turbulence level at the end of the simulation. In general, the maximum particle size reached at the end of the simulation increases as the charging level increases. In highly charged, weakly turbulent environments ($|V_s| = 5$ V, $\alpha = 10^{-4}$; $|V_s| = 1$ V,

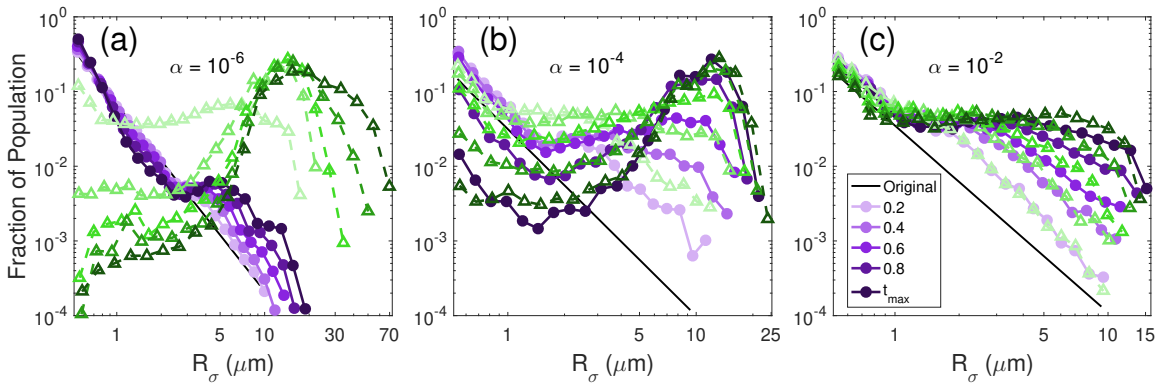

Figure 4.8: Evolution of distribution of particle size within total population for turbulence levels $\alpha = 10^{-6}$ (a), 10^{-4} (b), and 10^{-2} (c). The purple circles represent the charged case ($|V_s| = 0.1$ V) and green triangles represent the neutral case ($V_s = 0$). The curves progress in time from light to dark for equally spaced times until the bouncing criterion is met. The total elapsed times are 24.1 years for a), 3.2 years for b), and 0.4 years for c).

$\alpha = 10^{-6}$), once a critical size is reached, the largest particle in the population grows very rapidly (runaway growth), while the rest of the population grows very slowly, which is shown by the ratio of the maximum particle size to the average particle size of the population in Fig. 4.9b. In contrast, the ratio $R_{\sigma,max}/\langle R_\sigma \rangle$ decreases in strongly turbulent environments for $|V_s| < 1$ V, meaning that the difference in particle sizes of the populations decreases over time and the particles grow collectively. For the conditions between these two extreme cases, the ratio $R_{\sigma,max}/\langle R_\sigma \rangle$ first increases slightly and then decreases, indicating the preferential growth of large particles in the initial stage, followed by a more even growth among the population.

The elapsed time between successive interactions increases with time, due to the reduced number density of the dust. Particles in strongly turbulent regions collide more frequently and grow faster than those in weakly turbulent regions. Given the same turbulence level, weakly charged particles collide more frequently than highly charged particles. Although populations with low charge in strong turbulence grow faster, they meet the bouncing criterion sooner than those with high charge in weak turbulence, as shown in Table 4.1. The gentle collisions afforded by low relative velocities allow particles in weak turbulence to grow to larger sizes before meeting

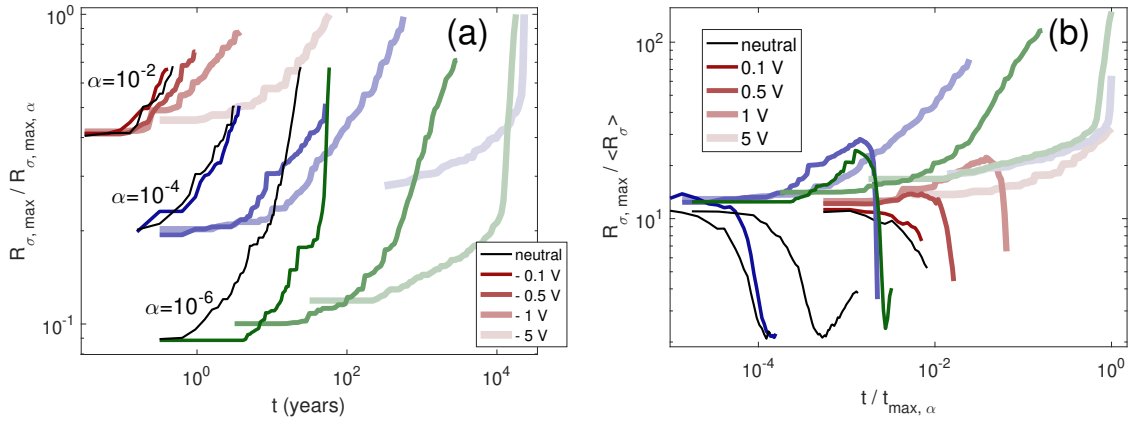

Figure 4.9: Growth rate of largest aggregate in the population. a) Normalized equivalent radius of the largest particle, and b) ratio of equivalent radius of the largest particle to the average equivalent radius of the population as a function of elapsed time for $|V_s| = 0$, 0.1, 0.5, 1, 5 V, in order of decreasing color shades, with different turbulence levels (red: $\alpha = 10^{-2}$; blue: $\alpha = 10^{-4}$; green: $\alpha = 10^{-6}$). For a), the equivalent radii are normalized by the largest value for each turbulence level: 19.5 μm for $\alpha = 10^{-2}$, 41.0 μm for $\alpha = 10^{-4}$, 115.6 μm for $\alpha = 10^{-6}$. For b), the elapsed times are normalized by the longest elapsed time for each turbulence level: 58 years for $\alpha = 10^{-2}$, 23148 years for $\alpha = 10^{-4}$, 17979 years for $\alpha = 10^{-6}$. The right end of each curve indicates the occurrence of bouncing for more than 5% of the particle interactions.

the bouncing criterion (compare results for neutral particles in Figs. 4.8a, 4.8c). In addition, particles with greater charge grow to a larger size before the bouncing criterion is met, due to reduced relative velocity by electrostatic repulsion (compare endpoints for Figs. 4.7, 4.9a). The maximum particle size reached before the bouncing criterion is met is positively correlated with charge for a given turbulence level, as shown in Figure 4.9a and Table 4.2.

Note that in addition to the relative velocity at impact, bouncing is also affected by the porosity. Compact aggregates are more likely to bounce than fluffy aggregates, because compact aggregates have much higher average coordination number, i.e., the number of contacts per monomer, than porous ones, making it more difficult to dissipate the collision energy through restructuring (Wada et al. 2011; Seizinger & Kley 2013). In addition, compact aggregates are less coupled to the gas, resulting in greater relative velocity with other particles, which also enhances bouncing. Therefore, charge can either reduce bouncing by decreasing the relative velocity through

electrostatic repulsion, or reinforce bouncing by increasing the compactness of aggregates. The first factor is more dominant for the environmental conditions considered in the simulation.

4.3 Analysis

The collision outcomes, i.e., the morphology of the resulting aggregates and the evolution of dust populations, depend on the properties of colliding particles, such as the relative velocity, equivalent radius and mass ratio. The particle properties also greatly determine the probability of particles being selected to collide and the probability of a successful collision, which further affect the collision outcome. In this section, we analyze the relationship between the colliding particles and the collision outcomes, and investigate how it is altered in different charging and turbulence conditions.

4.3.1 Relative Velocity

The relative velocity of aggregate pairs plays an important role in their collision rates as it affects the volume an aggregate sweeps out per unit time, which determines how likely it is for an aggregate to encounter another. The relative velocities between particles within the population during different time periods, calculated according to Eq. 2.89, are shown in Fig. 4.10. Similar-sized aggregates have low relative velocities. Aggregates with greater size differences, especially colliding pairs consisting of large and small aggregates, have higher relative velocities. The blanks that can be seen on the diagonal are due to the low relative velocity for aggregate pairs in that region resulting in a low selection probability, meaning they are less likely to be selected to collide (see Section 4.3.2). However, as more collisions take place, the difference of the relative velocity on the diagonal and the nearby regions decreases, especially for large particles (Figs. 4.10b, 4.10c), because the increased diversity of particle structure

(porosity) enables particles of the same size to have a variety of masses and therefore different friction times, resulting in a relatively high velocity.

Figures 4.10a and 4.10b show that the relative velocity drops as the equivalent radius just exceeds 10 μm, which is the maximum monomer size, because the spherically averaged density of an aggregate is much lower than it is for a spherical monomer of the same size (spherical monomers make up a large percentage of the particles at the early stage of the simulation). The decrease of the aggregate density in a PCA (particle-cluster-aggregation) collision results in a smaller difference in the friction times for an aggregate and a monomer, decreasing their relative velocity calculated from Eq. 2.89. Figures 4.10b and 4.10c show that the regions of maximum relative velocity (indicated by black rectangles; note that they are local maxima) shift towards smaller particle size as more collisions take place. The reason is that the maximum monomer size of the population decreases over time with the depletion of large monomers, and meanwhile the increase of the ratio of small aggregates to monomers of the same size leads to an overall decreased density for small particles. The resulting stronger coupling with the gas increases their relative velocity with respect to relatively large particles (notice that this is still in the small particle regime). Therefore, particles with 5 $\mu m < R_\sigma < 7$ μm have higher relative velocities in Figure 4.10c (indicated by the black rectangle) than in Figures 4.10a and 4.10b. Unlike the neutral particles, the relative velocity of charged particles increases with increasing size difference (Figs. 4.10e, 4.10f), except for the initial stage (Fig. 4.10d).

As discussed in section 4.2.3, charged particles have greater initial relative velocities than neutral particles (not considering the reduction of the velocity due to repulsion), because they are less coupled to the gas due to more compact structure. Figure 4.11 shows that the initial relative velocity is positively correlated with the dust surface potential for the same turbulence level. The fact that particles with the highest charge have the greatest compactness factors (Figure 4.6) and largest initial

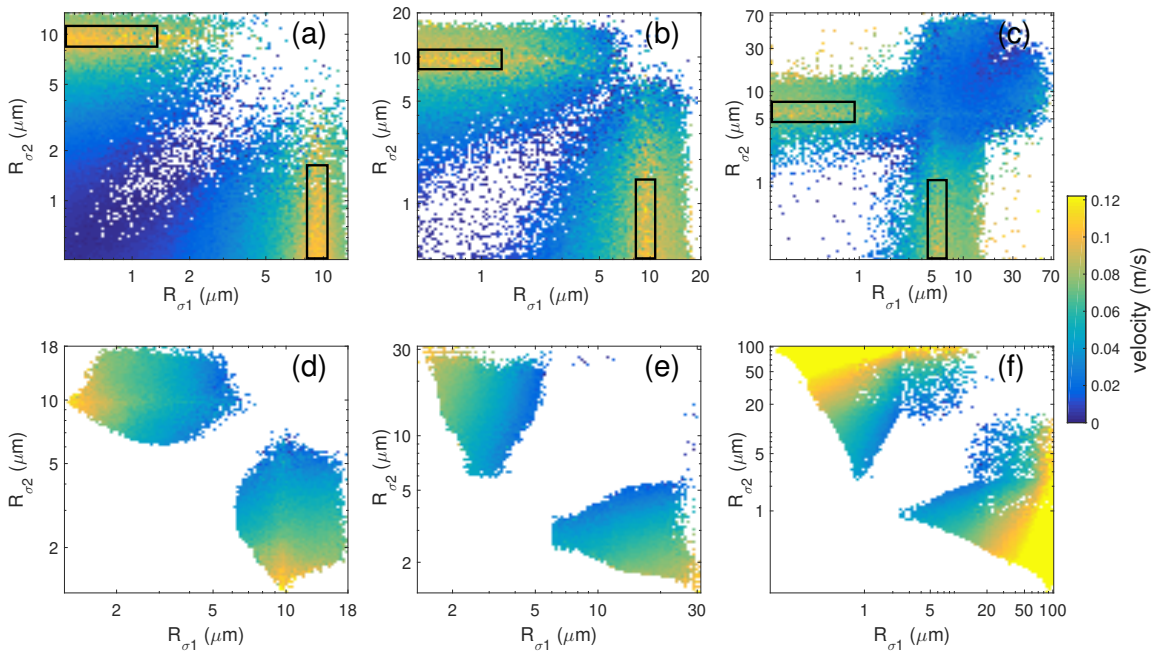

Figure 4.10: Relative velocity for particles at different stages of growth, a, d) 0-40,000 successful collisions, b, e) 40,000-80,000 successful collisions, and c, f) 80,000-140,000 successful collisions, comparing neutral (top row) and charged (bottom row, $|V_s| = 1$ V) grains. The turbulence level is $\alpha = 10^{-6}$.

relative velocities (Figure 4.11) corroborates the importance of the porosity in the dust motion.

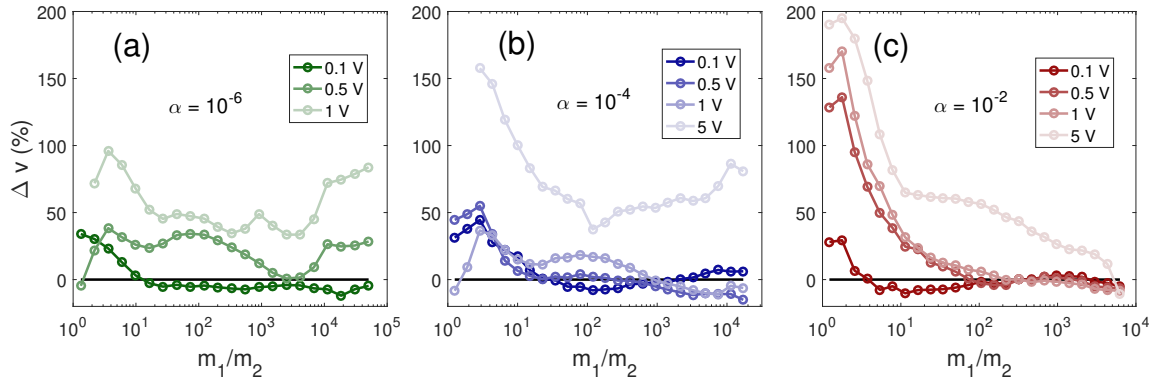

Figure 4.11: Percent difference of relative velocity between colliding pairs for charged aggregates relative to neutral aggregates as a function of the mass ratio. Color shades indicate dust surface potential. Turbulence levels are $\alpha = 10^{-6}$ for a), $\alpha = 10^{-4}$ for b) and $\alpha = 10^{-2}$ for c).

4.3.2 Selection Rate

The collision kernel which determines the selection of potentially colliding pair is a function of the effective cross section, which depends on particle size and charge, and the relative velocity, which depends on size, and indirectly on charge through the porosity. As a large size difference between grains increases the relative velocity, but large particles are a small fraction of the original population, the selection rate is a function of size, charge, relative velocity and the distribution of size in population. The dominant factor varies for different size ranges and different stages of coagulation, as shown in Figure 4.12, comparing the selection rates for a neutral ($|V_s| = 0$) and highly charged environment ($|V_s| = 1$ V) with turbulence level $\alpha = 10^{-6}$. In the neutral environment (top row of Fig. 4.12), the initial selection rate is broadly distributed over all particle sizes, though small monomers are most likely to be selected for collisions, reflecting the abundance of small monomers within the population (Fig. 4.12a). Particles first grow by collisions between monomers of all sizes, followed by PCA and CCA (cluster-cluster-aggregation). The maximum selection rate slowly shifts towards larger particle sizes as small monomers and aggregates are gradually removed from the population, and CCA is the dominant mechanism at the late stage of the process. In contrast, in the highly charged environment (bottom row of Fig. 4.12), small monomers are not selected to collide at the initial stage of the growth process (Fig. 4.12d), and particles first grow by coagulation of relatively large monomers, and then by accretion of monomers onto large aggregates. The mean size of accreted monomers shifts towards smaller sizes as time goes on, as larger aggregates enable small particles to overcome the electrostatic barrier (Figs. 4.12e, 4.12f). The selection rate remains sharply peaked for combinations of large aggregates (R_σ greater than maximum monomer size) with smaller monomers, an indication that PCA is the dominant mechanism over all time (Figs. 4.12e, 4.12f). The difference in the selection rates contributes to more spherical and symmetric structures of the charged

aggregates relative to the neutral aggregates (Fig. 4.2), as particles growing through PCA accrete monomers more evenly than collisions between irregular aggregates.

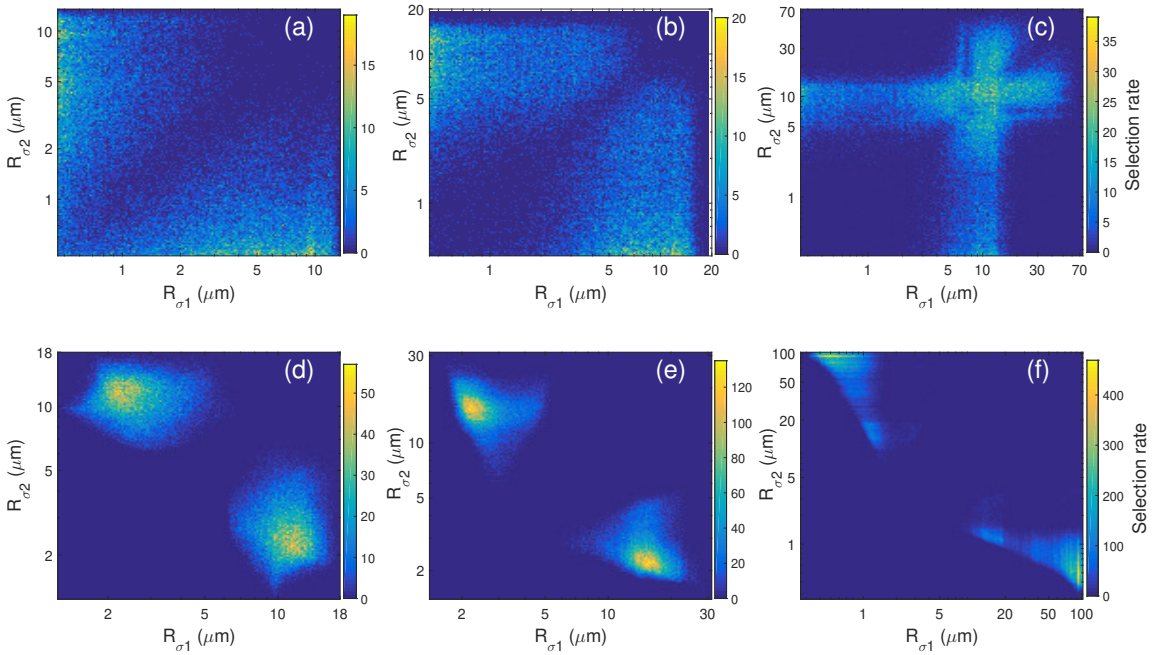

Figure 4.12: Selection rate for particles at different stages of growth, a, d) 0-40,000 successful collisions, b, e) 40,000-80,000 successful collisions, and c, f) 80,000-140,000 successful collisions, comparing neutral (top row) and charged (bottom row, $|V_s| = 1$ V) grains. The turbulence level is $\alpha = 10^{-6}$.

4.3.3 Size Ratio of Colliding Partners

The size ratio of colliding particles is greatly affected by the charging condition, turbulence level and size distribution within the population. In turn, it affects the collision outcome and the structure of the resulting aggregates. In general, the size of colliding particles increases over time for neutral or weakly charged population, while the smaller particle of the colliding pair decreases over time for highly charged, weakly turbulent population, since larger particles are more capable of accreting small particles. Figure 4.13 shows the equivalent radii of resulting particle as a function of the size ratio of colliding particles. It is seen that the equivalent radius of the resulting particle is positively related to the dust surface potential for a given size ratio of colliding particles, because in general, the smaller particle of the colliding

pair is larger in a highly charged environment, due to the repulsion of small particles. Therefore, the same size ratio corresponds to two larger colliding particles in a highly charged environment than in neutral or weakly charged environments, and results in a larger aggregate. Note that the slopes of the curves are nearly constant for neutral and weakly charged populations, but for highly charged populations the curves rise rapidly and then tend to be a constant value. The flattening of the curves is probably caused by the runaway growth, i.e., accretion of small particles onto large particles, which does not make much change to the sizes of large particles. In addition, the sizes of the small particles being accreted decrease over time, causing a rapid increase in the size ratios while the sizes of resulting aggregates are relatively constant.

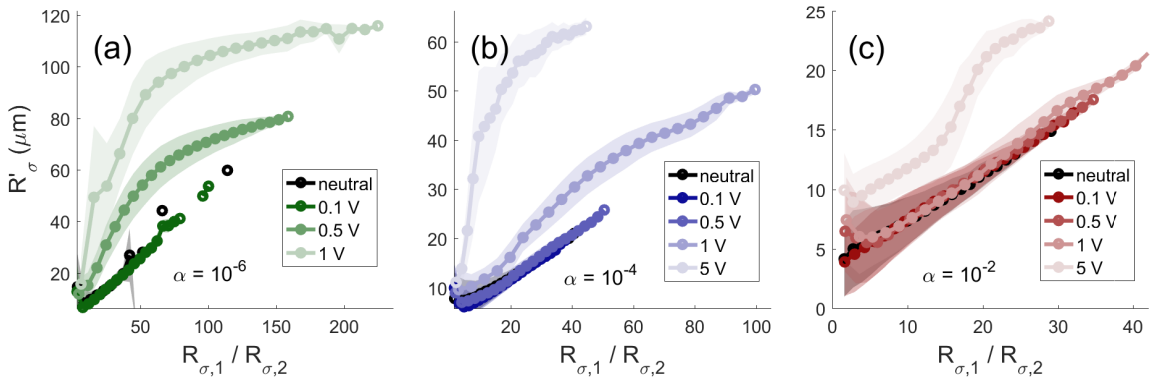

Figure 4.13: Average equivalent radius of the resulting particle from successful collision as a function of ratio of equivalent radii of colliding particles, for different turbulence levels and dust surface potentials. The shaded areas indicate one standard deviation of the average R_σ ratio. Turbulence levels are $\alpha = 10^{-6}$ for a), $\alpha = 10^{-4}$ for b) and $\alpha = 10^{-2}$ for c).

4.4 Discussion

As shown, the process of dust coagulation is affected by many factors, i.e., the diversity of particle size, porosity, charge, and turbulence. These factors influence each other and come together to determine the collision process. However, most studies to date have considered only a subset of these factors, and thus do not reflect the diversity of dust particles in a real environment. The current model incorporates all of these factors to examine how the charge affects the collision kernel of particles

and their resultant porosity, which further influences the collision probabilities and the growth rate of dust population.

In this section, we compare our detailed-MC model to previous MC models for neutral particles with an initial monodisperse distribution (Section 4.4.1), in particular determining the effect of charged aggregates (Section 4.4.2).

4.4.1 Comparison with Previous MC Models

The key characteristic of dust particles that controls their coupling to the turbulent motion of the gas is the ratio of surface area to mass A/m. In the "hit-and stick" regime, the mass m and the cross-section A for growing aggregates follows a power-law relationship (Ormel et at. 2007),

$$A \propto m^{\delta}, \quad \frac{2}{3} \leqslant \delta \leqslant 1 \tag{4.1}$$

with the lower limit $\delta = \frac{2}{3}$ corresponding to compact spherical particles, and the upper limit $\delta = 1$ corresponding to the aggregation of chains or linear structures. Consequently, the friction time scales with mass as

$$\tau_f \propto m^{1-\delta}. \tag{4.2}$$

Ormel et al. (2007) defined an enlargement factor $\psi = \frac{V}{V^*}$, where V is the extended volume corresponding to a sphere with a radius equal to the equivalent radius, and V^* is the volume the material occupies in its compacted state [the enlargement factor is approximately equal to the inverse of the compactness factor, except that V^* in the compactness factor is equal to the total volume of all the monomers in an aggregate, which is smaller than the V^* in the enlargement factor]. By using the relationships $V \propto A^{\frac{3}{2}} \propto m^{\frac{3}{2}\delta}$ and $V^* \propto m$, the enlargement factor can be related to the mass as (Ormel et al. 2007)

$$\psi \propto m^{\frac{3}{2}\delta - 1}. \tag{4.3}$$

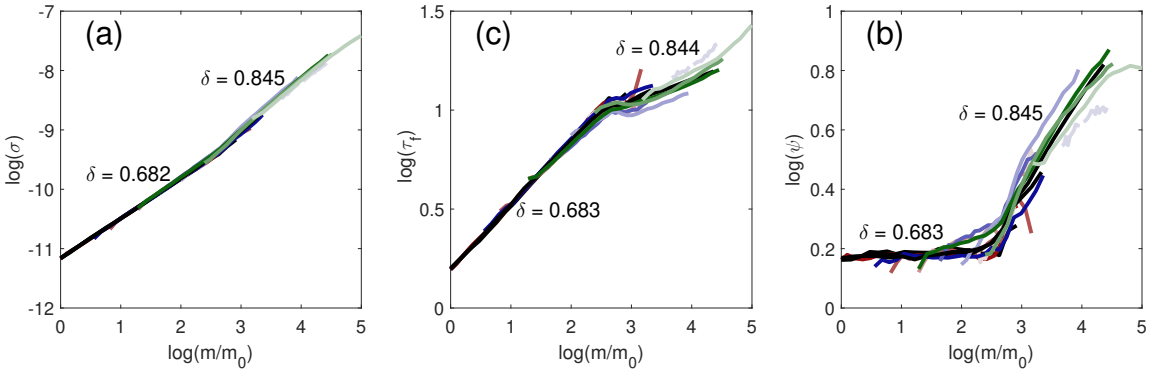

Figure 4.14: a) Surface area, b) friction time and c) enlargement factor as a function of mass for neutral and charged particles (surface potential $|V_s| = 0$, 0.1, 0.5, 1, 5 V; in order of decreasing color shades) with more than two monomers, for different turbulence levels (red: $\alpha = 10^{-2}$; blue: $\alpha = 10^{-4}$; green: $\alpha = 10^{-6}$). The masses are normalized by the mean mass of the initial population.

For compact particles ($A \propto m^{2/3}$), the friction time $\tau_f \propto m^{1/3}$, which increases monotonically with mass, and the enlargement factor ψ is constant. On the other hand, for fluffy particles ($\delta > \frac{2}{3}$), both τ_f and ψ increase with m. In the extreme case where linear aggregates are formed by collisions between equal-sized monomers, δ takes the value 1, and τ_f stays constant, which means the relative velocity between particles stays the same during collisional growth, where $\psi \propto m^{1/2}$.

Figure 4.14 shows the surface area, friction time and enlargement factor as a function of mass for aggregates generated in our simulation. By comparing the slopes of the curves with Eqs. 4.1, 4.2 and 4.3, one obtains $\delta \sim 0.682$ before the turning point and $\delta \sim 0.845$ after the turning point from the relationship between A and m (Fig. 4.14a); $\delta \sim 0.683$ before the turning point and $\delta \sim 0.844$ after the turning point from the relationship between τ_f and m (Fig. 4.14b); and $\delta \sim 0.683$ before the turning point and $\delta \sim 0.845$ after the turning point from the relationship between ψ and m (Fig. 4.14c). The turning point corresponds to the maximum monomer mass. The increase of δ at the turning point indicates that aggregates with higher porosity have larger δ.

Ormel et al. (2007) replaced the mass in Equation 4.3 with the volume of the particles in order to take into account the spatial extent of the collision partners, which reflects the porosity, and, by using the relationship among the volume, cross-section as well as the enlargement factor, derived a formula for the enlargement factor of the resulting aggregate for collisions between particles of all kinds of sizes:

$$\psi = \langle\psi\rangle_m \left(1 + \frac{m_2\psi_2}{m_1\psi_1}\right)^{\frac{3}{2}\delta_{CCA}-1} + \psi_{add} \tag{4.4}$$

where δ_{CCA}=0.95, and $\psi_{add} = B\frac{m_2}{m_1}\psi_1 exp\,[-\mu/m_F]$ with $B = 1$, $m_F = 10m_0$ (m_0 is the monomer size for monodisperse distribution). ψ_{add} is a term added to compensate for the underestimation of the porous growth when one of the colliding particles is very small.

Because our detailed-MC model and Ormel's MC model have different initial populations (polydisperse vs monodisperse) and locations within the PPD, instead of comparing the results of the two models directly, it is more instructive to compare the results of the detailed-MC model to the results calculated by the formula for Ormel's MC model (Eq. 4.4) using the data of the colliding particles in the detailed-MC model. Fig. 4.15 shows that in low turbulence ($\alpha = 10^{-6}$, 10^{-4}; Figs. 4.15a, b), the results of the two models start off the same, and then diverge in the neutral cases, while being consistent in the charged cases. In strong turbulence ($\alpha = 10^{-2}$; Fig. 4.15c), the results of the two models tend to diverge in both charged and neutral cases, with more divergence in the neutral case. Ormel's MC model predicts that charged and neutral populations have very similar enlargement factor for $\alpha = 10^{-2}$, while the detailed-MC model shows a difference with larger enlargement factor for the charged case. Greater differences between charged and neutral populations occur for $\alpha = 10^{-6}$, 10^{-4}, but the effect is opposite: the enlargement factor of charged population is smaller than that of the neutral population for $\alpha = 10^{-6}$, and is larger for $\alpha = 10^{-4}$. For all turbulence levels, the detailed-MC model results in more compact aggregates than

Ormel's MC model for equal ratio of mass-weighted enlargement factors of colliding particles, although V^* in the detailed-MC model is smaller than that of MC model, which would cause a larger enlargement factor. One possible reason is that Eq. 4.4 is based on a monodisperse distribution, while the polydisperse distribution in the detailed-MC model leads to more efficient packing than a monodisperse distribution, i.e., the small particles fill in the gaps of aggregates. However, in the charged cases with low turbulence ($\alpha = 10^{-6}$, 10^{-4}), the two models have similar enlargement factors, because the charged population have a narrower range of monomer sizes, i.e., less diversity of monomer size, which is closer to a monodisperse distribution than the size distribution in the neutral case.

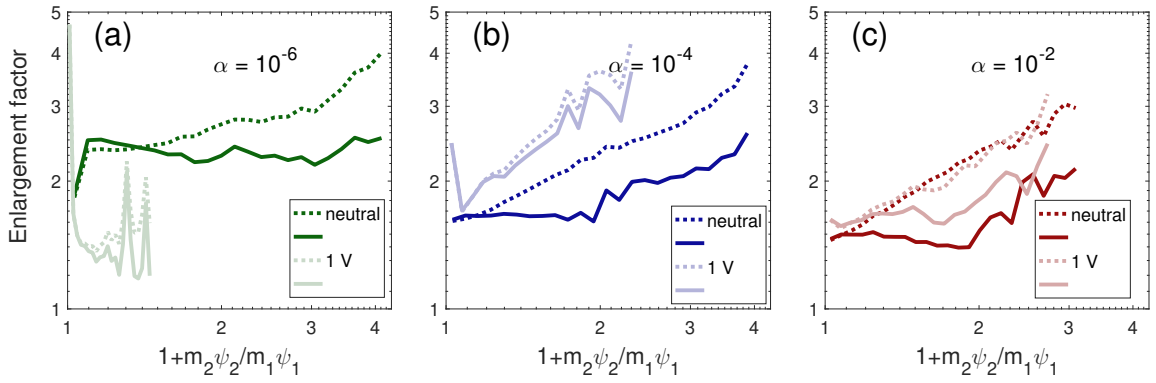

Figure 4.15: Comparison of the results from detailed-MC model (solid lines) to the results calculated by Ormel's MC model (dotted lines), for neutral (dark shades) and charged (light shades) particles. Turbulence levels are $\alpha = 10^{-6}$ for a), $\alpha = 10^{-4}$ for b) and $\alpha = 10^{-2}$ for c).

4.4.2 Comparison of Growth of Charged Aggregates

The diversity of particle sizes not only increases the growth rate of particles (due to the higher relative velocity between grains within the population), but also reduces the porosity of aggregates (more efficient packing; Fig. 4.15), which further increases the growth rate due to the weak coupling of compact particles to the gas. For charged particles, in addition to these two effects, the size distribution also helps avoiding the freeze-out of the fractal growth.

Okuzumi (2009) simulated dust coagulation with an initial monodisperse population in various plasma conditions. In contrast to Ormel et al. (2007), this simulation assumed that the dust grows into an ensemble of quasi-monodisperse aggregates with fractal dimension $D \sim 2$ and typical monomer number N, which increases during the fractal growth of dust. He found that the electric repulsion between charged particles strongly inhibits dust growth, which eventually ceases, for a wide range of model parameters. For example, at a radial distance of 5 AU and scale height z = H, with initial monomers size $a_0 = 0.1\ \mu m$, the dust growth freezes out at $N \sim 33$ for turbulence strengths $\alpha = 10^{-3}, 10^{-4}$. However, for $\alpha = 10^{-2}$, the dust continues growing and reaches the subsequent growth stage involving collisional compaction.

Figure 4.16 shows the average ratio of electric potential energy PE to kinetic energy KE of particles with N monomers in our simulations. Although the average ratio of potential energy to kinetic energy is larger than 1 for highly charged cases, the standard deviation of PE/KE for the population shows that there is a significant fraction of the population with $PE/KE < 1$, preventing the freezing of particle growth. Okuzumi (2009) proposed a possible scenario to remove the electrostatic barrier against the fractal growth, which assumes a polydisperse size distribution where large aggregates can sweep up small aggregates. This is borne out in the results from the detailed-MC model, as the aggregates can develop sufficient relative velocity to overcome the electrostatic barrier when colliding with large particles. Okuzumi (2009) also pointed out that this can not happen if the large aggregates are as fluffy as the small aggregates (with comparable mass-to-surface-area-ratios). Therefore, the diversity of both the porosity and size of particles is important to overcoming the growth barrier.

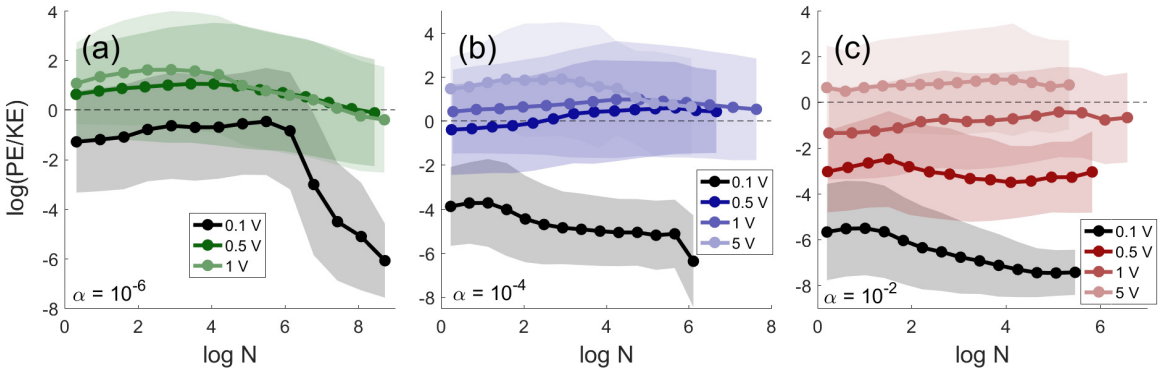

Figure 4.16: Ratio of electric potential energy to kinetic energy of particles as a function of the number of monomers within aggregates. Turbulence levels are $\alpha = 10^{-6}$ for a), $\alpha = 10^{-4}$ for b) and $\alpha = 10^{-2}$ for c). The shaded areas indicate the standard deviation of the ratio.

4.5 Conclusions

We have presented a model of grain growth that incorporates the detailed physical characteristics of aggregates during the collision process employing a MC algorithm to model the collisional evolution of a population of dust particles in a protoplanetary disk. We defined two quantities, the compactness factor and the equivalent radius, to describe the porosity of an aggregate and quantify the effect of the collision process on the structure of the colliding aggregates. We compared charged and neutral aggregates for different levels of turbulence, which drives collisions. Our main findings are:

1. Highly charged aggregates contain fewer small monomers, resulting in a size distribution shifted towards larger monomer sizes and greater average monomer size; this shift increases with larger surface potential and lower turbulence (Fig. 4.3). The average monomer size within aggregates does not change much over time in strongly turbulent environments for $|V_s| < 1$ V, and decreases over time in weakly turbulent environments with $|V_s| > 0.5$ V.

2. In general, charged aggregates are more compact than are neutral aggregates, and highly charged aggregates tend to be more compact than those having lower charge for the same turbulence level (Fig. 4.6). One reason is that charged particles

tend to avoid the prominent region of the colliding partners due to the high local potential, and are more likely to stick between the extended arms. This effect is most noticeable for weakly turbulent and/or highly charged environments, in which the particles have sufficient time to deviate/rotate to minimize the potential energy of the configuration due to the slow movement. A second reason is that aggregates grow mainly through PCA in highly charged, weakly turbulent environments, i.e., by accretion of monomers onto large aggregates. It is easier for monomers to pass through the pores and fill in the gaps of aggregates, reducing the porosity.

3. Aggregate growth in the charged population first lags behind neutral populations due to electrostatic repulsion. As particles grow larger, the growth of weakly charged particles in relatively strong turbulence catches up with neutral particles (Fig. 4.8), due to the greater number density (more particles remain in the population due to repulsion) and higher relative velocities between charged particles (resulting from their more compact structures).

4. Particles in strongly turbulent regions collide more frequently than those in weakly turbulent regions. Given the same turbulence level, weakly charged particles grow faster than highly charged particles (Table 4.1). However, highly charged particles grow to larger size before reaching the bouncing barrier, due to reduced relative velocity by electrostatic repulsion. The maximum particle size reached before the bouncing criterion is met is positively correlated with charge for a given turbulence level (Fig. 4.9a and Table 4.2).

5. For a highly charged environment with low turbulence, once a critical size is reached, the largest particles in the population grow very rapidly (runaway growth), while the rest of the population grows very slowly (Fig. 4.9). The particles formed by runaway growth are a small proportion of the population, resulting in a population with a few large aggregates and a lot of remaining monomers and small aggregates. For populations without runaway growth, particles grow collectively, and almost all

monomers have collided and formed aggregates before the bouncing criterion is met (Fig. 4.7).

6. Charge has a greater impact on the porosity, monomer size, collision probability and the growth rate of dust particles in weak turbulence than in strong turbulence.

7. Diversity of particle size not only increases the growth rate of the particles (due to the higher relative velocity), but also reduces the porosity of the aggregates (more efficient packing; Fig. 4.15), which further increases the growth rate due to the weak coupling of compact particles to the gas. For charged particles, the diversity of both the porosity and size are important to overcoming the growth barrier (Fig. 4.16).

In conclusion, it has been shown that charge and porosity play an important role in the evolution of a dust population. Charge decreases the growth rate of dust particles, due to missed collisions and smaller capture cross section (more compact structure). The longer growth timescale causes particles to be more subject to the radial drift barrier, and particles may have been accreted to the central star before growing to large sizes (Birnstiel 2016). In addition, dust particles also encounter bouncing and fragmentation barriers during their growth. The threshold bouncing and fragmentation velocities depend on impact energy, material, monomer size and porosity. Compact aggregates are more likely to bounce/fragment than fluffy aggregates, and aggregates comprised of small monomers are more resistant to fragmentation/compaction. Particles in charged environments are overall more compact and are comprised of larger monomers, which makes them more susceptible to bouncing and fragmentation. On the other hand, although charge increases the initial relative velocity between particles, due to the weaker coupling to the gas, the velocity is reduced during the electrostatic interaction, which decreases bouncing/fragmentation. On top of these two factors, the collision in charged cases tends to occur

between a large particle and a small particle, which is unlikely to cause catastrophic fragmentation. Instead, mass transfer is more likely: when a small particle impacts a large aggregate, part of its mass is transferred to the target, leading to further growth of large particles. Therefore, charge may assist the population to overcome the fragmentation barrier. In addition to the impact on the growth barriers, the charge also greatly affects the optical properties of dust, such as the scattering and absorption opacity, by altering particle porosity/composition and the abundance of remaining small particles, which influences the temperature distribution, spectral energy distribution and appearance of PPDs (Kirchschlager & Wolf 2014; Krijt et al. 2015).

A linear regression and principal component analysis were used to determine that the charge, compactness factor, equivalent radius and relative velocity are the greatest contributors to the collision rate and the properties of the resulting aggregates in the hit-and-stick regime. The next step of this research is to include other types of collision outcomes in the simulation, such as bouncing, fragmentation, erosion and mass transfer, and develop a heuristic model for the collision rate as well as the physical characteristics of the resulting aggregate based on the data recorded from actual collisions. This new kernel will be used to simulate the evolution of a dust population over long time periods relevant to protoplanetary disk evolution.

Acknowledgments: Support from the National Science Foundation grant PHY-1707215 is gratefully acknowledged.

CHAPTER FIVE

The Initial Structure of Chondrule Dust Rims I: Electrically Neutral Grains

This chapter published as [200]: Chuchu Xiang, Augusto Carballido, Romy D. Hanna, Lorin S. Matthews, Truell W. Hyde, "The initial structure of chondrule dust rims I: Electrically neutral grains," Icarus 321, 99-111 (2019).

5.1 Introduction

The origin of FGRs has been somewhat disputed, with some researchers proposing that FGRs formed in the parent body environment, either by attachment and compaction of dust onto chondrules in regolith (Sears et al. 1993, Trigo-Rodriguez et al. 2006, Takayama & Tomeoka 2012), or through pervasive aqueous alteration of chondrules (Sears et al. 1993, Takayama & Tomeoka 2012). These theories are supported by the embayment textures along the chondrule/rim boundary (Takayama & Tomeoka 2012) and the low rim porosity which is inconsistent with the high-porosity structure formed in experimental simulations of preplanetary dust coagulation (Blum & Wurm 2000, Blum & Schräpler 2004). However, Beitz et al. (2013) performed experiments of impacts between chondrule analogs and different dust materials, and found larger dust rim porosities than those found in chondrites. Thus, Beitz et al. (2013) concluded that FGRs around chondrules can not form in dynamic compaction processes.

Several lines of evidence suggest that FGRs formed by accretion of grains onto the underlying chondrule cores in a nebular setting, before the rimmed chondrules were incorporated into their parent bodies (Metzler et al. 1992, Morfill et al. 1998, Brearley 1999). The presence of pre-solar grains in CR chondrite FGRs led Leitner et al. (2016) to conclude that those rims had a nebular origin, since pre-solar silicate and oxide abundances in the rims differ from those in the interchondrule matrix, indicating different alteration paths of both meteoritic components. Metzler (2004)

investigated the occurrence and properties of preirradiated (track-rich) olivines in CM chondrites, and found that track-rich olivines were only contained in the clastic matrix. The absence of track-rich olivines in fragments of primary rock implied its formation in an environment shielded from cosmic radiation, leading Metzler to argue a nebular origin of dust mantles around chondrules in CM chondrites (Metzler 2004). Bland et al. (2011) mapped the orientation of submicron grains in the Allende CV chondrite, and calculated an initial rim porosity of 70-80% by relating fabric intensity to net compression. Such high porosity values are similar to those obtained from Monte Carlo simulations (Ormel et al. 2008) and laboratory experiments (Beitz et al. 2013), which assume nebular conditions. Metzler et al. (1992) found a roughly linear correlation between the thickness of dust rims and the diameter of the mantled cores, using optical microscopy and scanning electron microscopy. This finding is supported by numerical simulations assuming a nebula origin (Ormel et al. 2008; Carballido 2011), and furthered by Hanna and Ketcham (2018), who, using X-ray computed tomography, examined the 3D morphology of FGRs in the CM chondrite Murchison, and found a power law relation between FGR volume and chondrule radius, consistent with rim accretion in a weakly turbulent solar nebula as calculated by Cuzzi (2004). In addition, the noticeably smaller size of grain in FGRs than in enveloping matrix (Ashworth 1977; Brearley 1993; Zolensky et al. 1993), the alteration of hydrous phases present in the rims prior to accretion onto chondrule surface suggested by petrographic evidence (Metzler et al. 1992), and the rim layering as well as the grain-size coarsening (Brearley et al. 1999) all support the nebular setting of FGR formation.

The significance of a nebular scenario for FGR formation cannot be overstated. A possible path towards the emergence of asteroidal parent bodies, composed of agglomerates of rimmed chondrules, could involve an essentially hydrodynamic process: the runaway convergence of chondrules due to the relative drift between the solar

nebula gas and small solids (Carrera et al. 2015). This streaming instability, as it is known, has its origin in the radial pressure gradient that supports the nebular gas, but not the solid component. If chondrules acquired dust envelopes while being suspended in the solar nebula, the resulting rimmed chondrules could have formed dense clumps due to the streaming instability. These clumps, in turn, would have facilitated low-velocity sticking between rimmed chondrules.

Here we adopt the nebular scenario for FGR formation, and assume that FGR accretion occurs in the midplane of a minimum-mass solar nebula (MMSN; Hayashi 1981). Although different chondrule groups are thought to have formed at different heliocentric distances (Wasson & Wetherill 1979; Wasson 1988), Rubin (2010) suggested that most groups formed within 3 AU, based on the chemical composition of different groups. Salmeron et al. (2012) also suggested a radial distance of 1-3 AU for chondrule formation based on a possible heating mechanism to melt the chondrule core and subsequently collect a cool dust rim. For this study, we choose 1 AU as the heliocentric distance as a representative location for which FGR accretion takes place.

As discussed in Section 3.3.2, the study is restricted to a small patch on the chondrule surface. A "detailed-MC" model is developed to simulate collisions between dust and chondrules, taking into consideration detailed collisional physics, such as the trajectory of the incoming particle, restructuring after the collision, and the resulting morphology of the dust rim. The effects of turbulence strength and chondrule size on rim growth are investigated by tracking the evolution of the dust accretion process and examining the structure of the resulting dust rim (or more precisely, *partial* rim). In addition, the difference between rims formed by accretion of dust monomers (particle aggregation) and rims formed by accretion of dust aggregates (cluster aggregation) is analyzed. All theoretical models of chondrule rim growth have assumed that the dust grains comprising the rims are electrically neutral. We follow that assumption

in this chapter, and study the effects of electric charge on the formation of FGRs in next chapter.

5.2 Results

In order to analyze the structure and composition of a dust rim, we divided the rim into 30 horizontal layers (i.e., parallel to the chondrule's surface), with each layer having the same thickness. We define the porosity of each layer as the ratio of the volume of voids within the layer, which is the total volume of the layer minus the sum of the volume of the monomers (or monomer portions) within that layer, to the total volume of the layer. To avoid edge effects of the dust pile, only the inner region of the pile with a radius of 50% of the total pile radius (i.e., the distance from the pile center to pile edge) is analyzed.

5.2.1 Effect of Turbulence Strength

Figure 5.1 shows dust piles on the surface of a chondrule with a radius of 700 μm, for runs a1-r7 (Fig. 5.1a) and a6-r7 (Fig. 5.1b). The piles are formed on circular patches of 100 μm in diameter. The respective turbulent strengths are $\alpha = 10^{-1}$ and 10^{-6}. The piles contain 30,000 monomers. Since the relative speeds between chondrules and dust particles are higher in regions of stronger turbulence, massive particles are more likely to cause restructuring, as they have a larger kinetic energy which can exceed the threshold rolling energy. Therefore, chondrule dust rims formed in environments with stronger turbulence are more compact than those formed in weak turbulence. This can be better appreciated in Fig. 5.1c and Fig. 5.1d, which show a vertical slice through the center of the dust pile of Figs. 5.1a and 5.1b, respectively. There are more open spaces between monomers in the weak-turbulence case (Fig. 5.1d), a sign of less compaction (note that monomers and groups of monomers that are apparently detached from the main pile in Figs. 5.1c and 5.1d

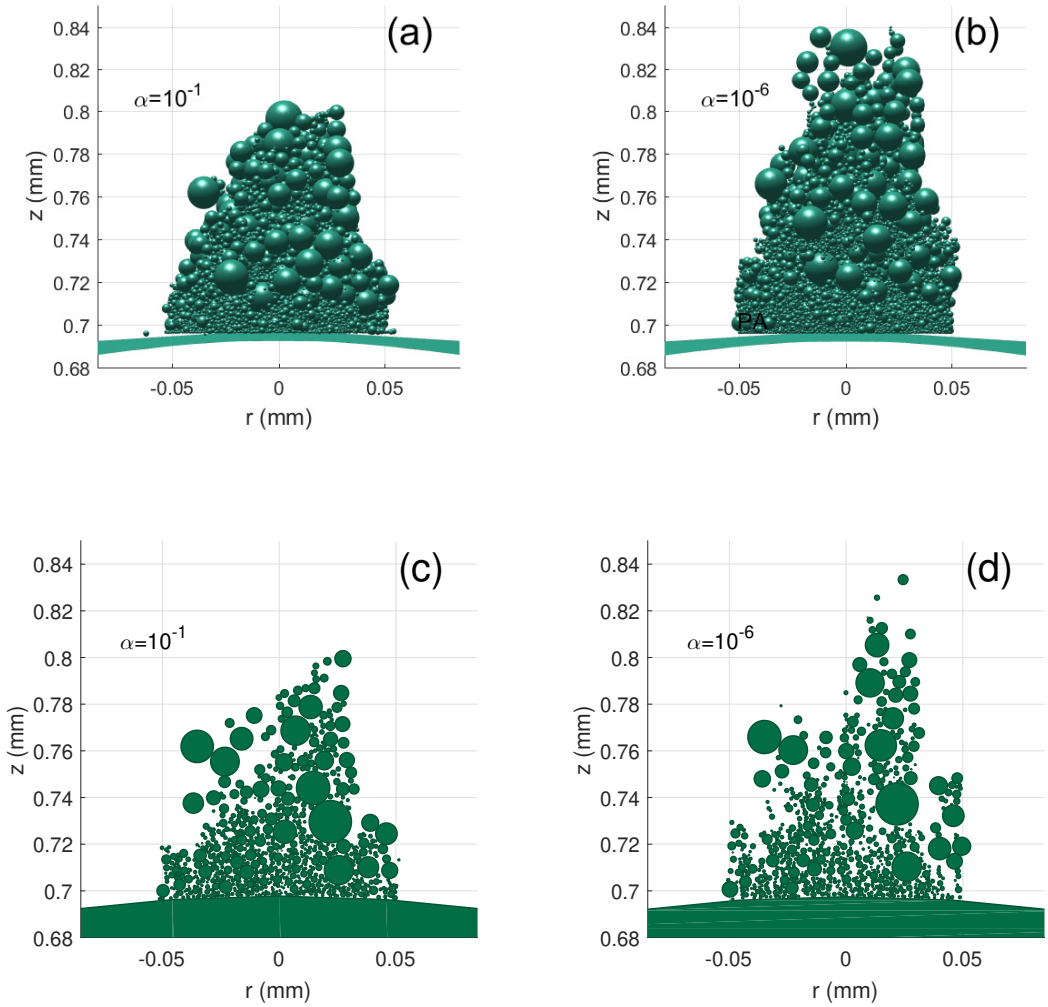

Figure 5.1: Rim growth on a 100 μm-diameter patch on the surface of a chondrule with a radius of 700 μm, from runs a1-r7 (a,c) and a6-r7 (b,d). The elapsed times are 0.26 yr and 173.61 yr, respectively. Panels (c) and (d) show the monomer distributions on a vertical plane cutting through the center of the dust piles that are shown in (a) and (b), respectively. The dust particle sizes shown (circle diameters) represent the apparent monomer sizes due to cutting effects. More compaction (less open spaces) is observed in the strong-turbulence case (c). The apparent detachment of some monomers and groups of monomers from the main dust pile is due to the slicing procedure, which cuts off other monomer structures that support the "detached" ones. A movie showing a succession of slices through the dust rim from the left to the right is available online.

appear to be so due to the slicing procedure, which cuts off other monomer structures on which the "detached" structures are supported).

Figure 5.2 shows the rim porosity as a function of distance from the chondrule surface, for different turbulence strengths. Note that the porosity increases rapidly at a certain radial distance in the dust pile. Thus we define the rim thickness by the position of the "knee" in the porosity plot. The rims formed in weak turbulence ($\alpha = 10^{-4}$) are more porous than those formed in strong turbulence ($\alpha = 10^{-1}$) after accretion of 60,000 monomers. Strong turbulence results in a more compact rim, and restructuring leads to an approximately constant porosity of 55% throughout the thickness of the rim. Weak turbulence produces less restructuring, resulting in rims which are overall more porous, and the porosity increases from the base of the rim to the top, as very fine dust particles are able to pass through voids and fill in the lower rim layers. Analysis of chondrules with radii between 500 and 1000 μm shows that FGRs formed in weak turbulence ($\alpha \leq 10^{-4}$) have an average porosity of 60-74%, while those formed in strong turbulence ($\alpha = 10^{-1}$) have an average porosity of 52-60%, with the lower end of each range corresponding to large chondrules and the upper end to small chondrules. In general, the porosity of FGRs decreases with both turbulence (stronger dependence) and chondrule radius (weaker dependence). The effect of chondrule size will be further discussed in Section 5.2.2.

In addition to the enhanced restructuring, the increased relative velocity caused by stronger turbulence also leads to more frequent collisions between the chondrule and the dust particles, speeding up the growth of the dust rim. Figure 5.3a displays the time necessary to build rims of three different thicknesses on a chondrule of 500 μm in radius, in each of the six turbulence conditions that we consider. The lower bound of each vertical bar represents a rim thickness of 40 μm, while the upper bound corresponds to a thickness of 320 μm. The midpoints represent a thickness of 180 μm. The time required to build rims of 180 μm in thickness is 2.7-3.2$\times 10^{-2}$ yrs for

$\alpha = 10^{-1}$; 7.9-8.9$\times 10^{-2}$ yrs for $\alpha = 10^{-2}$; 2.4-4.6$\times 10^{-1}$ yrs for $\alpha = 10^{-3}$; 1.3-2.4 yrs for $\alpha = 10^{-4}$; 7.6-14 yrs for $\alpha = 10^{-5}$; and 38-66 yrs for $\alpha = 10^{-6}$ (the lower end of each range corresponds to large chondrules and the upper end to small chondrules; see Section 5.2.2 for more detailed discussion). As expected, the time needed to build a rim of a given thickness decreases with increasing turbulence strength.

Using a linear fit to relate FGR thickness to elapsed growth time, we obtain the following growth rates (the increase in the rim thickness per unit time): 6100 μm/yr for $\alpha = 10^{-1}$; 1900 μm/yr for $\alpha = 10^{-2}$; 350 μm/yr for $\alpha = 10^{-3}$; 80 μm/yr for $\alpha = 10^{-4}$; 10 μm/yr for $\alpha = 10^{-5}$; and 3 μm/yr for $\alpha = 10^{-6}$. We also investigated the effect of the dust density on the growth rate. Figure 5.3b shows that the higher dust density leads to lower elapsed time for the same turbulence condition ($\alpha = 10^{-6}$), since a larger dust population can cause more frequent collisions between the chondrules and dust particles. The growth rates are 0.4, 2, 4, 17 and 36 μm/yr for the ratios of dust density to gas density equal to 0.001, 0.005, 0.01, 0.05 and 0.1, respectively.

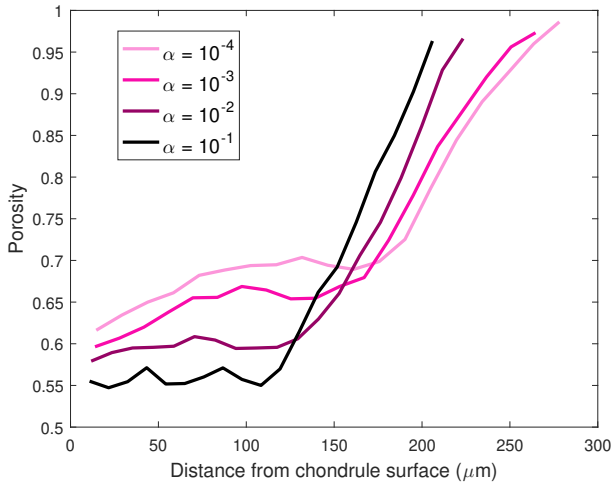

Figure 5.2: Radial profiles of dust rim porosity in each horizontal layer on a chondrule with a 600-μm radius, for four different turbulent strengths ($\alpha = 10^{-k}$, corresponding to runs ak-r6, $k = 1, 2, 3, 4$.), after accretion of $N = 60{,}000$ monomers, for particle aggregation (PA). The elapsed times are 0.52 yr (for $\alpha = 10^{-1}$), 1.62 yr ($\alpha = 10^{-2}$), 5.04 yr ($\alpha = 10^{-3}$) and 14.05 yr ($\alpha = 10^{-4}$). The position of the "knee" in the porosity curve is defined as the rim thickness.

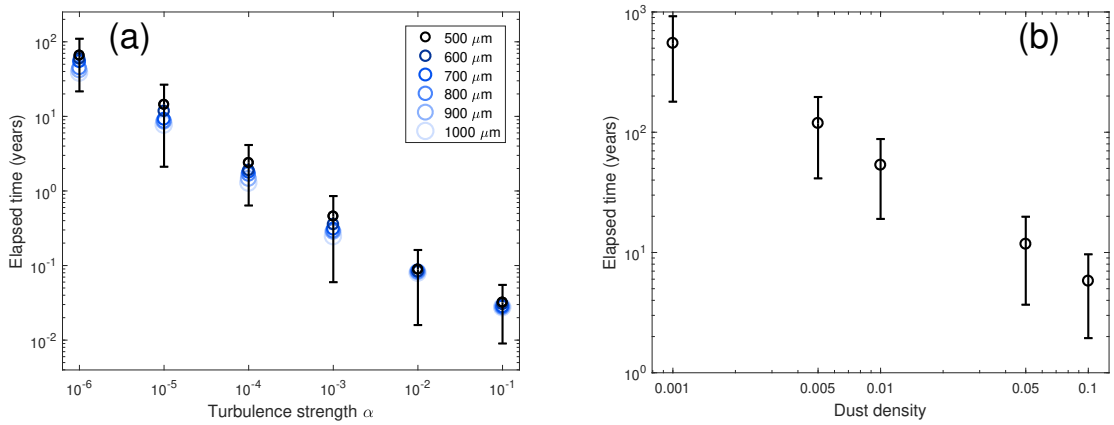

Figure 5.3: a) Elapsed time to build FGRs for different turbulence strengths and different chondrule radii (runs ak-rℓ, $k = 1, 2, ...6$, $\ell = 5, 6, ..., 10$). The midpoints correspond to a thickness of 180 μm for each chondrule size, while the lower and upper bounds (shown for the 500-μm-radius chondrule) indicate the times to build a thickness of 40 μm and 320 μm, respectively. b) Elapsed time to build FGRs on a 500-μm-radius chondrule for different dust densities with $\alpha = 10^{-6}$. The meaning of the upper and lower bounds as well as the midpoints is the same as (a).

5.2.2 Effect of Chondrule Size

Another important factor affecting dust rim growth is the size of the chondrule. Larger chondrules have higher relative velocity with respect to the dust particles (Eq. 2.89), which, together with their greater cross-sectional area, increase the collision rate between the chondrules and the dust particles. Figure 5.4 shows the number of interactions as a function of the elapsed time for different chondrule sizes and turbulence strengths. The small chondrules in weak turbulence ($\alpha = 10^{-4}$) take the longest time to collide with the dust particles. The broader separation between the curves in weak turbulence shows that the chondrule size has a greater impact on the collision rate when the relative velocity is low.

In spite of the higher collision rate, more dust is required to build a rim of a certain thickness for large chondrules than for smaller chondrules. As a consequence of these two factors, the rim thickness scales linearly with the chondrule radius, as shown in Fig. 5.5a, consistent with measurements by Metzler et al. (1992), Paque & Cuzzi (1997), Greshake et al. (2005), Hanna & Ketcham (2018), and simulations by

Ormel et al. (2008) and Carballido (2011). The linear relationship becomes steeper over time, as the greater collisional cross section and larger relative velocities of the larger chondrules increases the collision rate, causing large chondrules to grow even faster (Xiang et al. 2017b). The growth rates of chondrules of different sizes are also shown in Fig. 5.5b, in which the slopes of the lines increase with the chondrule size.

The comparison of the time evolution of the slopes for different turbulence strengths is shown in Fig. 5.6. All the rims have a thickness of 350 μm at the maximum elapsed times, which are 0.05 yr (for $\alpha = 10^{-1}$), 0.15 yr ($\alpha = 10^{-2}$), 0.66 yr ($\alpha = 10^{-3}$), 3.37 yr ($\alpha = 10^{-4}$), 20.98 yr ($\alpha = 10^{-5}$), and 92.89 yr ($\alpha = 10^{-6}$); the elapsed time for each turbulence strength is normalized by its maximum time. Although the slope increases with time for all turbulence strengths, the slope is greater and increases faster in weak turbulence than in strong turbulence, meaning that the growth rates of dust rims are less sensitive to chondrule size in strong turbulence. The dashed lines in Fig. 5.6 indicate the minimum thickness of of the dust rim, if all of the constituent dust material were compressed to a solid layer of zero porosity on the surface. This gives a lower bound of the rim thickness which may be observed in a chondrule after collisional compaction.

In addition to the change in the collision rate, the velocity difference caused by different chondrule sizes also affects the restructuring and therefore the porosity of the dust rim. Figure 5.7a shows that larger chondrules are enveloped in more compact dust rims than smaller chondrules with the same rim thickness for both strong and weak turbulence ($\alpha = 10^{-4}, 10^{-2}$), as larger chondrules have more kinetic energy for restructuring. Figure 5.7b shows the time evolution of the overall porosity of the dust rims. The colliding dust particles constantly fill in the gaps of the existing rim and form a new outermost layer which has the highest porosity. The ratio of the volume of the outermost layer to the volume of the inner layer gets lower as the rim becomes thicker. This, together with the fact that larger chondrules experience more

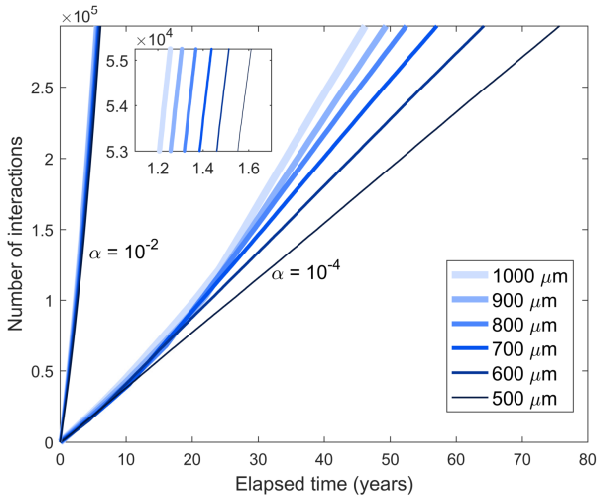

Figure 5.4: Number of interactions as a function of elapsed time for different chondrule radii, with $\alpha = 10^{-4}$ (runs a4-rℓ, $\ell = 5, 6, ..., 10$) and 10^{-2} (runs a2-rℓ, $\ell = 5, 6, ...10$). The inset is a magnification of the $\alpha = 10^{-2}$ curves between 1.1 and 1.7 years.

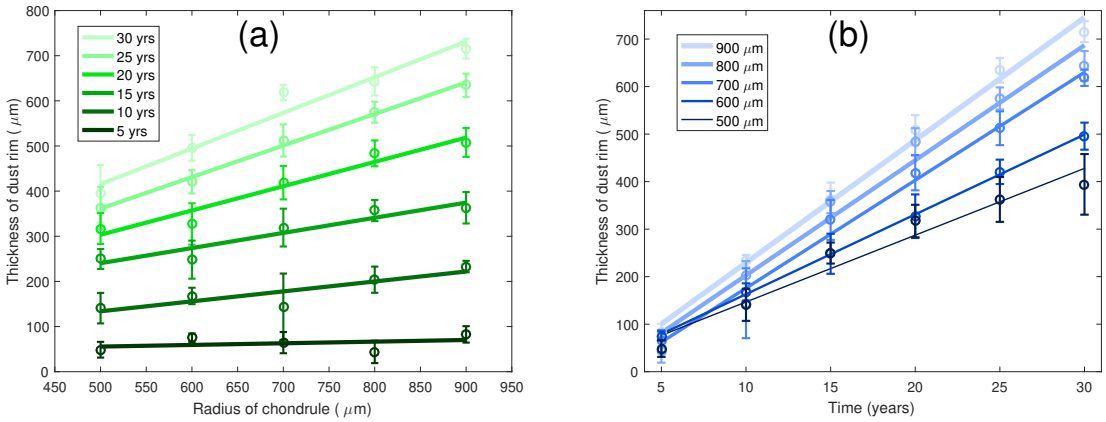

Figure 5.5: a) Thickness of dust rims formed through the addition of single monomers (PA) after $t = 5, 10, 15, 20, 25, 30$ years, with a turbulent strength $\alpha = 10^{-5}$ and for different chondrule radii. The data points correspond to runs a5-rℓ, $\ell = 5, 6, ..., 9$. The lines are linear, least-square polynomial fits to the data points. b) Same as a), except that the thickness of dust rim is a function of the elapsed time, and each line represents a chondrule size.

restructuring, results in the decrease in porosity of the whole rim over time, for all chondrule sizes, until a certain time has passed, after which the porosity is constant.

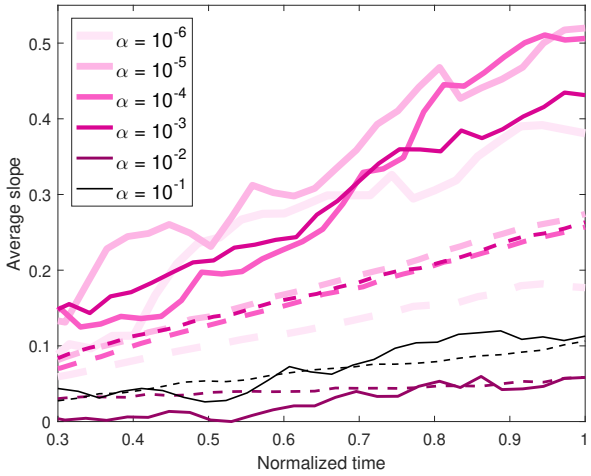

Figure 5.6: Time evolution of the slopes of rim thickness versus chondrule size (solid lines), with the elapsed time for each turbulence strength normalized by its maximum time (the time required to build a dust rim with a thickness of 350 μm). The dashed lines are for an ideal case where the dust rims are fully compacted (with zero porosity), indicating the influence of the porosity on the slope.

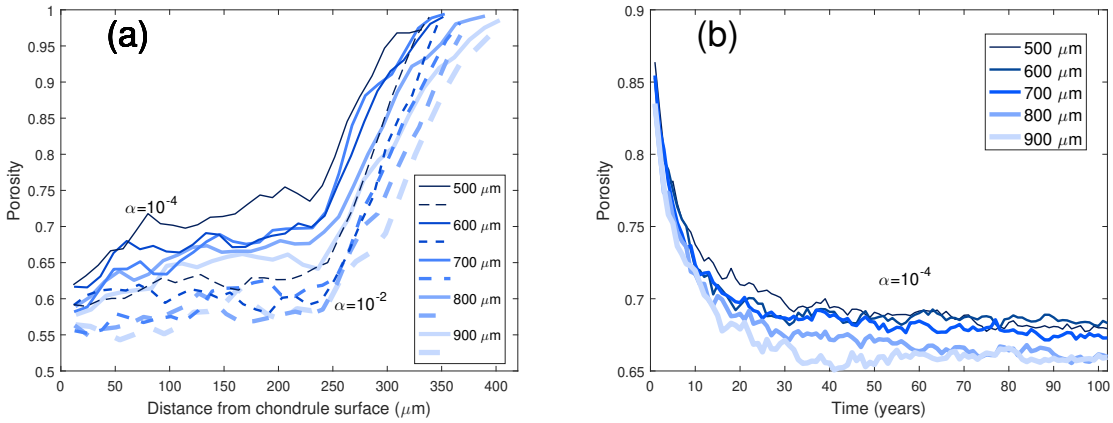

Figure 5.7: a) Radial profiles of dust rim porosity on chondrules of different sizes, for turbulent strengths $\alpha = 10^{-4}$ (*solid curves*, corresponding to runs a4-rℓ, $\ell = 5, 6, ..., 9$) and $\alpha = 10^{-2}$ (*dashed curves*, corresponding to runs a2-rℓ, $\ell = 5, 6, ..., 9$), for equal rim thickness. The data were obtained by particle aggregation (PA). b) Mean porosity of the rim (the top-most layer with porosity > 0.9 is discarded; note that this value is higher than the cutoff porosity for calculating the rim thickness, and this is an overall porosity of almost the whole rim), formed through particle aggregation (PA), as a function of time and for different chondrule radii. The turbulent strength is $\alpha = 10^{-4}$. The data correspond to runs a4-rℓ, $\ell = 5, ..., 9$.

5.2.3 Comparison between PA and CA

As dust particles in the solar nebula can form aggregates before colliding with chondrules (e.g., Scott et al. 1984), it is instructive to compare dust rims formed

through accretion of single monomers (particle aggregation, PA) and accretion of aggregates (cluster aggregation, CA). A library of small aggregates was created by building aggregates from spherical grains with the same size distribution as the monomer library. The aggregates were built using a combination of PCA (particle-cluster aggregation) and CCA (cluster-cluster aggregation), and their equivalent radii range from $0.5\ \mu m < R_\sigma < 10\ \mu m$, while their physical radii range from $1\ \mu m < R < 24\ \mu m$, (see Figure 3.1 for the definition of R_σ and R). The aggregates were binned by their equivalent radius, which was also used to calculate the relative velocity between the aggregate grain and chondrule (Eq. 2.89). Since aggregates are more porous than monomers and have larger radii than monomers of the same mass, it is less likely that the aggregates in CA will pass though the gaps of the dust rim. Instead, they are likely to stick to the outer layers of the rim. Therefore, the dust rims formed by CA are more porous than for PA, as shown in Fig. 5.8 and 5.9a. Since almost no restructuring takes place in weak turbulence ($\alpha = 10^{-4}$), the incoming particles simply add to the outer layer. Hence, the inner region of the rims for CA (up to $\sim 280\ \mu m$) has an approximate constancy of porosity as a function of distance from the chondrule surface, while for PA the porosity increases from the base of the rim to the top, with more small monomers filling the inner layers. In addition to the difference in porosity, Fig. 5.9b shows that the dust rims formed by CA have more constant monomer size distribution throughout the rims, while the average monomer size increases (especially at the top of the rims) with distance from chondrule center for dust rims formed by PA, consistent with laboratory observations of CM dust mantles that show grain-size coarsening toward the outer portions of the rim (Metzler et al. 1992; Zega & Buseck 2003).

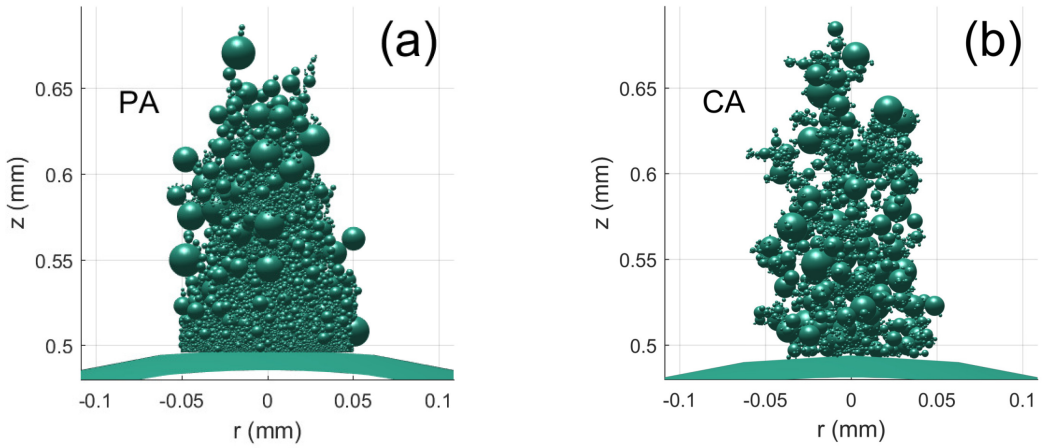

Figure 5.8: Rim growth on a 100 μm-diameter patch on the surface of a chondrule with a radius of 500 μm, formed through a) particle aggregation (PA, run a4-r5) and b) cluster aggregation (CA, run a4-r5-agg). A movie showing how small monomers pass through the rim to fill the lower layers is available online.

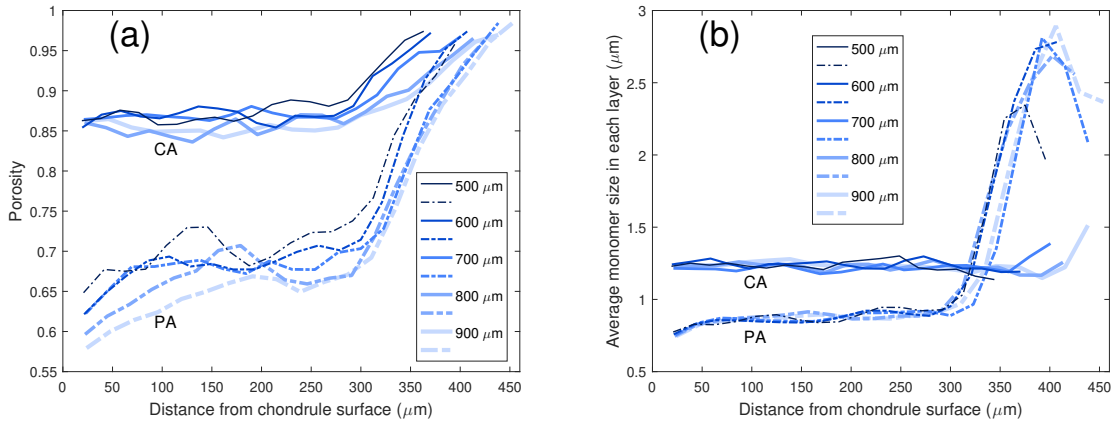

Figure 5.9: Radial profiles of a) dust rim porosity and b) average monomer size in each horizontal layer on chondrules of different radii, for same rim thickness of $\sim 290\mu m$ (the rim thickness is defined in Sec. 5.2.1). Shown are data for particle aggregation (PA, runs a4-rℓ, $\ell = 5, 6, ..., 9$) and cluster aggregation (CA, runs a4-rℓ-agg, $\ell = 5, 6, ..., 9$).

5.3 Discussion

We have calculated FGR porosities for different values of the parameters involved in the collision between chondrules and dust (either a spherical monomer or an aggregate; Secs. 5.2.1-5.2.3). We have also corroborated the linear relationship between FGR thickness and chondrule radius that has been measured by other authors (Sec. 5.2.2). We now put our results in the context of previous FGR studies.

5.3.1 Structure and Porosity of FGRs

Beitz et al. (2013) investigated FGR formation around chondrule analogs in laboratory experiments. The authors produced two types of chondrule analogs: one with a forsterite composition (radius = 0.75 mm) and one with a spinel composition (radius = 0.80 mm). The chondrule analogs were levitated inside a funnel using a gas flow, which also contained olivine dust grains of irregular shapes. These grains stuck to the chondrule analogs, with most of the stuck grains having radii in the range $\sim 0.25 - 1.5$ μm. Using scanning electron microscopy and X-ray computed tomography (CT), Beitz et al. (2013) measured the porosity profiles of the formed rims. Their data is shown in Fig. 5.10: the *black points* correspond to the rim porosity around the spinel chondrule analog, while the *white points* represent rim porosity values around the forsterite chondrule analog.

Figure 5.10 also shows our data for runs a2-r5 (*black curve*), a4-r5 (*red, solid curve*), a4-r5-agg (*red, dashed curve*), and a6-r5 (*blue curve*). Perhaps the largest difference between the numerical and the experimental data is seen close to the chondrule surface: the former shows a high porosity in the lower rim layers, while the latter exhibits very low porosity there. As Beitz et al. (2013) explain, the low porosity at the boundary between their chondrule analog and its associated dust rim is due to partial melting or sintering. Even if no melting or sintering occurred, we speculate that the low porosity close to a chondrule analog surface might be possible due to the irregular shape of the dust monomers, which can arrange themselves in more compact configurations than the spherical monomers used in our simulations. This difference in monomer shape is perhaps also responsible for the overall higher porosities in our simulations, compared to the experimentally obtained rims. Future simulations with non-spherical monomers will test these hypotheses.

The high FGR porosities calculated from our simulations ($\gtrsim 60\%$), however, are generally consistent with those obtained by Ormel et al. (2008) for the dust

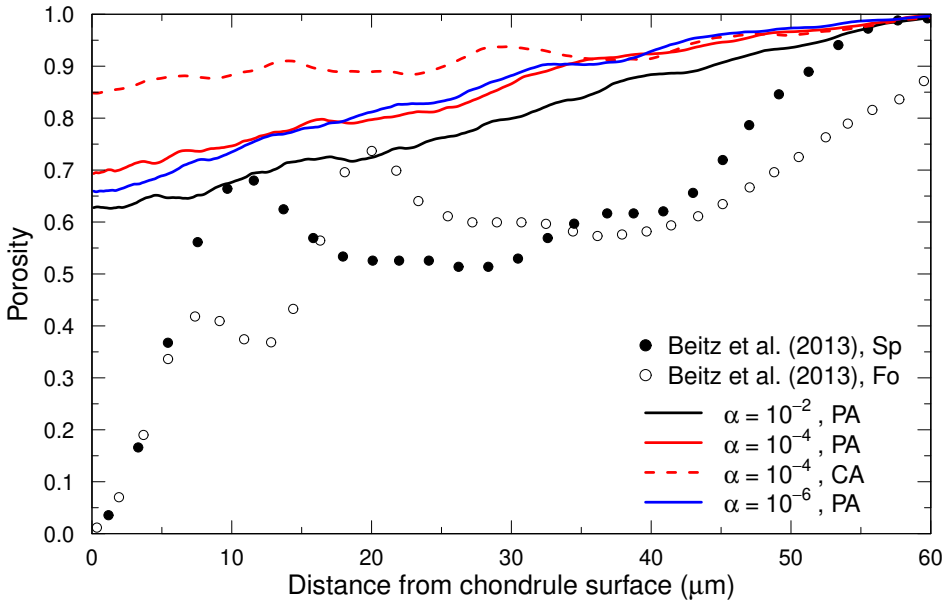

Figure 5.10: Measurements of rim porosity obtained by Beitz et al. (2013) from experiments of rim accretion onto spinel (*black points*) and forsterite (*white points*) chondrule analogs. For comparison, data from our runs a2-r5 (*black curve*), a4-r5 (*red, solid curve*), a4-r5-agg (*red, dashed curve*), and a6-r5 (*blue curve*) are also shown.

component of chondrule aggregates ($\gtrsim$ 67%), as well as with the initial porosity estimated for an FGR in Allende (70-80%, Bland et al. 2011). Such high porosities could conceivably result from gentle collisions between dust and chondrules in weak turbulence (Ormel et al. 2008).

Effects that will need to be taken into account in future work include fragmentation and erosion due to energetic collisions, as well as rim compaction due to chondrule-chondrule collisions.

5.3.2 Comparison to FGR Observations

The ultimate goal of our modeling efforts is the comparison of our results to observations of FGRs in chondrites to help shed light on the nebular conditions of FGR formation. However, the calculations presented herein apply only to the *initial* accretion of FGRs, and do not provide information regarding their subsequent structural evolution. For example, the role of FGRs as the "glue" that holds together decimeter-sized chondrule composites (Ormel et al. 2008) means that rims would be

subjected to compaction events via collisions between rimmed chondrules and other, perhaps similar, objects. It has also been suggested that weak nebular shocks may restructure the rim grains leading to a compaction fabric and lower rim porosity (Bland et al. 2011). After accretion to the chondrite parent body, the rims may be modified further by impact compaction, thermal metamorphism, and aqueous alteration. All of these processes will likely modify the rim structure and reduce porosity. Regardless, modeling the initial accretion of FGRs is an important first step towards identifying which of these nebular and parent body processes may have been involved in, and their relative influence on, post-formation FGR modification.

Bland et al. (2011) examined a CV Allende FGR fabric defined by the crystallographic alignment of olivine grains within the rim. By estimating the compressional strain needed to produce such a fabric and combining this with the current Allende porosity measured by Consolmagno et al. (2008), they estimated an initial rim porosity on the order of 70-80%. They interpreted the compaction as a post-accretional nebular process, such as a nebular shock or rimmed chondrule collision, so this initial porosity estimate should be comparable to our modeled rim porosity. For our model, porosities this high are associated with smaller chondrules (in the particle aggregation case) or with cluster aggregation (Fig. 5.9). Because the Allende chondrule is over ~ 1 mm in size, this seems to exclude particle aggregation for the formation of the rim unless the turbulence strength was much lower than 10^{-4} (Fig. 5.2). One important difference between our model and the Allende FGR, however, is that our model uses perfectly spherical grains while olivine grains are typically elongated. As we hypothesize in Section 5.3.1, irregular monomer shape may decrease the rim porosity, but future work will investigate this.

Another study that characterized strain in FGRs among several chondrules in CM Murchison found that the compression of the rims likely occurred on the parent body (Hanna & Ketcham 2018). In this case, the strain estimate from compression

of the rims and the current bulk porosity of Murchison leads to a pre-deformation rim porosity of 45% (Appendix A). Because the porosity reduction took place on the parent body it is difficult to know if this porosity estimate is directly comparable to our modeling results. In light of the Bland et al. (2011) study showing evidence of pre-parent body compression of the rim, it is likely that the 45% estimate does not represent original FGR formation porosity. Another complication is that FGR rims in CM chondrites are dominated by serpentine (a hydrous mineral) in contrast to the anhydrous olivine dominant in CV FGRs (Zolensky et al. 1993). Therefore, if CM FGRs were aqueously altered after formation, this also would have reduced the original formation porosity [although whether this hydration took place in the nebula or on the parent body is debated (e.g., Haenecour et al. 2018; Metzler et al. 1992; Tomeoka & Tanimura 2000)]. Still, these data place a lower limit ($\sim$ 45%) on the original, formational FGR porosity and is consistent with our modeling results that suggest a minimum original porosity of $\sim$ 55%.

There have been two direct observations of current, in-situ porosities of FGRs in carbonaceous chondrites. Beitz et al. (2013) calculated a $\sim$ 10% porosity for two CM Murchison rims from X-ray CT data. However, their assumptions of zero porosity in chondrule interiors and an identical mineralogical and chemical composition of rims and chondrules are likely incorrect (e.g., Fuchs et al. 1973; Hanna et al. 2015). Additionally, repeated measurements of Murchison porosity using helium ideal-gas pycnometry indicates a much higher porosity of 22.1% (Macke et al. 2011). Haenecour et al. (2018) also estimated a $\sim$ 10% porosity for FGRs in two primitive CO3.0 chondrites from reduced analytical totals in electron microprobe analysis (EMPA). This FGR porosity matched both the average matrix value and the average porosity of CO chondrites [10.8%; (Consolmagno et al. 2008)]. This observed porosity is much lower than our modeled porosity, probably for two reasons: first, CO chondrites have relatively low porosity (therefore inferences based on CO chondrites may not be

robust); second, it may again represent post-accretional processing of the FGR, most likely aqueous alteration, of which the authors found evidence within the FGRs.

Finally, we note that another assumption in our model is that the chondrule surface is smooth and spherical. In reality, chondrule surfaces can be rough and chondrule shapes can depart from spherical, possibly as primary features (Hanna & Ketcham 2018). Comparison of FGR volume with chondrule roughness suggests that increased chondrule surface roughness caused greater accumulation of dust onto the chondrule surface (Hanna & Ketcham, 2018). Forthcoming work will examine the influence of irregular chondrule surface shape on dust accumulation in our model.

5.3.3 FGR Formation Times

The results of Fig. 5.3 for the formation times of FGRs of a certain thickness (40, 180 and 320 μm) can be qualitatively compared to previous estimates by other authors. Cuzzi (2004) showed that rimming times, like our data in Fig. 5.3, decrease with increasing turbulence strength α. However, the rimming times calculated by Cuzzi (2004) correspond to a solar nebula location of 2.5 AU, where turbulent velocities are lower than at 1 AU as we consider here. Depending on the ratio ζ of rim volume to chondrule volume, rimming times obtained by Cuzzi (2004) vary between 40 yrs ($\zeta = 0.1$) and 600 yrs ($\zeta = 3.0$) at 2.5 AU, whereas at 1 AU we find the rimming times to be between 0.3 yrs ($\zeta = 0.1$) and 10 yrs ($\zeta = 3.0$), for $\alpha = 10^{-4}$.

Ormel et al. (2008) calculated the times at which the available dust in their simulations was depleted by incorporation onto chondrule surfaces, as a function of α. Once again, those times decrease with increasing α. As Ormel et al. (2008) take into account the growth of chondrule aggregates (i.e., objects composed of chondrules joined by fine-grained dust), direct comparison to our rimming times is difficult.

Gunkelmann et al. (2017) point out that the bouncing velocity of two chondrules increases by two orders of magnitude if they are covered by dust rims. Thicker and denser dust rims are more efficient in accommodating the collision energy (with

a higher bouncing velocity) than thin and porous rims, while the dust rims are partly destroyed in all cases by sputtering, even for hit-and-stick events. Our simulations show that the dust rims formed in different turbulence conditions have different porosity and growth rates, which means the colliding chondrules in different environments will have different bouncing velocities, affecting the growth of chondrule agglomerates. It will be of interest to investigate the growth rates of chondrules in various turbulent environments by conducting collisions between rimmed chondrules in our future work.

5.4 Conclusions

We conducted a numerical study of the initial accretion of fine-grained dust rims (FGRs) onto chondrule surfaces. This study is an important first step towards elucidating the structural properties of FGRs *before* the onset of impact compaction, thermal metamorphism, and aqueous alteration.

In this work, we concentrated on the porosity and the thickness of FGRs as signatures of the collisional formation process of rim structures. We compared FGRs formed in nebular turbulence of different strengths, and also investigated the roles of chondrule size and cluster aggregation. Our main conclusions are:

1. FGRs formed in environments with strong turbulence are more compact and grow more rapidly than FGRs formed in weak turbulence. In the case of strong turbulence ($\alpha \gtrsim 10^{-2}$), FGR porosity has an approximately constant value of 55 – 60% in the inner regions of the rims, while in the case of weak turbulence ($\alpha \lesssim 10^{-3}$) the porosity increases with distance from the chondrule center, from values of $\sim 60\%$ to $\sim 70\%$.

2. The times needed to build FGRs of a certain thickness decrease approximately linearly with increasing turbulence parameter α.

3. FGR thickness scales linearly with chondrule radius. This linear relation becomes steeper over time, as the greater collisional cross section and higher relative velocities of the larger chondrules increase the collision rate.

4. The mean porosity of FGRs decreases over time in weak turbulence ($\alpha = 10^{-4}$) for all chondrule sizes studied. Compaction reduces porosity from early values of $\sim 85\%$ to values between ~ 66 – 68% in ~ 100 years.

5. FGRs formed by cluster aggregation have higher porosity ($\sim 85\%$) than those formed by accretion of individual monomers (~ 60 – 70%), for all chondrule sizes studied.

Acknowledgments: this work was supported by the National Science Foundation under grant no. 1414523 (LSM and TWH).

CHAPTER SIX

The Initial Structure of Chondrule Dust Rims II: Charged Grains

This chapter submitted as [201]: Chuchu Xiang, Augusto Carballido, Lorin S. Matthews, Truell W. Hyde, "The initial structure of chondrule dust rims II: charged grains," arXiv:1911.00981.

6.1 Introduction

As dust grains become charged to varying degrees in the radiative plasma environment of the solar nebula, it is of importance to investigate how the charge effects the process of FGRs formation. In this model, both the chondrule parent body and the dust grains are charged, and the electrostatic interactions are included during the rimming/accretion process. FGRs are formed by direct accretion of spherical monomers of various sizes onto chondrule surfaces at the midplane with a distance of 1 AU from YSO. The structure of the resulting dust rim (porosity, monomer size distribution, etc.) as well as the time to build the rims are examined in order to identify the manner in which charge alters the rim structure and growth rate, and to investigate the interplay between the charge, turbulence strength, and chondrule size on dust rim growth.

6.2 Results

The structure of the dust rims and their formation time are affected by the level of turbulence, charging condition and the chondrule size. Together, these effects can be characterized by the ratio PE/KE, where PE is the electrostatic potential energy of the dust grain at the point of impact, given by $\mathrm{PE} = \frac{\epsilon_0 Q_d Q_c}{4 r_{dc}}$, with Q_d and Q_c the charges of the dust grain and the chondrule and r_{dc} the distance between the dust grain and the center of the chondrule, and the kinetic energy of the dust grain far from the chondrule is $\mathrm{KE} = \frac{1}{2} m_d v_{rel}^2$, with m_d the mass of the dust grain and v_{rel} the relative

velocity calculated from Eq. 2.89. Figure 6.1 shows the range of PE/KE averaged over the dust population for different chondrule sizes in different environments (turbulence strength; plasma conditions). Given the combined turbulence and charge levels, the results are broadly applicable over a large region of the disk where conditions match a given PE/KE. The structure of the resulting dust rims is characterized based on the distribution of monomer sizes, porosity (ψ), and the time for rim formation as a function of PE/KE.

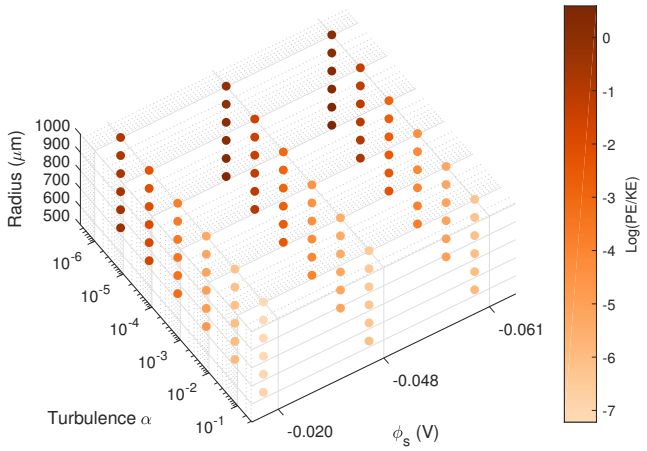

Figure 6.1: PE/KE (the ratio of a grain's electrostatic potential energy upon collision to its kinetic energy at large distances), as a function of dust surface potential (ϕ_s = -0.061 V, -0.048V, -0.020 V), turbulence strength ($\alpha = 10^{-1}$, 10^{-2}, 10^{-3}, 10^{-4}, 10^{-5}, 10^{-6}) and chondrule size (r = 500-1000 μm, in 100-μm increments).

6.2.1 Size Distribution of Dust Collected in the Rim

Although the population of dust in the protoplanetary disk has a power law size distribution with average grain radius $a_0 \approx 0.83\ \mu m$, the electrostatic repulsion alters the distribution of grains collected within the chondrule rim. The distribution of monomer size within the rim depends not only on the magnitude of the charge, but also on the relative velocities between the dust and chondrule. Representative slices through the dust rim are shown in Fig. 6.2 comparing the results for two levels of charge and turbulence. In a weakly turbulent environment, where the relative velocities are low, only the largest dust grains have enough energy to overcome the

Coulomb repulsion barrier (Fig. 6.2a), whereas for the same turbulence level, a rim consisting of uncharged grains will consist of dust particles of all sizes (Fig. 6.2b), and the smaller dust grains are able to penetrate the porous dust pile and are concentrated near the chondrule surface. In a highly turbulent region where the relative velocities are large, the distribution of dust grain sizes is similar for both charged and neutral grains (Fig 6.2c, 6.2d). However, as shown below, the distribution of particle sizes within the rim and the porosity of the rims differ.

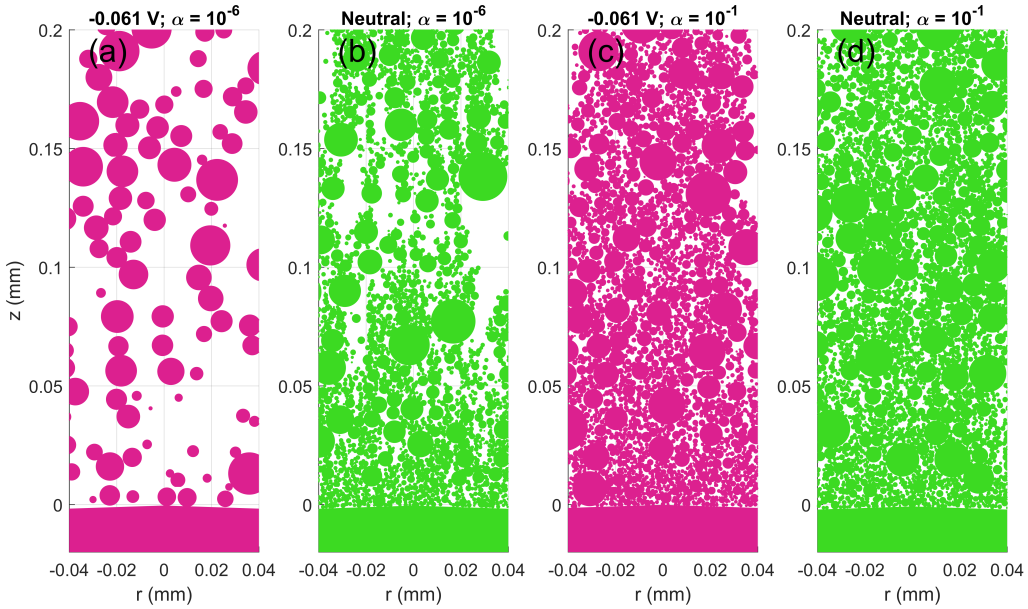

Figure 6.2: Cutaway view of rims collected on a 100-μm-diameter patch on the surface of a chondrule with a radius of 1000 μm, formed from a) charged dust (ϕ_s = -0.061V) in weak turbulence $\alpha = 10^{-6}$; b) neutral dust in weak turbulence $\alpha = 10^{-6}$; c) charged dust (ϕ_s = -0.061V) in strong turbulence $\alpha = 10^{-1}$; d) neutral dust in strong turbulence $\alpha = 10^{-1}$. The size of each circle represent the apparent monomer size due to cutting effects.

The average monomer size within dust rims when the rims have reached a thickness of 200 μm in environments with different turbulence levels ($\alpha = 10^{-1} - 10^{-6}$) and charge levels ($\phi_s$ = -0.061V, -0.048V, -0.020V) are compared in Fig. 6.3. For low values of PE/KE, the presence of charged grains has little effect, and the average monomer size within the dust rims matches that of the original dust population. Above a critical value of PK/KE $\approx$ 0.0193, the average monomer size within the rims

increases with PE/KE, as the smallest dust particles are repelled from the chondrules. For a given turbulence level (indicated by shade), and charge level (indicated by color), small chondrules (indicated by symbol size) tend to collect larger monomers.

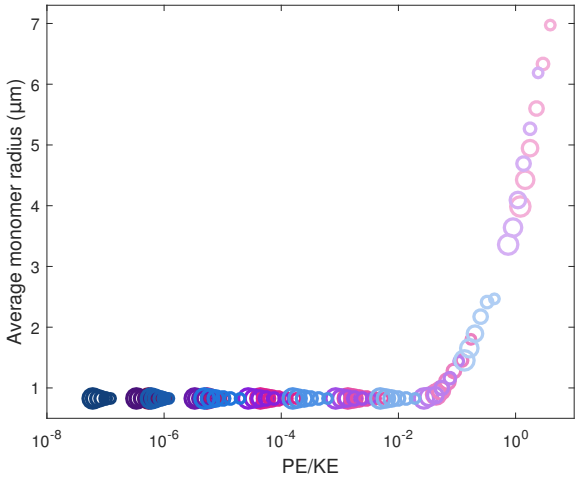

Figure 6.3: Comparison of average dust size within dust rims with a thickness of 200 μm, as a function of PE/KE. Dust surface potential is indicated by color (pink: ϕ_s = -0.061V; purple: ϕ_s = -0.048V; blue: ϕ_s = -0.020V). Turbulence level is denoted by shade($\alpha = 10^{-1}$ to $\alpha = 10^{-6}$ in order of decreasing color shades). Size of chondrule core is represented by symbol size (r = 500-1000 μm, in 100 μm increments).

The time evolution of the average dust size collected as the rim grows in thickness is shown in Fig. 6.4a for a representative chondrule with a radius of 900 μm. Neutral chondrules collect dust with the average size matching that of the population for all turbulence levels. In charged environments, the average size of the dust contained in the rims remains nearly constant for turbulence $\alpha \geq 10^{-4}$ but increases with rim growth for lower turbulence levels. This indicates that the repulsion of smaller dust grains increases as the rimmed chondrule grows and collects more charge. The average monomer size as the rim grows is also shown as a function of PE/KE in Fig. 6.4b. Again, as in Fig. 6.3, PE/KE $\approx 10^{-2}$ is a critical threshold above which the average monomer size increases with PE/KE. As the rim grows thicker, as indicated by the symbol size, more large dust grains are incorporated.

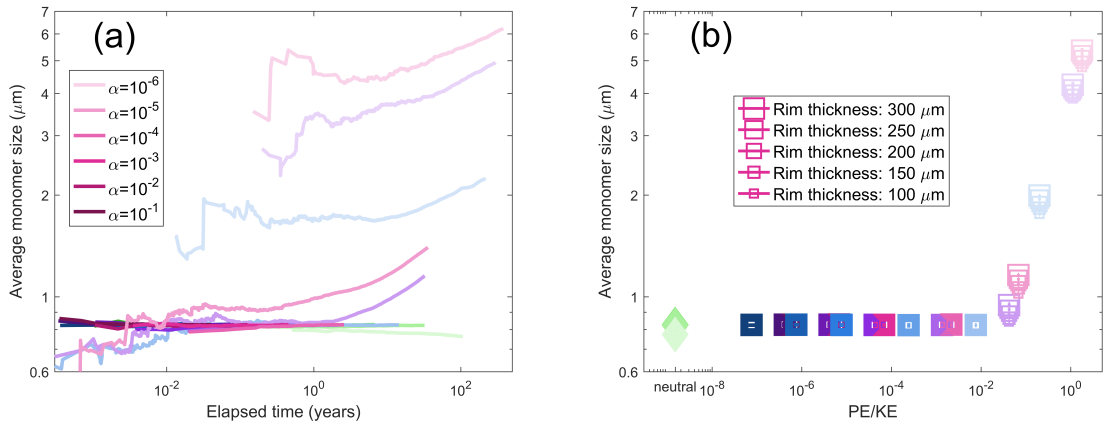

Figure 6.4: Average monomer size within dust rim on a 900-μm-radius chondrule, a) as a function of elapsed time, and b) as a function of PE/KE. Data is shown for all turbulence levels ($\alpha = 10^{-1}$ to $\alpha = 10^{-6}$ in order of decreasing color shades) and dust surface potentials (pink: ϕ_s = -0.061V; purple: ϕ_s = -0.048V; blue: ϕ_s = -0.020V). In (b), the symbol size indicates the total thickness of the rim as the rim grows from 100 μm (small squares) to 300 μm (big squares). For comparison, the results for neutral dust particles are shown in green.

To further illustrate the difference that charge plays in weak turbulence, the distribution of monomer sizes for the three different levels of surface potential at three different stages in the rim growth is presented in Fig. 6.5 for turbulence level $\alpha = 10^{-4}$. The distribution shifts towards larger monomers as a dust rim grows in thickness in the highly charged environments (ϕ_s = -0.061 V and -0.048 V), while the change is minor in the environment with a low dust surface potential (ϕ_s = -0.020 V). Overall, large monomers with radii greater than 1 μm are more common in small chondrules, in environments with high surface potentials, and in thicker rims (those that have more time for accumulation).

6.2.2 Porosity

The porosity is a measure of the open space within the dust rim. It can be examined in experimental observations of meteorite samples (Greshake et al. 2005; Friedrich 2014), and, along with other features of the fabric, provide important information about the environmental conditions where the dust rims were originally formed and the subsequent processes that alter the porosity (Thompson 1985; Gunkelmann

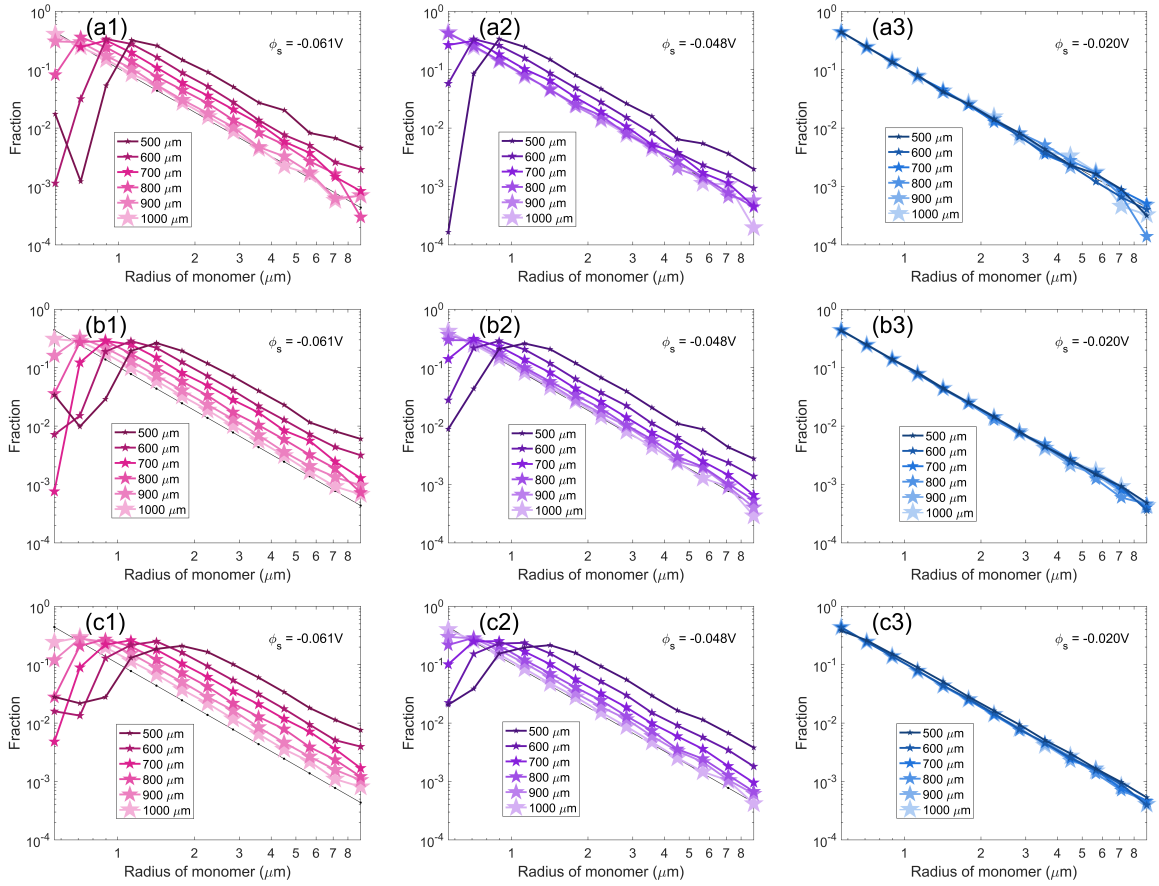

Figure 6.5: Monomer size distribution in the dust rims as the rim thickness grows from a) 100 μm, to b) 250 μm to c) 400 μm. The dust surface potential is (column 1, pink) ϕ_s = -0.61 V, (column 2, purple) ϕ_s = -0.048 V, and (column 3, blue) ϕ_s = -0.020 V. The initial chondrule radius is indicated by the symbol size, as given in the legend. The turbulence strength is $\alpha = 10^{-4}$. The distribution of the initial dust population is shown by the thin black line.

et al. 2017). Differences can be seen not only in the average porosity of the entire rim, but also in the change in the porosity of different layers within the rim. To calculate the porosity as a function of the distance from chondrule surface, the rim is divided into a certain number of horizontal layers (i.e., parallel to the chondrule's surface), with each layer having a thickness of 3–4 μm. The porosity of each layer is defined as the ratio of the volume of voids within the layer (the total volume of the layer V_{layer} minus the sum of the volume of the monomers (or monomer portions) within that layer $\sum V_d$) to the total volume of the layer, i.e., $\left(V_{layer} - \sum V_d\right)/V_{layer}$. To avoid edge effects of the dust pile, only the inner region of the pile with a radius

of 50% of the total pile radius (i.e., half the distance from the pile center to pile edge) is analyzed.

In Fig. 6.6, the change in rim porosity as a function of distance from the chondrule surface, for different charging conditions and turbulence strengths, is illustrated for a chondrule with radius $a = 700\ \mu m$. Overall, the porosity increases from the base of the rim to the top, due to the grain-size coarsening toward outer portions of FGRs, consistent with observations. This is apparently caused by the fact that small grains pass through voids and fill in the lower rim layers (Metzler et al. 1992, Zega & Buseck, 2003; see Paper 1). In relatively strong turbulence ($\alpha = 10^{-4}$; Fig. 6.6a), the charged and neutral dust rims have similar radial profiles for porosity. As turbulence weakens ($\alpha = 10^{-5}$, 10^{-6}; Fig. 6.6b, c), the relative difference in the porosity between bottom and top layers decreases with increasing dust surface potential, because it is more difficult for large dust particles (which are able to overcome the Coulomb repulsion barrier) to pass through voids.

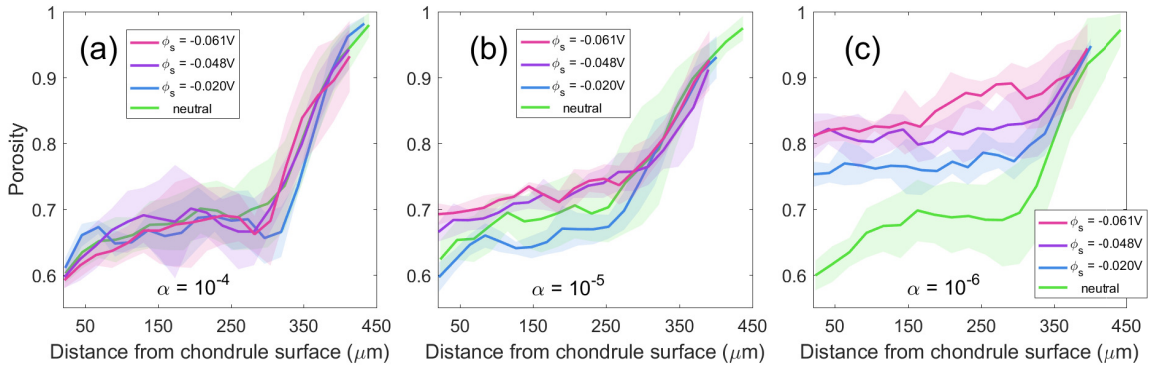

Figure 6.6: Radial profiles of dust rim porosity in each horizontal layer on a chondrule with a 700-μm radius, formed in neutral and charged environments, for equal rim thickness, defined by the distance from the chondrule surface encompassing 95% of the total rim mass. The turbulence strength is a) $\alpha = 10^{-4}$, b) $\alpha = 10^{-5}$, and c) $\alpha = 10^{-6}$. Lines are averages for five chondrule rims, with the shaded area indicating the standard deviation.

The evolution of the overall porosity of dust rims as the rims grow in thickness (defined as the average porosity of inner rim portion encompassing 95% of the total rim mass), is shown in Fig. 6.7. In strong turbulence with $\alpha \geqslant 10^{-4}$, the charged

rims and neutral rims have similar porosity, which decreases as the rim is accumulated because the small colliding dust particles constantly fill in the gaps of the existing rim (an example of $\alpha = 10^{-4}$ is shown in Figure 6.7a). In weak turbulence ($\alpha = 10^{-6}$; Figure 6.7c), higher charge increases the porosity of dust rims, and the porosity increases further as the rim grows. This is due to the increased likelihood of missed collisions with small grains caused by electrostatic repulsion, as shown in Figure 6.8. The threshold size of dust particles which are able to overcome the Coulomb repulsion barrier increases as chondrules grow larger, and the lack of small monomers filling in the pore spaces results in higher porosity. The turbulence level $\alpha = 10^{-5}$ is a turning point where the highly charged rims (ϕ_s = -0.061 V, -0.048 V) are more porous than the neutral rims and the weakly charged rims (ϕ_s = -0.020 V) are more compact than the neutral rims (Figure 6.7b).

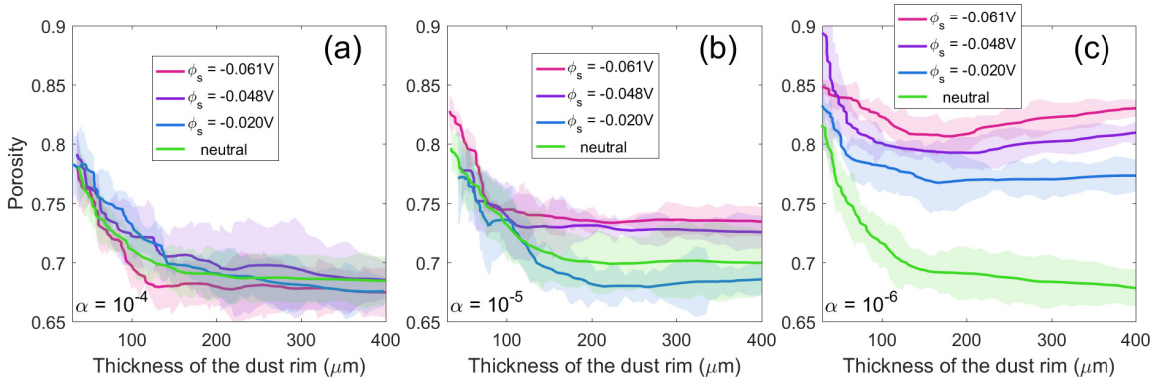

Figure 6.7: Change in average rim porosity as the rim is accumulated in different plasma conditions. Turbulence strength is a) $\alpha = 10^{-4}$, b) $\alpha = 10^{-5}$, and c) $\alpha = 10^{-6}$. Chondrule radius is 700 μm. Lines are averages for five chondrule rims, with the shaded area showing the standard deviation.

In Fig. 6.9, the evolution of rim porosity as it is accumulated is summarized for all combinations of turbulence strengths, dust surface potentials and chondrule sizes, characterized by the average PE/KE for the chondrule-dust interactions for a given set of parameters. The average porosity of dust rims decreases as they grow in thickness over time, except for values of PE/KE $\gtrsim 2$, which result in a slight increase

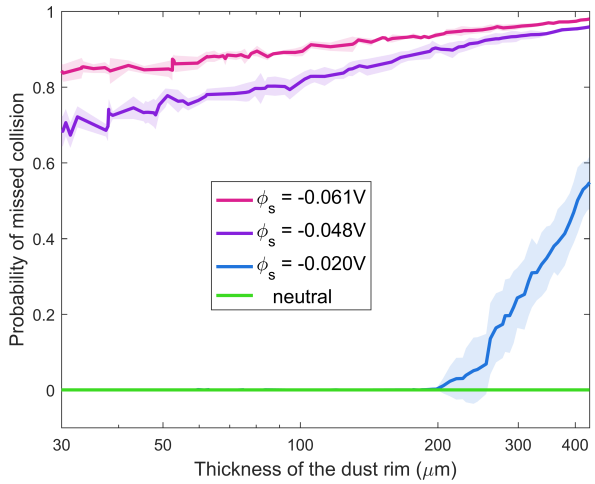

Figure 6.8: Probability of missed collision as the rim is accumulated in different plasma conditions, with turbulence strength $\alpha = 10^{-5}$. Chondrule radius is 500 μm. Lines are averages for five chondrule rims, with the shaded area showing the standard deviation.

of porosity with time. Rims with lower PE/KE have more compact structure and the porosity decreases more rapidly than those with higher PE/KE. [Note that PE/KE is the average calculated for all dust particle sizes, so even if PE/KE > 1 for the dust population, the largest dust particles in the simulation may have enough energy to overcome the Coulomb repulsion barrier; PE/KE is mainly determined by the size of the chondrule core for given environmental conditions, and only changes a little as the rim is accumulated].

Fig. 6.10 compares the average porosity of the entire rim when the rims have reached a thickness of 300 μm for chondrules in environment with different PE/KE. The porosity ψ is almost linearly proportional to the logarithm of PE/KE. Two fit lines are shown: $\psi \approx 0.023 \log(PE/KE) + 0.75$ for $log(PE/KE) \lesssim -2$, and $\psi \approx 0.060 \log(PE/KE) + 0.80$ for $log(PE/KE) \gtrsim -2$. The greater slope of the fit line for large PE/KE indicates a greater dependence of the porosity on the charge in weak turbulence. Given the same environment, larger chondrules tend to accumulate less porous rims than small chondrules, due to the greater relative velocity with respect to dust particles, which increases the restructuring and reduces the repulsion of small particles.

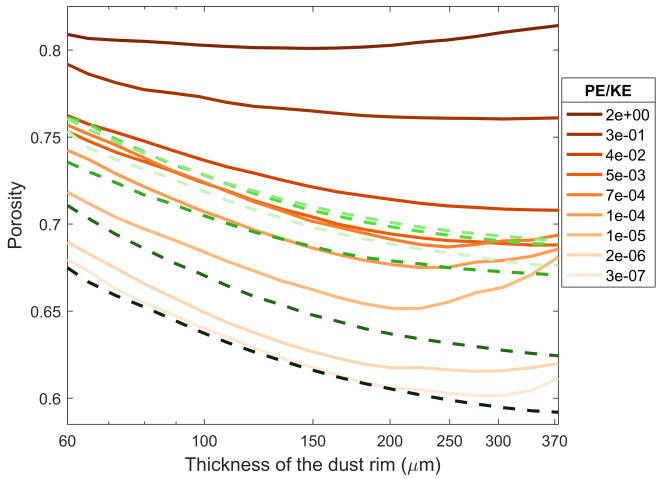

Figure 6.9: Change in average rim porosity as the rim is accumulated for different average values of PE/KE. Dust rims on chondrules of different sizes (a = 500-1000 μm, in 100-μm increments), formed in different plasma conditions (ϕ_s = -0.061 V, -0.048 V, -0.020 V), with different turbulent strengths ($\alpha = 10^{-1}$, 10^{-2}, 10^{-3}, 10^{-4}, 10^{-5}, 10^{-6}) are binned into nine groups based on the average PE/KE. Shown is the average porosity in each group. For comparison, the average porosity of neutral rims for different turbulence levels are shown in green ($\alpha = 10^{-1} - 10^{-6}$ in order of decreasing color shades).

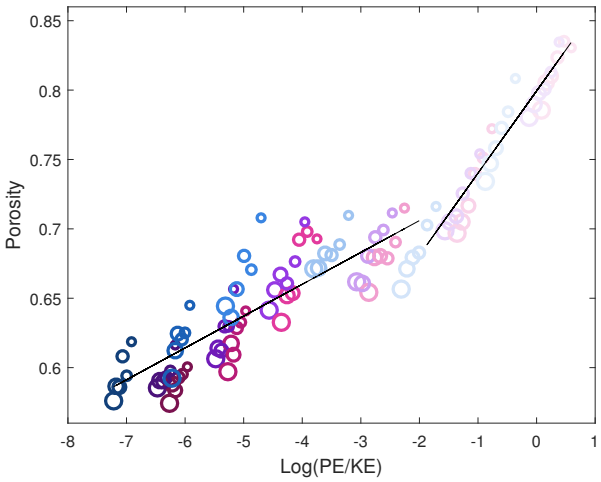

Figure 6.10: Comparisons of porosity of dust rims with a thickness of 300 μm as a function of the ratio of grains' electrostatic potential energy to the kinetic energy. Dust surface potential is indicated by color (pink: ϕ_s = -0.061V; purple: ϕ_s = -0.048V; blue: ϕ_s = -0.020V). Turbulence level is denoted by shade ($\alpha = 10^{-1}$ to $\alpha = 10^{-6}$ in order of decreasing color shades). The size of the chondrule core is represented by symbol size (r = 500-1000 μm, in 100 μm increments). The black lines are the linear, least-square polynomial fit to the data points.

6.2.3 Time to Accumulate Rims

As shown in Chapter Five, in a neutral environment, chondrules in strong turbulence accrete dust rims faster than those of the same size in weak turbulence, and large chondrules accumulate dust rims faster than small chondrules in the same environment. Here we examine the effect of charge on the time it takes a chondrule to collect a dust rim. Although the growth rates of charged and neutral rims are similar in strong turbulence, they can differ markedly in weak turbulence, as illustrated in Fig. 6.11a for a 500-μm chondrule. Differences are seen among the charged and neutral rims for turbulence levels $\alpha \leqslant 10^{-5}$, due to a large fraction of small dust particles being repelled. The critical value of turbulence at which the growth rate of charged rims starts lagging behind neutral rims differs for different chondrule sizes: it shifts towards weaker turbulence with increasing chondrule size due to the greater kinetic energy of dust particles. More complete data for all chondrule sizes, turbulence levels and charge levels are presented in Fig. 6.11b, where the growth rate is shown as a function of PE/KE. Overall, the higher the charge and the weaker the turbulence, i.e., greater PE/KE, the more the growth rates of charged rims lag behind those of neutral rims.

Figure 6.12 compares the growth rates of chondrules of different sizes in more detail. In the weakest turbulence ($\alpha = 10^{-6}$), it is shown that the rim ceases accretion before it grows to a thickness of 400 μm for the smallest chondrule (500 μm) with highest surface potential (ϕ_s = -0.061V). Therefore, in low turbulence, the presence of charge not only slows the growth rate, but can cause the rim growth to stop. The maximum rim thickness depends not only on the turbulence and charge level, but also on the chondrule size. Although for the range of the conditions and elapsed times examined here, rim growth is halted only for the smallest chondrule, larger chondrules are also expected to eventually stop accreting dust rims after reaching some maximum thickness depending on the surface charge and turbulence level.

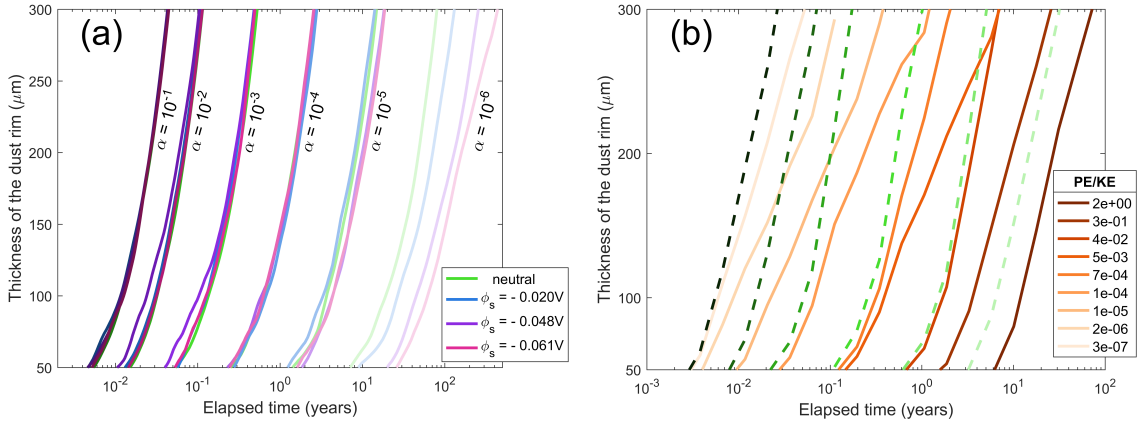

Figure 6.11: a) Thickness of the dust rim on a 500-μm-radius chondrule, as a function of elapsed time, in charged (pink: ϕ_s = -0.061V; purple: ϕ_s = -0.048V; blue: ϕ_s = -0.020V) and neutral (green lines) environments, with different turbulence strengths ($\alpha = 10^{-1}$ to $\alpha = 10^{-6}$ in order of decreasing color shades). b) Thickness of the dust rim as a function of elapsed time for different average values of PE/KE. Dust rims on chondrules are binned into 9 groups based on the average PE/KE. The green dashed lines indicate the growth of neutral dust rims in environments with different turbulence levels ($\alpha = 10^{-1} - 10^{-6}$ in order of decreasing color shades).

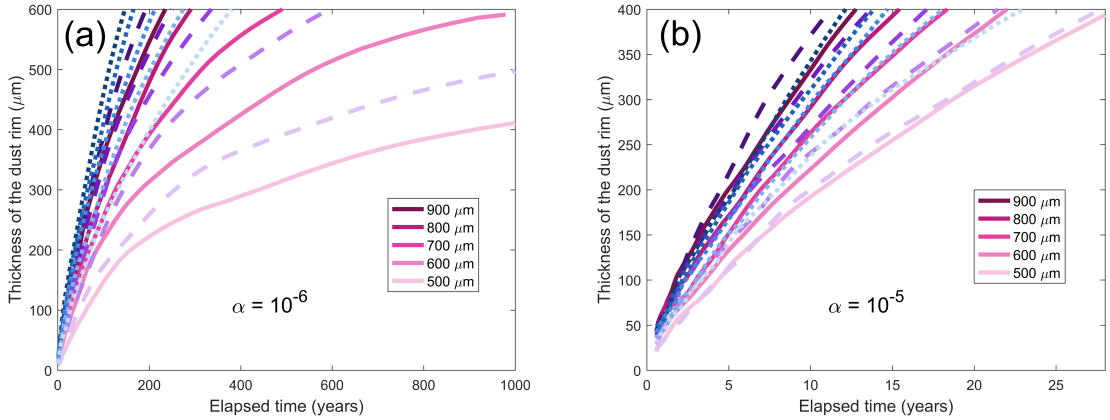

Figure 6.12: Thickness of the dust rim on chondrules with different radii as a function of elapsed time, for different plasma conditions (pink solid lines: ϕ_s = -0.061V; purple dashed lines: ϕ_s = -0.048V; blue dotted lines: ϕ_s = -0.020V). Turbulence strength is a) $\alpha = 10^{-6}$ and b) $\alpha = 10^{-5}$

.

6.3 Discussion and Conclusions

We have compared the growth of chondrule rim in neutral and weakly ionized gas in PPDs, where the collisions leading to rim growth are driven by turbulence. The turbulence strength, the amount of charge, and the chondrule size all come

together to determine the ratio of a dust particle's potential energy at the point of impact to its kinetic energy far from the chondrule. Thus differences in the porosity, thickness, and the distribution of dust sizes within the rim, as well the time needed to accumulate a rim of a given thickness, are shown to depend on the ratio PE/KE. In general, greater charge, weaker turbulence, and smaller chondrule size results in larger average monomer size, increased porosity, smaller rim thickness and greater time to accumulate the rim.

The radial profiles of dust rim porosity show that the outer regions have a higher porosity than the inner regions in all cases, and the values vary in different environments. In general, dust rims formed in stronger turbulence are more compact than those formed in weak turbulence due to more severe restructuring (see Chapter Five) and more small dust grains filling the pores. The impact of the charge on the rim porosity varies in different turbulence regimes. In a strongly turbulent environment ($\alpha \geqslant 10^{-4}$), the charge can either increase or decrease the rim porosity due to the two factors: first, the reduced relative velocity caused by the electrostatic force reduces restructuring which increases the porosity; second, the electrostatic force can alter the particle trajectories as they pass through the gaps in the rim, and the particles tend to avoid the extremities of the rim to minimize the potential energy of the configuration, which causes a more compact arrangement of monomers and decreases the porosity [note that this effect is less important when particles move fast]. The impact of the charge is negligible for $\alpha \geqslant 10^{-2}$, and FGR porosity has an approximately constant value of 50 – 65% in the inner regions of the rims formed in both charged and neutral environments. For medium turbulence levels ($\alpha = 10^{-3}$, 10^{-4}), charged rims are overall slightly more compact than neutral rims, but they both fluctuate in the range of 60 – 70%. Modelling and laboratory estimates (Ormel et al. 2008; Dominik et al. 1997; Blum 2004) show that the rolling motion within the dust layer or restructuring caused by greater collisional energy can increase the filling factor ($\phi_\sigma = 1 - \psi$) to

a value of ~ 0.33, which is close to our results. In the case of weak turbulence ($\alpha \lesssim 10^{-5}$), the presence of charge on the dust results in the very smallest dust particles being repelled from the chondrule surface. This lack of small dust grains leads to an increase in the porosity of the dust rims, as the small dust grains tend to fill in the pore spaces. Greater values of PE/KE result in more small grains being repelled and therefore higher rim porosity, and the difference between rims with different PE/KE increases as the rim grows (Fig. 6.9). The inner regions of charged rims have a porosity of 60 – 75% for $\alpha = 10^{-5}$ and 70 – 92% for $\alpha = 10^{-6}$, while the porosity of neutral dust rims ranges from 63% to 72% for these turbulence strengths.

Note that these are the initial porosities that dust rims acquired in the PPD, which can be greatly reduced during following compaction process caused by low-intensity shocks that individual rimmed chondrules or aggregates of chondrules experience before incorporated into parent bodies (strong shocks can melt chondrules; Desch et al. 2012; Thompson 1985) or by energetic collisions between agglomerations of rimmed chondrules (Bland 2011). Bland et al. (2011) researched the relationship between fabric intensity and net compression by examining the degree of alignment of olivine grain in FGRs, which indicates the amount of deformation, and reconstructed an initial rim porosity of 70 – 80%. Our results have a broader range of porosity due to the variety of conditions considered. In addition to the porosity, the repulsion of small dust grains also affects the monomer size distribution within rims, and the average monomer size is positively related to PE/KE for $\alpha \gtrsim 10^{-2}$ (Fig. 6.3).

FGRs formed in environments with strong turbulence grow more rapidly than those in weak turbulence (Ormel et al. 2008; Chapter Five). In strong turbulence, the charge affects the formation time of dust rims by changing the rim porosity and equivalent radius of the dust rim, which results in a different surface-to-mass ratio and thus relative velocity with respect to dust particles (see Eq. 2.89). In low turbulence,

the charge impacts the rim porosity and formation time mainly through the repulsion of small dust particles. As chondrules grow in size and rims become more porous, the increased surface area results in a higher surface potential, as shown in Fig. 6.13a, which poses a greater electrostatic barrier for dust particles. Meanwhile, the ratio of mass to surface area of a rimmed chondrule decreases as the thickness of the porous rim relative to the compact chondrule core increases (Fig. 6.13b), which decreases the relative velocity between chondrule and dust particles. Both factors cause more small dust particles to be repelled. Therefore, the rim becomes more porous and the growth rate slows down over time. Although larger chondrules have a higher surface potential than small chondrules, they also have a greater mass-to-surface area ratio increasing the relative velocity, which enables the dust particles to overcome the increased electrostatic barrier. Therefore, large chondrules grow faster, and form thicker and more compact rims than small chondrules. In very weak turbulence, the presence of charge not only slows the growth rate, but can cause the rim growth to stop. The maximum thickness depends on PE/KE: the lower the turbulence, the higher the charge, and the smaller the chondrule size, the thinner the dust rim that can be formed.

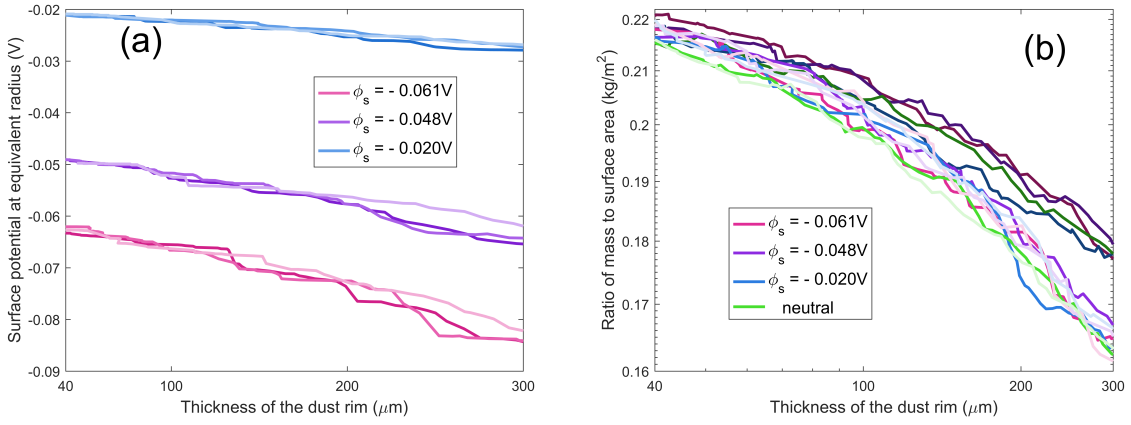

Figure 6.13: a) Charge and b) mass to surface ratio of rimmed chondrule with a radius of 700 μm as the rim is accumulated, for different dust surface potentials (pink: ϕ_s = -0.061V; purple: ϕ_s = -0.048V; blue: ϕ_s = -0.020V), and different turbulence levels ($\alpha = 10^{-1}$, 10^{-3} and 10^{-5} in order of decreasing color shades.

The cessation of rim growth caused by the charge is similar to the charge barrier for aggregate growth identified by Okuzumi (2009). However, there are several mechanisms that could prevent the freezing of rim growth. First, chondrules may resume accreting dust after traveling to environments with less charge or stronger turbulence (through radial infall, etc.). A sudden change in porosity or monomer size distribution within the rims may imply they were formed in multiple locations. Second, vertical mixing of dust particles can enhance the kinetic energy of dust particles: dust particles that couple strongly to the gas are lifted out of the region, and reenter it after they grow larger (Okuzumi 2011b). Third, positive charging of the dust grains caused by photoelectric emission due to stellar radiation (Akimkin 2015) can remove the electrostatic barrier. However, neither of the last two mechanisms is significant in dense regions of the disk (Ivlev 2016). Finally, compaction of dust rims caused by thermal alternation or nebular shock waves results in a higher mass-to-surface ratio which increases the relative velocity between chondrules and dust particles, and a lower charge-to-mass ratio which reduces the electrostatic barrier. Both factors promote the growth of dust rims.

Our main conclusions are:

- The overall porosity of neutral dust rims decreases as they grow in thickness, while that of charged rims can either decrease (low PE/KE) or increase (high PE/KE). In weakly turbulent regions, higher charge results in higher rim porosity, and this increases as the rim grows.

- Deviation from the initial grain size distribution (with a greater proportion of large monomers incorporated into the rim) increases for greater charge, weaker turbulence, and smaller chondrule cores. In addition, the deviation from the initial monomer distribution increases as the rim increases in thickness (given more time to accumulate).

- The higher the charge and the weaker the turbulence, the more the growth rates of charged rims lag behind those of neutral rims. In low turbulence ($\alpha < 10^{-4}$), the presence of charge not only slows the growth rate, but can cause the rim growth to stop.

Acknowledgments: Support from the National Science Foundation grant PHY-1707215 is gratefully acknowledged.

CHAPTER SEVEN

Conclusions and Outlook

A "detailed-MC" model simulating dust grain growth and chondrule dust rim formation has been presented. This model incorporates the detailed physical characteristics of aggregates in the collision process and uses a MC algorithm to simulate the collisional evolution of a dust population and chondrule dust rims in a protoplanetary disk. The study examines the impact of the environment, such as plasma condition and turbulence level, and the physical characteristics of particles, such as the diversity of particle size and porosity, on the collision process. In turn, it is also investigated how the collision process affects the characteristics of resulting aggregates/dust rims. Dust growth and FGR formation are compared over a range of nebular conditions (charging levels, turbulence levels), by quantifying their physical characteristics and timescales for growth. A summary of the results and a discussion about future work are presented in the following sections.

7.1 Dust Growth

7.1.1 Results

Charge is an important factor in the process of dust coagulation, as it can cause missed collisions and affect the monomer size distribution as well as porosity of aggregates. Highly charged aggregates contain larger monomers than weakly charged and neutral aggregates, as small monomers have a high charge-to-mass ratio and are repelled from highly charged grains. The average monomer size within aggregates increases with larger surface potential and lower turbulence. As aggregates grow larger, the increased relative velocity enables small grains to be incorporated into large aggregates. Therefore, the average monomer size decreases over time in highly

charged, weakly turbulent environments, while it is fairly constant in neutral and weakly charged, strongly turbulent environments.

Although the repulsion of small grains increases the porosity of aggregates, charge can also decrease the porosity of resulting aggregates by causing colliding particles to alter their path or rotate to minimize the potential energy of the configuration. In addition, aggregates grow mainly through PCA in highly charged, weakly turbulent environments, i.e., by accretion of monomers onto large aggregates. It is easier for monomers to pass through the pores of aggregates and fill in the gaps of aggregates, resulting in lower porosity. As a result of these factors, in general charged aggregates tend to be more compact than neutral aggregates, and highly charged aggregates are more compact than those with a low charge for a given turbulence level.

The more compact structure of charged particles increases their relative velocities, which enhances the collision rate and enables the growth of a weakly charged population to catch up with neutral population after lagging behind in the early stage of dust growth. However, highly charged populations, despite their compact structure, are unable to catch up, due to a large amount of missed collisions. Although for a given turbulence level, highly charged populations grow most slowly, they grow to a larger size before reaching the bouncing barrier, due to reduced relative velocity by electrostatic repulsion. The maximum particle size reached before bouncing occurs is positively correlated with charge for a given turbulence level.

Different charging levels also cause dust populations to grow with different modes. For highly charged population, once a critical size is reached, the largest particles in the population grow very rapidly ("runaway growth'), while the rest of the population grows very slowly. The particles with runaway growth are a small proportion of the population, resulting in a population with few large aggregates and a lot of remaining monomers and small aggregates. On the other hand, for neutral

and weakly charged populations, particles grow collectively, and almost all monomers have collided and formed aggregates before bouncing occurs.

In addition to the charge and porosity, the diversity of particle size also plays an important role in dust coagulation. It not only increases the growth rate of particles, as greater size difference results in higher relative velocity, but also reduces their porosity through more efficient packing, which further increases the growth rate due to the weak coupling of compact particles to the gas. For charged particles, the diversity of both the porosity and size are important to overcoming the growth barrier.

7.1.2 Future Work for Growth of Aggregates in PPDs

This study focused on the hit-and-stick regime for low-velocity collisions. Regression analysis shows that the charge, compactness factor, equivalent radius and relative velocity are the greatest contributors to the collision process in this regime. As aggregates grow larger and become less coupled to the ambient gas, they develop greater relative velocities, which can lead to destructive collisions. As charged particles are more compact and comprised of larger monomers, they are more subject to bouncing and fragmentation. The next step of this research is to simulate other types of collision outcomes, such as bouncing, fragmentation, erosion and mass transfer using LIGGGHTS (an Open Source Discrete Element Method Particle Simulation Software), and develop a heuristic model for the collision rate as well as the physical characteristics of the resulting aggregates based on the data recorded from actual collisions. This new kernel will be used to simulate the evolution of a dust population over long time periods relevant to protoplanetary disk evolution.

7.2 FGRs

7.2.1 Results

The turbulence strength, the amount of charge, and the size of the chondrule core all come together to determine the ratio of a dust particle's potential energy at

the point of impact to its kinetic energy far from the chondrule. Thus, differences in the porosity, thickness, and the distribution of dust sizes within the rim, as well as the time needed to accumulate a rim of a given thickness, are shown to depend on the ratio PE/KE.

Neutral chondrules collect dust grains representative of the size distribution in the local environment, while in environments with high PE/KE, large monomers are selectively incorporated into rims due to the repulsion of small monomers. The average monomer size and the deviation from the initial grain size distribution are positively related to the charge as well as rim thickness (thicker rims indicate more time for accumulation), and negatively related to the turbulence level and the size of chondrule core.

FGRs formed in strong turbulence are more compact than those formed in weak turbulence, and FGRs formed by accretion of individual monomers (PA) are more compact than those formed by cluster aggregation (CA). Higher charge results in higher rim porosity in weakly turbulent regions, while in strong turbulence, charged and neutral rims have similar porosity. Differences can be seen not only in the average porosity of the entire rim, but also in the change in the porosity of different layers within the rim. For PA with strong turbulence ($\alpha \gtrsim 10^{-2}$) and CA, rim porosity has an approximately constant value in the inner regions of the rims, while for PA with weak turbulence ($\alpha \lesssim 10^{-3}$), especially for highly charged rims, the porosity increases with distance from the chondrule center. As dust rims grow in thickness, their overall porosity decreases in a neutral environment, while in charged environments, the porosity can either decrease (low PE/KE) or increase (high PE/KE).

The linear relationship between chondrule size and rim thickness is investigated. Larger chondrules have higher collision rate with dust particles due to their greater relative velocity with respect to dust particles and the greater cross-sectional area. However, more dust is required to build a rim of a certain thickness for large

chondrules than for smaller chondrules. As a consequence of these two factors, FGR thickness scales linearly with chondrule radius for equal elapsed time. This linear relation becomes steeper over time, as the greater collisional cross section and higher relative velocities of the larger chondrules increase the collision rate.

FGRs formed in environments with strong turbulence grow more rapidly than those formed in weak turbulence, and the times needed to build FGRs of a certain thickness decrease approximately linearly with increasing turbulence parameter α. In the case of low PE/KE, charged rims have similar growth rates as neutral rims, while for high PE/KE, the greater the charge and the weaker the turbulence, the more the growth rates of charged rims lag behind those of neutral rims. In low turbulence ($\alpha < 10^{-4}$), the presence of charge not only slows the growth rate, but can cause the rim growth to stop. The maximum thickness depends on PE/KE: the lower the turbulence, the higher the charge, and the smaller the chondrule size, the thinner the dust rim that can be formed.

In summary, a higher PE/KE, i.e., greater charge, weaker turbulence, and smaller chondrule size, results in larger average monomer size, increased porosity, smaller rim thickness and greater time to accumulate the rim.

7.2.2 Future Work on the Growth of Chondrule Rims

Note that the porosities of FGRs obtained in this study are the initial porosities that dust rims acquired in the PPD, which can be greatly reduced during the compaction processes that follow, such as those caused by low-intensity shocks that individual rimmed chondrules or aggregates of chondrules experience before being incorporated into parent bodies or by energetic collisions between agglomerations of rimmed chondrules. In addition to impact compaction, thermal metamorphism and aqueous alteration can also reduce the dust rim porosity. Future work should take these factors into consideration.

This model assumes that both the chondrule core and dust monomer are spherical with smooth surfaces. In reality, chondrule surfaces can be rough and chondrule shapes can depart from spherical, possibly as primary features. Comparison of FGR volume with chondrule roughness suggests that increased chondrule surface roughness caused greater accumulation of dust onto the chondrule surface (Hanna & Ketcham, 2018). Dust monomers in the PPD also have irregular shapes, which can arrange themselves in more compact configurations than spherical monomers, reducing the rim porosity. Future work should examine the influence of irregular shape of chondrule core/dust monomer on dust accumulation and rim porosity.

FGRs act as a cushion and are compressed in energetic collisions between rimmed chondrules. Thicker and denser dust rims are more efficient in dissipating the collision energy than thin and porous rims, resulting in higher critical bouncing velocity. The compaction of dust rims increases the relative velocities of chondrules with respect to other particles, which leads to destructive collisions such as erosion and fragmentation, limiting the further growth of dust rims. On the other hand, both the greater relative velocity and lower charge-to-mass ratio resulting from compaction can alleviate the electrostatic barrier. It will be of interest to simulate collisions between rimmed chondrules and/or agglomerates of chondrules, taking into account the erosion, fragmentation and compaction of dust rims, and investigate the effect of dust rims on the collision process in future work.

APPENDIX

APPENDIX A

Initial porosity of compacted Murchison FGRs

Hanna and Ketcham (2018) found that that Murchison FGRs varied in thickness and were consistently thinner (compressed) in the direction of maximum strain within the meteorite. The maximum FGR thickness was 9.2% of the maximum chondrule length and the minimum FGR thickness was 6.4% (of maximum chondrule length) [refer to Fig. 6F of Hanna & Ketcham (2018)]. Therefore the maximum relative thickness difference between compressed and uncompressed portions of the rim is $0.064/0.092 = 0.70$. In other words, the thickness of the FGRs has been reduced by up to 30%. If we assume the current bulk porosity of Murchison (22.1%; Macke et al., 2011) is the current porosity of the FGRs in Murchison, we can use equation (9) of Hanna et al. (2015) to estimate the maximum initial porosity of the FGRs at $\sim$45%.

BIBLIOGRAPHY

[1] Akimkin, V.V., 2015. A Possible Mechanism for Overcoming the Electrostatic Barrier Against Dust Growth in Protoplanetary disks. Astron. Rep. 59, 747-761.

[2] Alexander, R., Pascucci, I., Andrews, S., Armitage, P., Cieza, L., 2013. The Dispersal of Protoplanetary Disks. arXiv:1311.1819.

[3] Allen, J.E., 1992. Probe theory - the orbital motion approach. Phys. Scr. 45, 497-503.

[4] Armitage, P.J., 2011. Dynamics of Protoplanetary Disks. Annu. Rev. Astron. Astrophys. 49, 195-236.

[5] Ashworth, J.R., 1977. Matrix textures in unequilibrated ordinary chondrites. Earth Planet. Sci. Lett. 35, 25-34.

[6] Bai, X., 2013. Wind-driven Accretion in Protoplanetary Disks. II. Radial Dependence and Global Picture. Astrophys. J. 772, 96.

[7] Bai, X., Stone, J.M., 2013. Wind-driven Accretion in Protoplanetary Disks. I: Suppression of the Magnetorotational Instability and Launching of the Magnetocentrifugal Wind. Astrophys. J. 769, 76.

[8] Bai, X., Stone, J.M., 2014. Magnetic flux concentration and zonal flows in magnetorotational instability turbulence. Astrophys. J. 796, 31.

[9] Balbus, S.A., Hawley, J.F., 1991. A powerful local shear instability in weakly magnetized disks. I - Linear analysis. II - Nonlinear evolution. Astrophys. J. 376, 214-233.

[10] Balbus, S.A., Hawley, J.F., 1998. Instability, turbulence, and enhanced transport in accretion disks. Rev. Mod. Phys. 70, 1.

[11] Basu, A., Roy, S., 2014. Equipartition magnetic fields and star formation rates in normal galaxies at sub-kpc scales. arXiv:1402.2229.

[12] Battaner, E., 1996. Astrophysical Fluid Dynamics. Cambridge University Press. ISBN 0-521-43747-4.

[13] Beitz, E., Guttler, C., Blum, J., Meisner, T., Teiser, J., Wurm, G., 2011. Low-velocity Collisions of Centimeter-sized Dust Aggregates. Astrophys. J. 736, 34.

[14] Beitz E., Blum J., Mathieu R., Pack A., Hezel D. C., 2013. Experimental investigation of the nebular formation of chondrule rims and the formation of chondite parent bodies. Geochim. Cosmochim. Acta 116, 41-51.

[15] Bellan, P.M., 2008. Fundamentals of Plasma Physics. Cambridge University Press.

[16] Birnstiel, T., Klahr, H., Ercolano, B., 2012. A simple model for the evolution of the dust population inprotoplanetary disks. Astron. Astrophys. 539, A148.

[17] Birnstiel, T., Fang, M., Johansen, A., 2016. Dust Evolution and the Formation of Planetesimals. Space Sci. Rev. 205, 41-75.

[18] Bittencourt, J.A., 1980. Fundamentals of Plasma Physics. Springer.

[19] Bland, P.A., Howard, L.E., Prior, D.J., Wheeler, J., Hough, R.M., Dyl, K.A., 2011. Earliest rock fabric formed in the Solar System preserved in a chondrule rim. Nat. Geosci. 4, 244-247.

[20] Blum, J., Münch, M., 1993. Experimental Investigations on Aggregate-Aggregate Collisions in the Early Solar Nebula. Icarus 106, 151-167.

[21] Blum, J., Wurm, G., 2000. Experiments on Sticking, Restructuring, and Fragmentation of Preplanetary Dust Aggregates. Icarus 143, 138-146.

[22] Blum, J., Schräpler, R., 2004. Structure and mechanical properties of high-porosity macroscopic agglomerates formed by random ballistic deposition. Phys. Rev. Lett. 93(11):115503.

[23] Blum, J., 2010. Dust growth in protoplanetary disks - a comprehensive experimental/theoretical approach. Res. Astron. Astrophys. 10, 1199.

[24] Blum, J., 2018. Dust evolution in protoplanetary discs and the formation of planetesimals What have we learned from laboratory experiments? Space Sci. Rev. 214, 52.

[25] Boss, A.P., Durisen, R.H., 2005. Chondrule-forming shock fronts in the solar nebula: A possible unified scenario for planet and chondrite formation. Astrophys. J. Lett. 621, L137.

[26] Boulanger, F., Cox, P., Jones, A.P., 2000. Course 7: Dust in the Interstellar Medium. In F. Casoli, J. Lequeux, F. David (eds.). Infrared Space Astronomy, Today and Tomorrow. P. 251.

[27] Brauer, F., Henning, Th., Dullemond, C. P., 2008. Planetesimal formation near the snow line in MRI-driven turbulent protoplanetary disks. Astron. Astrophys. 487, L1-L4.

[28] Brearley, A. J., 1993. Matrix and fine-grained rims in the unequilibrated CO3 chondrite, ALHA77307 - Origins and evidence for diverse, primitive nebular dust components. Geochim. Cosmochim. Acta 57, 1521-1550.

[29] Brearley, A. J., 1999. Origin of graphitic carbon and pentlandite in matrix olivines in the allende meteorite. Science 285, 1380-1382.

[30] Cameron, A.G.W., 1978. Physics of the primitive solar accretion disk. Moon and the Planets 18, 5-40.

[31] Carballido, A., 2011. Accretion of dust by chondrules in a MHD-turbulent solar nebula. Icarus 211, 876-884.

[32] Carrera, D., Johansen, A., Davies, M.B., 2015. How to form planetesimals from mm-sized chondrules and chondrule aggregates. Astron. Astrophys. 579, A43.

[33] Chambers, J.E., 2003. Planet Formation. Treatise Geochem. 1, 461-475.

[34] Chokshi, A., Tielens, A.G.G.M., Hollenbach, D., 1993. Dust coagulation. Astrophys. J. 407, 806-819.

[35] Chow, V.W., Mendis, D.A., Rosenberg, M., 1993. Role of grain size and particle velocity distribution in secondary electron emission in space plasmas. J. Geophys. Res. 98, 19065-19076.

[36] Clayton, R.N., Mayeda, T.K., 1989. Oxygen Isotope Classification of Carbonaceous Chondrites. Abstracts of the Lunar and Planetary Science Conference 20, 169.

[37] Compton, K.T., Langmuir, I., 1930. Electrical Discharges in Gases. Part I. Survey of Fundamental Processes. Rev. Mod. Phys. 2, 123-242.

[38] Conde, L., 2018. An Introduction to Plasma Physics and its Space Applications. IOP Concise Physics.

[39] Consolmagno, G., Britt, D., Macke, R, 2008. The significance of meteorite density and porosity. Chem. Erde-Geochem. 69, 1-29.

[40] Cuzzi, J.N., Dobrovolskis, A.R., Champney, J.M., 1993. Particle-gas dynamics in the midplane of a protoplanetary nebula. Icarus 106, 102-134.

[41] Cuzzi, J.N., 2004. Blowing in the wind: III. Accretion of dust rims by chondrule-sized particles in a turbulent protoplanetary nebula. Icarus 168, 484-497.

[42] Cuzzi, J.N., Alexander C.M.O'D., 2006. Chondrule formation in particle-rich nebular regions at least hundreds of kilometres across. Nature 441, 483-485.

[43] Cuzzi, J.N., Hogan, R.C., Shariff, K., 2008. Toward Planetesimals: Dense Chondrule Clumps in the Protoplanetary Nebula. Astrophys. J. 687, 1432-1447.

[44] Desch, S.J., Morris, M.A., Connolly, H.C., Boss, A.P., 2012. The importance of experiments: Constraints on chondrule formation models. Meteorit. Planet. Sci. 47, Nr7, 1139-1156.

[45] Di Francesco, J., Evans II, N.J., Caselli, P., Myers, P.C., Shirley, Y., Aikawa, A., Tafalla, M., 2006. An Observational Perspective of Low-Mass Dense Cores I: Internal Physical and Chemical Properties. arXiv:astro-ph/0602379.

[46] Dominik, C., Tielens, A.G.G.M., 1997. The Physics of Dust Coagulation and the Structure of Dust Aggregates in Space. Astrophys. J. 480, 647-673.

[47] Dominik, C., 2015. Disk formation and structure. EPJ Web of Conferences 102, 00002.

[48] Dullemond, C.P., Dominik, C., 2004. The effect of dust settling on the appearance of protoplanetary disks. Astron. Astrophys. 421, 1075-1086.

[49] Dullemond, C.P., Hollenbach, D., Kamp, I., D'Alessio, P., 2007. Models of the Structure and Evolution of Protoplanetary Disks. Protostars and Planets V, 555-572.

[50] Ehrenfreund, P., Fraser, H., Blum, J., Cartwright, J.H., Garcıa-Ruiz, J., Hadamcik, E., Levasseur-Regourd, A., Price, S., Prodi, F., Sarkissian, A, 2003. Physics and chemistry of icy particles in the universe: answers from microgravity. Planet. Space Sci. 51, 473-494.

[51] Ferriere, K., 2001. The Interstellar Environment of our Galaxy. Rev. Mod. Phys. 73 (4): 1031-1066.

[52] Feynman, R.P., Leighton, R.B., Sands, M.L., 1963. Feynman Lectures on Physics. Reading, Mass: Addison-Wesley Pub. Co.

[53] Field, G.B., Goldsmith, D.W., Habing, H.J., 1969. Cosmic-Ray Heating of the Interstellar Gas. Astrophys. J. 6, 670.

[54] Flynn, G., 1994. Interplanetary dust particles collected from the stratosphere: physical, chemical, and mineralogical properties and implications for their sources. Planet. Space Sci. 42, 1151-1161.

[55] Friedrich, J.M., Perrotta, G.C., Kimura, M, 2014. Compositions, geochemistry, and shock histories of recrystallized LL chondrites. Geochim. Cosmochim. Acta 139, 83-97.

[56] Fuchs, L.H., Olsen E., Jensen K. J., 1973. Mineralogy, mineral-chemistry, and composition of the Murchison (C2) meteorite. Smithson. Contrib. Earth Sci. 10, 39.

[57] Garaud, P., Meru, F., Galvagni, M., Olczak, C., 2013. From dust to planetesimals: an improved model for collisional growth in protoplanetary disks. Astrophys. J. 764:146.

[58] Garcia, A.J.L., Gonzalez, J.F., Pignatale, F.C., 2016. Growing porous grains: a solution to the radial-drift barrier. Proceedings of the Annual meeting of the French Society of Astronomy and Astrophysics, 449-454.

[59] Gillespie, D.T., 1975. An Exact Method for Numerically Simulating the Stochastic Coalescence Process in a Cloud. J. Atmos. Sci. 32(10), 1977-1989.

[60] Gmachowski, L., 2002. Calculation of the fractal dimension of aggregates. Icarus 211, 197-203.

[61] Goldreich, P., Schubert, G., 1967. Differential Rotation in Stars. Astrophys. J. 150, 571.

[62] Goree. J., 1994. Charging of particles in a plasma. Plasma Sources Sci. Technol. 3, 400-406.

[63] Greenberg, J.M., Hage, J.I., 1990. From interstellar dust to comets - A unification of observational constraints. Astrophys. J. 361, 260-274.

[64] Greshake, A., Krot, A.N., Flynn, G.J., Keil, K., 2005. Fine-grained dust rims in the Tagsh Lake carbonaceous chondrite: evidence for parent body alteration. Meteorit. Planet. Sci. 40, 1413-1431.

[65] Gundlach, B., Blum, J., Keller, H.U., Skorov, Y.V., 2015. What drives the dust activity of comet 67P/Churyumov-Gerasimenko? Astron. Astrophys. 583, 12.

[66] Gunkelmann, N., Kataoka, A., Dullemond, C.P., Urbassek, H.M., 2017. Low-velocity collisions of chondrules: How a thin dust cover helps enhance the sticking probability. Astron. Astrophys. 599, L4.

[67] Güttler, C., Blum, J., Zsom, A., Ormel, C.W., Dullemond, C. P., 2010. The outcome of protoplanetary dust growth: pebbles, boulders, or planetesimals? I. Mapping the zoo of laboratory collision experiments. Astron. Astrophys. 513, A56.

[68] Haenecour P., Floss C., Zega T. J., Croat T. K., Wang A., Jolliff B. L., Carpenter P., 2018. Presolar silicates in the matrix and fine-grained rims around chondrules in primitive CO3.0 chondrites: Evidence for pre-accretionary aqueous alteration of the rims in the solar nebula. Geochim. Cosmochim. Acta 221, 379-405.

[69] Hanna R.D., Ketcham R.A., Zolensky M., Behr W., 2015. Impact-induced brittle deformation, porosity loss, and aqueous alteration in the Murchison CM chondrite. Geochim. Cosmochim. Acta 171, 256-282.

[70] Hanna R.D., Ketcham R.A., 2018. Evidence for accretion of fine-grained rims in a turbulent nebula for CM Murchison. Earth Planet. Sci. Lett. 481, 201-211.

[71] Hartmann, L., Calvet, N., Gullbring, E., D'Alessio, P., 1998. Accretion and the evolution of T Tauri disks. Astrophys. J. 495, 385-400.

[72] Hartmann, L., 2000. Accretion Processes in Star Formation. Cambridge University Press. ISBN 0-521-78520-0.

[73] Havnes, O., Aanesen, T.K., Melandsø, F., 1990. On dust charges and plasma potentials in a dusty plasma with dust size distribution. J. Geophys. Res. 95, 6581-6585.

[74] Hayashi, C., 1981. Structure of the Solar Nebula, Growth and Decay of Magnetic Fields and Effects of Magnetic and Turbulent Viscosities on the Nebula. Prog. Theor. Phys. Supp. 70, 35-53.

[75] Heißelmann, D., Blum, J., Fraser, H.J., 2007. Experimental Studies on the Aggregation Properties of Ice and Dust in Planet-Forming Regions. In: Proc. 58th Int. International Astronautical Congress, 24-28, Hyderabad, India.

[76] Henyey, L.G., Lelevier, R., Levée, R.D., 1955. The Early Phases of Stellar Evolution. Publications of the Astronomical Society of the Pacific 67, 154-160.

[77] Herbst, E., 1995. Chemistry in The Interstellar Medium. Annu. Rev. Phys. Chem. 46, 27-54.

[78] Hollenbach, D.J., Yorke, H.W., Johnstone, D., 2000. Disk Dispersal around Young Stars. Protostars and Planets IV, 401-428.

[79] Homma, K.A., Okuzumi, S., Nakamoto, T., Ueda, Y., 2019. Collisional growth of organic-mantled grains and formation of rocky planetesimals. Bull. Am. Astron. Soc. 51, No. 6.

[80] Horanyi, M., Goertz, C.K., 1990. Coagulation of dust particles in a plasma. Astrophys. J. 361, 155-161.

[81] Igea, J., Glassgold, A.E., 1999. X-Ray Ionization of the Disks of Young Stellar Objects. Astrophys. J. 518, 848-858.

[82] Ivlev, A.V., Akimkin, V.V., Caselli, P., 2016. Ionization and Dust Charging in Protoplanetary Disks. Astrophys. J. 833:92.

[83] Jeans, J.H., 1902. The Stability of a Spherical Nebula. Philos. Trans. R. Soc. A 199, 1-53.

[84] Ji, H., Balbus, S., 2013. Angular momentum transport in astrophysics and in the lab. Phys. Today 66(8), 27.

[85] Johansen, A., Henning, T., Klahr, H., 2006. Dust Sedimentation and Self-sustained Kelvin-Helmholtz Turbulence in Protoplanetary Disk Midplanes. Astrophys. J. 643, 1219-1232.

[86] Johansen, A., Oishi, J.S., Mac Low, M.-M., Klahr, H., Henning, T., Youdin, A., 2007. Rapid planetesimal formation in turbulent circumstellar disks. Nature 448, 1022-1025.

[87] Johansen, A., Youdin, A., 2007. Protoplanetary Disk turbulence driven by the streaming instability: nonlinear saturation and particle concentration. Astrophys. J. 662:627-641.

[88] Kataoka, A., Tanaka, H., Okuzumi, S., Wada, K., 2013. Fluffy dust forms icy planetesimals by static compression. Astron. Astrophys. 557, 4.

[89] Kataoka, A., 2017. Dust Coagulation with Porosity Evolution. Formation, Evolution, and Dynamics of Young Solar Systems, Astrophysics and Space Science Library 445, 143-159.

[90] Kirchschlager, F., Wolf, S., 2014. Effect of dust grain porosity on the appearance of protoplanetary disks. Astron. Astrophys. 568, A103.

[91] Klessen, R.S., Glover, S.C.O., 2016. Physical Processes in the Interstellar Medium. In: Star Formation in Galaxy Evolution: Connecting Numerical Models to Reality. Springer-Verlag Berlin 85-249.

[92] Kokubo, E., Ida, S., 1998. Oligarchic growth of protoplanets. Icarus 131, 171-187.

[93] Kothe, S., 2016. Mikrogravitationsexperimente zur Entwicklung eines empirischen Stoßmodells fr protoplanetare Staubagglomerate. Ph.D. thesis, TU Braunschweig.

[94] Krijt, S., Ormel, C.W., Dominik, C., Tielens, A.G.G.M., 2015. Erosion and the limits to planetesimal growth. Astron. Astrophys. 574, A83.

[95] Krumholz, M.R., Fumagalli, M.F., da Silva, R.L., Rendahl, T., Parra, J., 2015. SLUG – Stochastically Lighting Up Galaxies. III: A Suite of Tools for Simulated Photometry, Spectroscopy, and Bayesian Inference with Stochastic Stellar Populations. Mon. Notices Royal Astron. Soc. 452, 1447.

[96] Kubsch, M., Illenseer, T.F., Duschl, W.J., 2016. Accretion disk dynamics α-viscosity in self-similar self-gravitating models. Astron. Astrophys. 588, A22.

[97] Kwok, S., 2006. Physics and Chemistry of the Interstellar Medium. University Science Books. ISBN 1-891389-46-7.

[98] Langkowski, D., Teiser, J., Blum, J. 2008. The physics of protoplanetesimal dust agglomerates. II. Low-velocity collision properties. Astrophys. J. 675, 764-776.

[99] Larson, R.B., 1969. Numerical calculations of the dynamics of collapsing proto-star. Mon. Notices Royal Astron. Soc. 145 (3): 271-295.

[100] Lauretta, D.S., Nagahara, H., Alexander, C.M.O'D., 2006. Petrology and origin of ferromagnesian silicate chondrules. In: Meteorites and the Early Solar System II (D. S. Lauretta and H. Y. McSween Jr., eds.). Univ. of Arizona, Tucson.

[101] Leitner, J., Vollmer, C., Floss, C., Zipfel, J., Hoppe, P., 2016. Ancient star-dust in fine-grained chondrule dust rims from carbonaceous chondrites. Earth Planet. Sci. Lett. 434, 117-128.

[102] Li, H., Dowell, C.D., Goodman, A., Hildebrand, R., Novak, G., 2009. Anchoring Magnetic Field in Turbulent Molecular Clouds. Astrophys. J. 704 (2): 891.

[103] Li, Z., Banerjee, R., Pudritz, R.E., Jørgensen, J.K., Shang, H., Krasnopolsky, R., Maury, A., 2014. Protostars and Planets VI, 173-194 (Tucson, AZ: Univ. Arizona Press).

[104] Lorek, S., Lacerda, P., Blum, J., 2018. Local growth of dust- and ice-mixed aggregates as cometary building blocks in the solar nebula. Astron. Astrophys. 611, A18.

[105] Lynden-Bell, D., Pringle, J.E., 1974. The evolution of viscous discs and the origin of the nebular variables. Mon. Notices Royal Astron. Soc. 168, 603-637.

[106] Ma, Q., Matthews, L.S., Land, V., Hyde, T.W., 2013. Charging of aggregate grains in astrophysical environments. Astrophys. J. 763:77.

[107] Macke R. J., Consolmagno G. J., Britt D. T., 2011. Density, porosity, and magnetic susceptibility of carbonaceous chondrites. Meteorit. Planet. Sci. 46, 1842-1862.

[108] Mamajek, E.E., Meyer, M.R., Hinz, P.M., Hoffmann, W.F., Cohen, M., Hora, J.L., 2004. Constraining the Lifetime of Circumstellar Disks in the Terrestrial Planet Zone: A Mid-Infrared Survey of the 30 Myr old Tucana-Horologium Association. Astrophys. J. 612 (1), 496-510.

[109] Mandell, A.M. 2015. Viscosity. In: Gargaud M. et al. (eds) Encyclopedia of Astrobiology. Springer, Berlin, Heidelberg.

[110] Marshall, J., Cuzzi, J., 2001. Electrostatic enhancement of coagulation in protoplanetary nebulae. Lunar Planet Sci., abstract 1262.

[111] Mathis, J. S., Rumpl, W., Nordsieck, K. H., 1977. The Size Distribution of Interstellar Grains. Astrophys. J. 217, 425-433.

[112] Matthews, L.S., Land, V., Hyde, T.W., 2012. Charging and Coagulation of Dust in Protoplanetary Plasma Environments. Astrophys. J. 744:8.

[113] Matthews, L.S., Kimery, J.B., Wurm, G., De Beule, C., Kuepper, M., Hyde, T.W., 2015. Photophoretic force on aggregate grains. Mon. Notices Royal Astron. Soc. 455, 2582-2591.

[114] Matthews, L.S., Coleman, D.A., Hyde, T.W., 2016. Multipole Expansions of Aggregate Charge: How Far to Go? IEEE T. Plasma Sci. 44(4), 519-524.

[115] Mayer1, L., Quinn, T., Wadsley, J., Stadel, J., 2002. Formation of Giant Planets by Fragmentation of Protoplanetary Disks. Science 298, 1756-1759.

[116] McKee, C.F., Ostriker, J.P., 1977. A theory of the interstellar medium - Three components regulated by supernova explosions in an inhomogeneous substrate. Astrophys. J. 218: 148-169.

[117] McLaughlin, D.E., Pudritz, R.E., 1997. Gravitational Collapse and Star Formation in Logotropic and Nonisothermal Spheres. Astrophys. J. 476, 750-765.

[118] Meakin, P., 1988. Models for Colloidal Aggregation. Annu. Rev. Phys. Chem. 39:237-267.

[119] Metzler, K., Bischoff, A., Stöffler, D., 1992. Accretionary dust mantles in CM chondrites: Evidence for solar nebula processes. Geochim. Cosmochim. Acta 56, 2873-2897.

[120] Metzler, K., 2004. Formation of accretionary dust mantles in the solar nebula: Evidence from preirradiated olivines in CM chondrites. Meteorit. Planet. Sci. 39, 1307-1319.

[121] Min, M., Dominik, C., Hovenier, J.W., de Koter, A., Waters, L.B.F.M., 2006. The 10 μm amorphous silicate feature of fractal aggregates and compact particles with complex shapes. Astron. Astrophys 445, 1005-1014.

[122] Mordasini, C., Klahr, H., Alibert, Y., Benz, W., Dittkrist, K., 2010. Theory of planet formation. arXiv:1012.5281.

[123] Morfill, G.E., Durisen, R.H., Turner, G.W., 1998. An accretion rim constraint on chondrule formation theories. Icarus 134, 180-184.

[124] Mori, S., Okuzumi, S., 2016. Electron Heating in Magnetorotational Instability: Implications for Turbulence Strength in the Outer Regions of Protoplanetary Disks. Astrophys. J. 817:52.

[125] Morozov, A.I., 2012. Introduction to Plasma Dynamics. CRC Press.

[126] Murray, N., 2011. Star Formation Efficiencies and Lifetimes of Giant Molecular Clouds in the Milky Way. Astrophys. J. 729 (2): 133.

[127] Nakagawa, Y., Nakazawa, K., Hayashi, C., 1981. Growth and Sedimentation of Dust Grains in the Primordial Solar Nebula. Icarus 45, 517-528.

[128] Nowak, M.A., Wagoner, R.V., 1991. Diskoseismology: Probing accretion disks. I - Trapped adiabatic oscillations. Astrophys. J. 378, 656-664.

[129] Okuzumi, S., 2009. Electric charging of dust aggregates and its effect on dust coagulation in protoplanetary disks. Astrophys. J. 698:1122-1135.

[130] Okuzumi, S., Tanaka, H., Sakagami, M., 2009. Numerical Modeling of the Coagulation and Porosity Evolution of Dust Aggregates. Astrophys. J. 707, 1247-1263.

[131] Okuzumi, S., Tanaka, H., Takeuchi, T., Sakagami, M, 2011a. Electrostatic barrier against dust growth in protoplanetary disks. I. Classifying the evolution of size distribution. Astrophys. J. 731:95.

[132] Okuzumi, S., Tanaka, H., Takeuchi, T., Sakagami, M, 2011b. Electrostatic barrier against dust growth in protoplanetary disks. II. Measuring the size of the "frozen" zone. Astrophys. J. 731:96.

[133] Okuzumi, S., Tanaka, H., Kobayashi, H., Wada, K., 2012. Rapid Coagulation of Porous Dust Aggregates outside the Snow Line: A Pathway to Successful Icy Planetesimal Formation. Astrophys. J. 752, 106.

[134] Okuzumi, S., Mori, S., Inutsuka, S., 2019. The Generalized Nonlinear Ohm's Law: How a Strong Electric Field Influences Nonideal MHD Effects in Dusty Protoplanetary Disks. Astrophys. J. 878:133.

[135] Ormel, C.W., Cuzzi, J.N., 2007. Closed-form expressions for particle relative velocities induced by turbulence. Astron. Astrophys. 466, 413-420.

[136] Ormel, C.W., Spaans, M., Tielens, A.G.G.M., 2007. Dust coagulation in protoplanetary disks: porosity matters. Astron. Astrophys. 461, 215-232.

[137] Ormel, C.W., Cuzzi, J.N., Tielens, A.G.G.M., 2008. Co-accretion of chondrules and dust in the solar nebula. Astrophys. J. 679, 1588-1610.

[138] Paque, J., Cuzzi, J.N., 1997. Physical characteristics of chondrules and rims, and aerodynamic sorting in the solar nebula. Lunar Planet Sci. XXVIII, 1189(abstract).

[139] Paraskov, G.B., Wurm, G., Krauss, O., 2007. Impacts into weak dust targets under microgravity and the formation of planetesimals. Icarus 191, 779-789.

[140] Paszun, D., Dominik, C., 2009. Collisional evolution of dust aggregates. From compaction to catastrophic destruction. Astron. Astrophys. 507, 1023-1040.

[141] Poppe, T., Blum, J., Henning, Th., 2000. Analogous experiments on the stickiness of micron-sized preplanetary dust. Astrophys. J. 533, 454-471.

[142] Prialnik, D., 2000. An Introduction to the Theory of Stellar Structure and Evolution. Cambridge University Press. ISBN 0-521-65065-8.

[143] Pringle, J.E., 1981. Accretion discs in astrophysics. Annu. Rev. Astron. Astrophys. 19, 137-162.

[144] Raab, R.E., de Lange, O.L., 2004. Multipole Theory in Electromagnetism. Oxford University Press.

[145] Raettig, N., Klahr, H., Lyra, W., 2015. Particle trapping and streaming instability in vortices in protoplanetary disks. Astrophys. J. 804:35.

[146] Reynolds, M., 2004. Classifications of meteorites. Journal of the Association of Lunar & Planetary Observers, The Strolling Astronomer (ISSN 0039-2502), Vol. 46, No. 1, p. 13-17.

[147] Rice, W.K.M., Lodato, G., Pringle, J.E., Armitage, P.J., Bonnell, I.A., 2004. Accelerated planetesimal growth in self-gravitating protoplanetary discs. Mon. Notices Royal Astron. Soc. 355, 543-552.

[148] Rubin, A.E., Krot, A.N., 1996. Multiple heating of chondrules. In: Chondrules and the Protoplanetary Disk, Cambridge University Press, Cambridge, 173-180.

[149] Rubin, A.E., 2010. Physical properties of chondrules in different chondrite groups: Implications for multiple melting events in dusty environments. Geochim. Cosmochim. Acta 74, 4807-4828.

[150] Saha, M.N., 1920. LIII.Ionization in the solar chromosphere. Philos. Mag., Series 6. 40 (238): 472-488.

[151] Salmeron, R., Ireland, T., 2012. Chondrule formation via extended winds in the early solar system. Workshop on Formation of the First Solids in the Solar System held November 7–9, 2011 in Kauai, Hawaii.

[152] Samarian, A.A., Vaulina, O.S., Nefedov, A.P., Fortov, V.E., James, B.W., Petrov, O.F., 2001. Positively charged particles in dusty plasmas. Phys. Rev. E 64, 056407.

[153] Sano, T., Miyama, S.M., 2000. Magnetorotational Instability in Protoplanetary Disks. II. Ionization State and Unstable Regions. Astrophys. J. 543:486-501.

[154] Schmitt, W., Henning, T., Mucha, R., 1997. Dust evolution in protoplanetary accretion disks. Astron. Astrophys. 325, 569-584.

[155] Schrapler, R., Blum, I., 2011. The Physics of Protoplanetesimal Dust Agglomerates. VI. Erosion of Large Aggregates as a Source of Micrometer-sized Particles. Astrophys. J. 734, 108.

[156] Schrapler, R., Blum, J., Krijt, S., Raabe, J.-H., 2018. The physics of protoplanetesimal dust agglomerates. X. High-velocity collisions between small and large dust agglomerates as growth barrier. Astrophys. J. 853:74.

[157] Scott, E.R.D., Rubin, A.E., Taylor, G.J., Keil, K., 1984. Matrix material in type 3 chondrites—occurrence, heterogeneity and relationship with chondrules. Geochim. Cosmochim. Acta 48, 1741-1757.

[158] Sears, W.D., Lunine, J.I., Greenberg, R., 1993. Equilibrium Nonsynchronous Rotation of Titan, Icarus 105, 259-262.

[159] Seizinger, A., Kley, W., 2013. Bouncing behavior of microscopic dust aggregates. Astron. Astrophys. 551, A65.

[160] Shakura, N.I., Sunyaev, R.A., 1973. Black holes in binary systems: Observational appearance. Astron. Astrophys. 24, 337-355.

[161] Spitzer, L., Jr.,1941. The Dynamics of the Interstellar Medium. I. Local Equilibrium. Astrophys. J. 93, 369-379.

[162] Takayama, A., Tomeoka, K., 2012. Fine-grained rims surrounding chondrules in the Tagish Lake carbonaceous chondrite: Verification of their formation through parent-body processes. Geochim. Cosmochim. Acta 98, 1-18.

[163] Teiser, J., Wurm, G., 2009. Decimetre dust aggregates in protoplanetary discs. Astron. Astrophys. 505, 351-359.

[164] Teiser, J., Kupper, M., Wurm, G., 2011. Impact angle influence in high velocity dust collisions during planetesimal formation. Icarus 215, 596-598.

[165] Tenorio-Tagle, G., 1996. Interstellar Matter Hydrodynamics and the Dispersal and Mixing of Heavy Elements. Astron. J. 111, 1641.

[166] Thommes, E.W., Murray, N., 2006. Giant planet accretion and migration: surviving the Type 1 regime. Astrophys. J. 644, 1214-1222.

[167] Thompson, W.B., 1985. Shock heating of chondrules. Meteoritics 20, 359-365.

[168] Tobiska, W.K., 1991. Revised solar extreme ultraviolet flux model. J. Atmosph. Terrestr. Phys. 53, 1005-1018.

[169] Tomeoka K., Tanimura I., 2000. Phyllosilicate-rich chondrule rims in the vigarano cv3 chondrite: evidence for parent-body processes. Geochim. Cosmochim. Acta 64(11), 1971-1988.

[170] Tonks, L., 1967. The birth of "plasma". Am. J. Phys. 35(9): 857-858.

[171] Torres del Castillo, G.F., Mendez Garrido, A., 2006. Torques on quadrupoles. Rev. Mex. Fis. 52, no. 6, 501-506.

[172] Tricco, T.S., Price, D.J., Laibe, G., 2017. Is the dust-to-gas ratio constant in molecular clouds? Mon. Notices Royal Astron. Soc. 000, 1-6.

[173] Trigo-Rodriguez, J.M., Rubin, A.E., Wasson, J.T., 2006. Non-nebular origin of dark mantles around chondrules and inclusions in CM chondrites. Geochim. Cosmochim. Acta 70, 1271-1290.

[174] Turner, N.J., Fromang, S., Gammie, C., Klahr, H., Lesur, G., Wardle, M., Bai, X., 2014. Protostars and Planets VI, 411-432 (Tucson, AZ: Univ. Arizona Press).

[175] Van Schmus, W.R., Wood, J.A., 1967. A chemical-petrologic classification for the chondritic meteorites. Geochim. Cosmochim. Acta 31, 747-754.

[176] Voelk, H.J., Jones, F.C., Morfill, G.E., Roeser, S., 1980. Collisions between grains in a turbulent gas. Astron. Astrophys. 85, 316-325.

[177] Wada, K., Tanaka, H., Suyama, T., Kimura, H., Yamamoto, T., 2008. Numerical Simulation of Dust Aggregate Collisions. II. Compression and Disruption of Three-Dimensional Aggregates in Head-on Collisions. Astron. Astrophys. 677, 1296-1308.

[178] Wada, K., Tanaka, H., Suyama, T., Kimura, H., Yamamoto, T., 2009. Collisional Growth Conditions for Dust Aggregates. Astrophys. J. 702, 1490-1501.

[179] Wada, K., Tanaka, H., Suyama, T., Kimura, H., Yamamoto, T., 2011. The Rebound Condition of Dust Aggregates Revealed by Numerical Simulation of Their Collisions. Astrophys. J. 737:36.

[180] Wada, K., Tanaka, H., Okuzumi, S., Kobayashi, H., Suyama, T., Kimura, H., Yamamoto, T., 2013. Growth efficiency of dust aggregates through collisions with high mass ratios. Astron. Astrophys. 559, A62.

[181] Wagoner, R.V., 2008. Diskoseismology. Journal of Physics: Conference Series 118, 012006.

[182] Wardle, M., 2007. Magnetic fields in protoplanetary disks. Astrophys. Space Sci. 311, 35-45.

[183] Wasson, J.T., Wetherill, G.W., 1979. Dynamical chemical and isotopic evidence regarding the formation locations of asteroids and meteorites. IN: Asteroids, A80-24551 08-91.

[184] Wasson, J.T., 1988. The building stones of the planets. IN: Mercury, A89-43751 19-91.

[185] Weidenschilling, S.J., 1977. Aerodynamics of solid bodies in the solar nebula. Mon. Not. R. Astron. Soc. 180, 57-70.

[186] Weidenschilling S.J., 1980. Dust to planetesimals: Settling and coagulation in the solar nebula. Icarus 44, 172-189.

[187] Weidling, R., Güttler, C., Blum, J., Brauer, F., 2009. The Physics of Protoplanetesimal Dust Agglomerates. III. Compaction in Multiple Collisions. Astrophys. J. 696, 2036-2043.

[188] Weisstein, E., 2012. Electric Quadrupole Moment. Eric Weisstein's World of Physics. Wolfram Research.

[189] Wetherill, G.W., Stewart, G.R., 1993. Formation of planetary embryos: effects of fragmentation, low relative velocity, and independent variation of eccentricity and inclination. Icarus 106, 190-209.

[190] Whipple, F.L., On certain aerodynamic processes for asteroids and comets. In: From Plasma to Planet, ed. A. Elvius, 211.

[191] White, R.J., Hillenbrand, L.A., 2005. A Long-lived Accretion Disk around a Lithium-depleted Binary T Tauri Star. Astrophys. J. 621 (1), L65-L68.

[192] Windmark, F., Birnstiel, T., Güttler, C., Blum, J., Dullemond, C.P., Henning, Th., 2012. Planetesimal formation by sweep-up: how the bouncing barrier can be beneficial to growth. Astron. Astrophys. 540, A73.

[193] Wright, J.T., Fakhouri, O., Marcy, G.W., Han, E., Feng, Y., Johnson, J.A., Howard, A.W., Valenti, J.A., Anderson, J., Piskunov, N., 2010. The Exoplanet Orbit Database. arXiv:1012.5676.

[194] Wurm, G., Blum, J., 1998. Experiments on Preplanetary Dust Aggregation. Icarus 132, 125-136.

[195] Wurm, G., Paraskov, G., Krauss, O., 2005a. Ejection of dust by elastic waves in collisions between millimeter- and centimeter-sized dust aggregates at 16.5 to 37.5 ms impact velocities. Phys. Rev. E 71(2), 021304.

[196] Wurm, G., Paraskov, G., Krauss, O., 2005b. Growth of planetesimals by impacts at ∼25 ms. Icarus 178, 253-263.

[197] Xiang, C., Matthews, L.S., Carballido, A., Hyde, T.W., 2017a. Dust growth under different plasma conditions in protoplanetary disks. APS Division of Plasma Physics Meeting 2017, abstract id. PP11.132.

[198] Xiang, C., Matthews, L.S., Carballido, A., Morris, M.A., Hyde, T.W., 2017b. Modeling the growth of chondrule dust rims with molecular dynamics. Accretion: Building New Worlds Conference 2017, abstract.

[199] Xiang, C., Matthews, L.S., Carballido, A., Hyde, T.W., 2019a. Detailed Model of the Growth of Fluffy Dust Aggregates in a Protoplanetary Disk: Effects of Nebular Conditions. arXiv:1911.04589.

[200] Xiang, C., Carballido, A., Hanna, R.D., Matthews, L.S., Hyde, T.W., 2019b. The initial structure of chondrule dust rims I: Electrically neutral grains. Icarus 321, 99-111.

[201] Xiang, C., Carballido, A., Matthews, L.S., Hyde, T.W., 2019c. The initial structure of chondrule dust rims II: charged grains. arXiv:1911.00981.

[202] Yoshida, N., Hosokawa, T., Omukai, K., 2012. Formation of the first stars in the universe. Prog. Theor. Exp. Phys. 2012 (1), 01A305.

[203] Youdin, A.N., Shu, F.H., 2002. Planetesimal formation by gravitational instability. Astrophys. J. 580, 494-505.

[204] Youdin, A.N., Goodman, J., 2005. Streaming Instabilities in Protoplanetary Disks. Astrophys. J. 620, 459-469.

[205] Zega, T.J., Buseck, P.R., 2003. Fine-grained-rim mineralogy of the Cold Bokkeveld CM chondrite. Geochim. Cosmochim. Acta 67, 1711-1721.

[206] Zolensky M., Barrett R., Browning L., 1993. Mineralogy and composition of matrix and chondrule rims in carbonaceous chondrites. Geochim. Cosmochim. Acta 57, 3123-3148.

[207] Zsom, A., Ormel, C.W., Güttler, C., Blum, J., Dullemond, C.P., 2010. The outcome of protoplanetary dust growth: pebbles, boulders, or planetesimals? Astron. Astrophys 513, A57.